UNIVERSITÉ DE GENÈVE

Archive ouverte UNIGE
https://archive-ouverte.unige.ch

Thèse 2021

Open Access

This version of the publication is provided by the author(s) and made available in accordance with the copyright holder(s).

Oxygen Control in Infinite-Layer Cuprate Heterostructures

Waelchli, Adrien

How to cite

WAELCHLI, Adrien. Oxygen Control in Infinite-Layer Cuprate Heterostructures. Doctoral Thesis, 2021. doi: 10.13097/archive-ouverte/unige:158810

This publication URL: https://archive-ouverte.unige.ch/unige:158810
Publication DOI: 10.13097/archive-ouverte/unige:158810

© This document is protected by copyright. Please refer to copyright holder(s) for terms of use.

UNIVERSITÉ DE GENÈVE
Section de physique
Département de physique de la matière quantique

FACULTÉ DES SCIENCES
Prof. Jean-Marc Triscone
Dr. Stefano Gariglio

Oxygen Control in Infinite-Layer Cuprate Heterostructures

THÈSE

présentée à la Faculté des sciences de l'Université de Genève
pour obtenir le grade de Docteur ès sciences, mention physique

par

Adrien Waelchli
de
Perly-Certoux (GE)

Thèse n° 5620

GENÈVE
Centre d'Impression de l'Université de Genève
2022

UNIVERSITÉ DE GENÈVE
FACULTÉ DES SCIENCES

DOCTORAT ÈS SCIENCES, MENTION PHYSIQUE

Thèse de Monsieur Adrien WAELCHLI

intitulée :

«Oxygen Control in Infinite-Layer Cuprate Heterostructures»

La Faculté des sciences, sur le préavis de Monsieur J.-M. TRISCONE, professeur ordinaire et directeur de thèse (Département de physique de la matière quantique), Monsieur S. GARIGLIO, docteur et codirecteur de thèse (Département de physique de la matière quantique), Monsieur C. RENNER, professeur ordinaire (Département de physique de la matière quantique), Monsieur D. DI CASTRO, docteur (Dipartimento di Ingegneria Civile e Ingegneria Informatica, Università di Roma Tor Vergata, Roma, Italia), Monsieur J. MANNHART, professeur (Departments of Solid State Quantum Electronics, Max Planck Institute for Solid State Research, Stuttgart, Germany), autorise l'impression de la présente thèse, sans exprimer d'opinion sur les propositions qui y sont énoncées.

Genève, le 30 novembre 2021

Thèse - 5620 -

Le Doyen

N.B. - La thèse doit porter la déclaration précédente et remplir les conditions énumérées dans les "Informations relatives aux thèses de doctorat à l'Université de Genève".

C'est par la foi que nous reconnaissons que le monde a été formé par la parole de Dieu, en sorte que ce qu'on voit n'a pas été fait de choses visibles.

Hébreux 11 : 3

Contents

Résumé

En 1911 Heike Kamerlingh Onnes découvre que le mercure (par la suite d'autres composés seront découverts) peut conduire l'électricité parfaitement, c'est-à-dire sans aucune perte d'énergie, lorsqu'il est refroidi en dessous d'une certaine température, nommée la température critique. Quelques années plus tard, en 1933, Walther Meißner et Robert Ochsenfeld observent que ces métaux, appelés des supraconducteurs, ont aussi la propriété d'expulser le champ magnétique (effet Meissner), ce qui peut se manifester de façon spectaculaire par le phénomène de la lévitation magnétique. De nombreuses applications révolutionnaires, dans les domaines de l'énergie, des transports, de l'informatique ou encore en médecine, pourraient voir le jour si l'on découvrait des matériaux supraconducteurs à température ambiante et à pression atmosphérique.

Les cuprates, des matériaux particulièrement prometteurs parce qu'ils détiennent la plus haute température critique (135 K) à pression atmosphérique, ont été intensément étudiés depuis la découverte de la supraconductivité dans ces systèmes par Johannes Georg Bednorz and Karl Alexander Müller en 1986. Dans les cuprates, la supraconductivité est confinée dans les plans CuO_2 ayant une charge électrique neutre. La charge est injectée depuis des réservoirs adjacents aux blocs de plans CuO_2. En conséquent, leur structure cristalline est complexe, ce qui complique l'étude et l'application de ces systèmes.

Le bloc contenant les plans CuO_2, ayant la formule chimique $ACuO_2$ (avec A = Sr, Ca ou Ba), a une structure cristalline simple : c'est un empilement de plans CuO_2 séparés par un plan de cation A, appelé structure à couche infinie ou "infinite-layer". Il peut être synthétisé sous forme de cristal ou de couche mince mais il est isolant ; pour devenir supraconducteur il doit être dopé en électrons ou en trous. Ces cuprates de type "inifinite-layer" sont le sujet d'étude de cette thèse.

Le contexte général de la recherche est présenté dans le **chapitre 1**, en particulier, une brève description des oxydes de métaux de transition, une famille de composés dont font partis les cuprates, ainsi qu'une courte introduction sur le système $LaAlO_3/SrTiO_3$ dont la supraconductivité bidimensionnelle et les mesures d'effet de champ ont été une source de motivation pour l'étude des cuprates "infinite-layer".

Le **chapitre 2** survole les propriétés principales des cuprates et des cuprates

de type “infinite-layer”. Ce chapitre ne se veut pas exhaustif, la littérature étant extrêmement riche à ce sujet, mais il présente les points les plus pertinents pour cette thèse : par exemple le rôle de l'oxygène apical dans les cuprates ou le dopage des systèmes de type “infinite-layer”. Ce chapitre présente aussi les hétérostructures combinant $SrTiO_3$ et $CaCuO_2$, un système au centre de ce travail en raison de l'émergence d'une supraconductivité bidimensionnelle d'interface.

Le **chapitre 3** décrit les méthodes expérimentales utilisées dans cette thèse, à commencer par la croissance des films par ablation à laser pulsé. Ensuite les différentes techniques de caractérisation sont présentées, telles que la diffraction à rayon X, la microscopie à force atomique ou encore les mesures de transport électrique. Ce chapitre se termine par la description de deux méthodes d'étude de spectroscopie : par absorption des rayons X et de photoémission des rayons X.

Les premiers résultats expérimentaux sont présentés dans le **chapitre 4** qui décrit l'optimisation de la croissance de bicouches de $SrTiO_3$ et $CaCuO_2$ dans notre effort pour induire la supraconductivité dans ce système. Malgré la difficulté pour obtenir des conditions de croissance reproductibles, les meilleurs échantillons sont métalliques, un résultat encourageant pour la suite du projet. Ce chapitre décrit aussi la motivation première pour l'étude de ce système, à savoir tester expérimentalement l'idée que plus l'atome d'oxygène, qui est apical à l'atome de cuivre, est éloigné du plan CuO_2 et plus la température critique serait grande. L'expérience envisage d'utiliser un champ électrique pour déplacer les atomes d'oxygène apicaux (O^{2-}) et voir l'effet de ce déplacement sur la température critique.

Le **chapitre 5** présente une étude sur le rôle de différents paramètres clés contrôlant l'incorporation d'atomes oxygène (apicaux) additionnel dans les cuprates “infinite-layer” $ACuO_{2+\delta}$, avec A = Ca, Sr et δ le surplus d'oxygène dans la structure. Alliant résultats expérimentaux et calculs théoriques, nous avons exploré le rôle des conditions d'oxydation lors de la croissance, des contraintes induites par le substrat sur les films et le rôle majeur de la taille du cation alcalin terreux (A). Nous avons notamment démontré que plus le cation A est large et plus il est facile d'incorporer des atomes d'oxygène supplémentaires dans la structure.

Les effets du surplus d'oxygène sur les propriétés physiques des cuprates de type “infinite-layer”, en particulier pour $SrCuO_{2+\delta}$, sont examinés dans le **chapitre 6**. Nous montrons que les atomes d'oxygène additionnels se situent dans les plans de Sr, apical à l'atome de Cu, ce qui conduit à l'émergence d'un axe c allongé en comparaison avec la phase “infinite-layer”. L'excès d'oxygène dans la structure mène à un fort surdopage en trous de l'atome de cuivre, comme montré par des mesures d'absorption des rayons X et confirmé aussi par des mesures de transport électrique. Nos résultats suggèrent qu'il est possible de réduire le dopage en réduisant le nombre d'atomes d'oxygène dans la structure,

cela par recuit des films à basse température ($\leq 250°C$) sous vide ou dans un flux d'azote. Ceci nous a permis d'obtenir des films métalliques, un résultat très encourageant pour notre recherche de supraconductivité dans ce système.

Introduction

In 1911 H. K. Onnes discovered that some metals (the first one was mercury) can conduct electricity perfectly, that is without any energy loss, when cooled down below a specific temperature: the critical temperature. These compounds, called superconductors, also have the property to expel magnetic fields (the Meissner effect) which can lead to spectacular effects such as magnetic levitation. Beyond today's use of the unique properties of superconductors, for instance in MRI, revolutionary applications in the fields of energy, the transport sector, computer science or in medicine could emerge if superconductivity would be obtained at room temperature and atmospheric pressure.

A family of compounds, the cuprates, are particularly promising as they hold the record of the highest critical temperature at atmospheric pressure (135 K); they have been intensively studied since their discovery in 1986 by J. G. Bednorz and K. A. Müller. In these compounds, superconductivity is confined within the CuO_2 planes. However, their crystalline structure is usually complex which complicates the study of these systems. Some cuprates, with the chemical formula $ACuO_2$ (with A = Sr, Ca or Ba) crystallise in the infinite-layer phase, a simpler crystalline structure but, as such, not superconducting, the CuO_2 planes not being doped. Superconductivity can however be induced by doping them with electrons or holes. These infinite-layer cuprates are the subject of the present thesis.

The general context is presented in **Chapter 1**, with a brief description of the transition metal oxides, a family of compounds that includes the cuprates, and a short introduction concerning the $LaAlO_3/SrTiO_3$ system whose two-dimensional superconductivity and properties that can be electric field tuned have been a source of motivation for the study of the infinite-layer cuprates.

Chapter 2 outlines the main properties of the cuprates and the infinite-layer compounds. This chapter is not comprehensive, the literature being extremely rich on this subject, but it presents the relevant information that is necessary to understand the present thesis; for example the role of the apical oxygen in the cuprates or the doping of the infinite-layer systems. It presents also heterostructures combining $SrTiO_3$ and $CaCuO_2$, a system at the centre of this work that displays interfacial and two-dimensional superconductivity.

Chapter 3 describes the experimental techniques used in the present thesis, starting with the growth of thin films by pulsed laser deposition. Then

the different techniques used to characterise the samples are presented, such as X-ray diffraction, atomic force microscopy or electrical transport measurements. This chapter ends with two more specialised experimental methods: X-ray absorption spectroscopy and X-ray photoemission spectroscopy.

We believe that because of its simple structure, the $SrTiO_3/CaCuO_2$ bilayer is a promising system to study the role of the apical oxygen in the cuprates, in particular the dependence of the critical temperature on the copper-apical-oxygen distance; the details of this idea are presented in **Chapter 4**. The first step toward the realisation of this study is the growth of the bilayers, by depositing thin films of $CaCuO_2$ and $SrTiO_3$ using pulsed laser deposition, which is also the concern of this chapter.

Chapter 5 presents a study about the role of different parameters possibly controlling the incorporation of additional oxygen atoms in the infinite-layer compounds $ACuO_2$ using both first-principle calculations and experimental investigations. Parameters such as the effect of the strain (induced by the substrate onto the thin film), the role of the oxidation power of the atmosphere used during the thin film deposition as well as the effect of the A-cation are considered.

The main subject of **Chapter 6** is to clarify where the additional oxygen atoms in the infinite-layer cuprates are incorporated, in particular for $SrCuO_{2+\delta}$. Additional information concerning the electronic state in these compounds can be extracted by comparing $SrCuO_2$ infinite-layer thin films with oxygen rich $SrCuO_{2+\delta}$ samples using various experimental techniques such as X-ray diffraction, scanning transmission electron microscopy, electrical transport measurements as well as X-ray absorption and photoemission spectroscopy techniques.

All these studies are necessary steps toward realising superconducting infinite-layer based structures.

Chapter 1

Motivation

1.1 Transition metal oxide interfaces

Transition metal oxides (TMO) belong to a class of materials which contain at least an oxygen atom and a transition metal. The oxygen atoms are generally bonded to a transition metal forming typically monoxides (TiO, CuO), dioxides (TiO_2, CuO_2) or more complex compounds as ternary oxides ($CaCuO_2$, $SrTiO_3$, La_2CuO_4). Due to the large number of structural and chemical combinations, TMO show a rich variety of physical properties. These properties include superconductivity, magnetism, ferroelectricity and structural/orbital ordering, "exotic" phases that are not achievable in standard semiconductors, making TMO promising materials for future electronic applications.

Among the large family of TMO, the most studied compounds crystallise in the perovskite structure with chemical formula ABO_3, B being the transition metal and A usually an alkali metal or a rare earth element. In the perovskite structure, illustrated in Fig. 1.1a, the transition metal (B) occupies the centre of an octahedron formed by six oxygen atoms, that is placed in a cubic-like cage formed by the A atoms. Often the octahedron rotates about the vertical or horizontal O-B-O axes in order to accommodate the different sizes of the A and B cations, distorting the unit cell away from the cubic symmetry.

Thanks to the impressive development of thin film growth techniques that has occurred during the last half century, it is now possible to grow these materials epitaxially. The epitaxial strain imposed by the substrate onto the thin film can distort the crystal structure and consequently modify the crystal field: this can potentially lead to an orbital polarisation which can influence the physical properties of the film. The strain can also be accommodated through a change of the rotations of the octahedra that, as a consequence, modifies the orbital overlap between the oxygen and the transition metal, altering the electronic bandwidth.

With the current control of the growth of these materials, the properties of different layers can be combined into a new compound, opening the possibil-

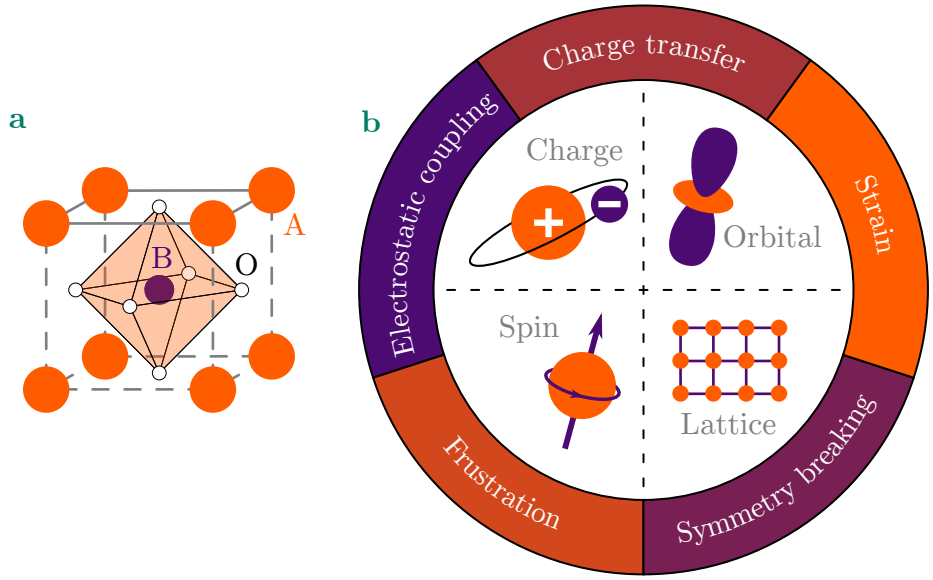

Figure 1.1: **a** Schematic of the ABO_3 perovskite structure where large orange, purple and white circles represent A, B and O respectively. The octahedral cage formed by the six oxygen atoms is shown in light orange. **b** Representation of the different degrees of freedom in TMO (in the centre) and the possible means to control them through heterostructuring (adapted from [1]).

ity of artificially designing multifunctional materials with the desired physical properties. Indeed, the different degrees of freedom of TMO such as spin, charge, lattice and orbital can be affected by different means [1, 2] as schematically represented in Fig. 1.1b. Perhaps, even more exciting, is the possibility to combine two materials in a heterostructure to promote the emergence of new physical properties that are not present in the two individual compounds.

When two materials are grown on top of each other (heterostructuring), the interface region experiences a breaking of inversion symmetry which can lead to new phenomena. Other effects such as (spin) frustration and electrostatic coupling at the interface also provide means to control these different degrees of freedom. Finally, in order to equilibrate the chemical potential between the two compounds, charge transfer can occur, leading to interface charge accumulation, i.e. local doping. A relevant example of the latter is the bilayer composed of the metallic $La_{1.55}Sr_{0.45}CuO_4$ and the insulating La_2CuO_4, both compositions being outside the region where superconductivity occurs in the cuprates phase diagram (see Section 2.1.3). When combined together, the system shows superconductivity below 15 K or 30 K depending on the stacking order [3].

In the latter example, superconductivity has been shown to be confined in few atomic layers at the interface between the two layers, but in other systems the effects of the interfacial coupling can propagate to the whole film thickness,

as, for example, for a strain effect. Some of the interactions presented in Fig. 1.1b can be long-range while others are restricted only within a few unit cells. The length scales at play are consequently important when discussing new phenomena emerging at the interface between various compounds.

1.2 Low dimensional superconductivity

Systems with superconductivity confined within a few nanometres are of great interest, principally for two reasons: the first one being the possibility to study low-dimensional quantum effects as for example the Berezinskii-Kosterlitz-Thouless (BKT) transition [4, 5]; the second reason concerns the potential application of field-effect techniques to tune the superconducting state [6] (see Section 1.3.3 for an example).

The general approach to restrict superconductivity to a thin layer is to grow ultra-thin films of a superconducting material. This thin layer can be sandwiched between two non-superconducting layers as $SrTiO_3$/δ-$SrTiO_3$/$SrTiO_3$, where the middle $SrTiO_3$ layer is δ-doped, for instance with Nb [7]. The geometrical confinement forces superconductivity to reside in the δ-$SrTiO_3$: when this layer is thinner than the superconducting coherence length, two-dimensional (2D) superconductivity is observed. Some systems are naturally layered, i.e. conduction occurs in atomic planes that are separated from each other by insulating blocks, leading to intrinsic low dimensional superconductivity, as it will be discussed in Section 2.1 regarding the cuprates. Another striking example of 2D superconductivity is the emergence of a zero-resistance state at the interface between $LaAlO_3$ and $SrTiO_3$. Being of particular interest for the present work, this system is presented in greater detail in Section 1.3. It can be briefly mentioned that the non-polar/polar interface results in a charge transfer, inducing metalicity and, below 200 mK, 2D superconductivity.

1.3 The $LaAlO_3$/$SrTiO_3$ system

In the last two decades one of the most studied systems in the community of oxide interfaces is undoubtedly the $LaAlO_3$/$SrTiO_3$ interface. Both $LaAlO_3$ and $SrTiO_3$ crystallise in the perovskite structure as illustrated in Fig. 1.2a and both are wide-bandgap insulators with a gap of 5.6 eV and 3.2 eV respectively. However, in 2004, A. Ohtomo and H. Hwang reported a metallic behaviour when a $LaAlO_3$ layer was grown by pulsed laser deposition (PLD) on top of $SrTiO_3$: the interface surprisingly shows high mobility (as high as few 1000 cm^2/Vs) [9]. Other emerging properties such as superconductivity [10, 11], spin-orbit coupling [12, 13] and even reports of magnetism [14, 15] make this system a fascinating playground for research on novel functionalities in oxides.

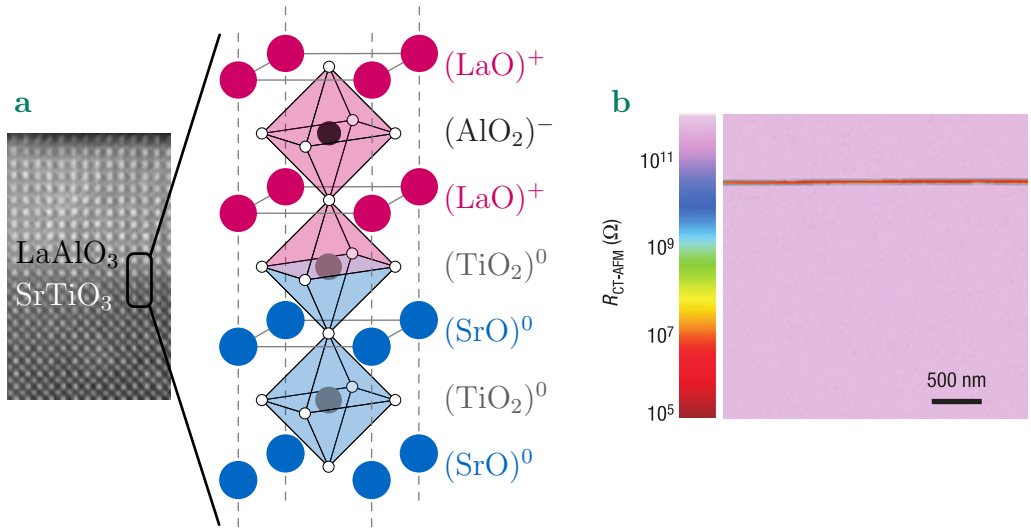

Figure 1.2: The $LaAlO_3/SrTiO_3$ system. An atomically resolved image of the interface (acquired using a scanning transmission electron microscope) with a schematic of the atomic structure is shown in **a**. A resistance profile through the interface acquired with a conductive atomic force microscope is shown in **b**, illustrating the electron system confined within 10 nm (reprinted from [8]).

1.3.1 The two-dimensional electron system

The metallic behaviour is observed only for $LaAlO_3$ layers deposited on TiO_2 terminated $SrTiO_3(001)$-oriented (so-called n-type interface) crystals with the following interfacial stacking of atomic planes: SrO-TiO_2-LaO-AlO_2, while the TiO_2-SrO-AlO_2-LaO interface (p-type) remains insulating [9]. The exact microscopic mechanism that leads to the interfacial doping is still under debate but several studies have shown the critical role of the polar/non-polar nature of the interface. The polarity of the $LaAlO_3$ layer generates an increasing potential, diverging with the layer thickness, that has to be compensated in some way (the so-called polar catastrophe); one possibility is the transfer of electrons from the $LaAlO_3$ surface to the interface [16]. The origin of these charges is not entirely clear yet: they could originate from the $LaAlO_3$ valence band (Zener breakdown scenario) but more complex mechanisms involving defects and oxygen vacancies at the $LaAlO_3$ surface have also been envisaged and are in better agreement with experimental observations [17, 18].

The electron system has been shown, both experimentally and theoretically, to be localised in $SrTiO_3$ within 10 nm from the interface [19, 20]. A nice example showing that the metallic behaviour appears only at the interface is provided by the measure of the resistance profile taken along a vertical cut through the interface using a conductive atomic force microscope as shown in Fig. 1.2b [8]. Other experimental results also confirmed the interfacial nature of the conducting layer [21–25], which is often referred to as two-dimensional

electron system (2DES). It is worth noting that the quantum confinement strongly influences the electronic band structure in comparison to bulk $SrTiO_3$ leading to a different organisation of the energy levels of the Ti-3d bands: at the Γ point, the d_{xy} has the lowest energy level, followed by the d_{xz} and d_{yz} bands [26, 27]; the finite conducting thickness also induces the formation of multiple sub-bands [19, 28].

1.3.2 Field-effect tuning of the physical properties

Using a metallic electrode deposited on the back of the $SrTiO_3$ substrates gives the possibility to apply an electric field between this electrode and the conducting interface. Thanks to the high dielectric constant of $SrTiO_3$, especially at low temperature [29, 30], such an approach allows the control of the carrier density of the electron system at the interface. Hall effect measurements reveal a typical carrier density for as-grown samples of a few 10^{13} cm^{-2}. Fig. 1.3a shows a capacitance measurement of a Hall bar patterned device: it can be estimated that the carrier density can be modulated by roughly $4 \cdot 10^{13}$ cm^{-2} for a gate voltage ranging between -200 V to +200 V [11]. This change in carrier

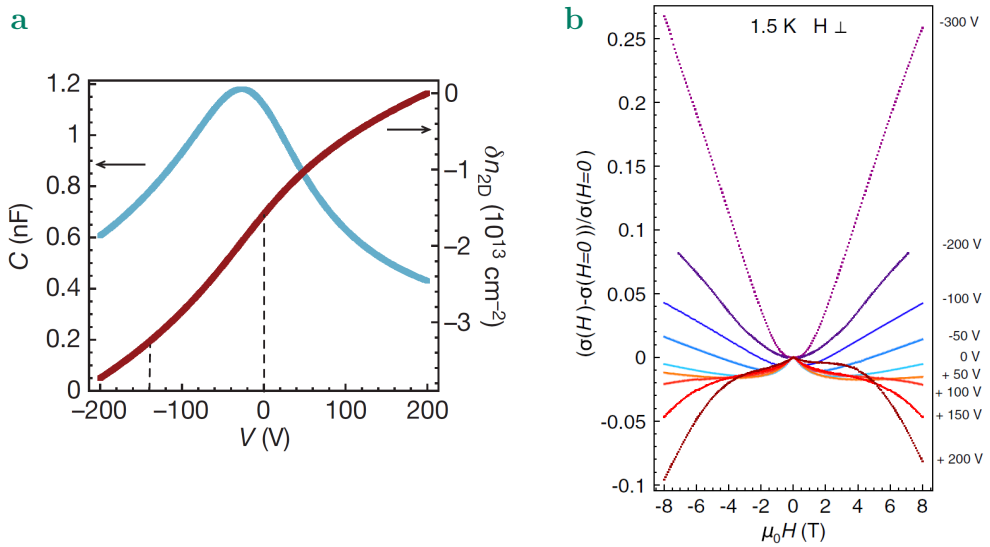

Figure 1.3: Field-effect in $LaAlO_3/SrTiO_3$. **a** Typical variation of the carrier density calculated from capacitance measurement as a function of the gate voltage (reprinted from [11]). **b** Influence of the back-gate voltage on the magneto-transport, showing the transition from weak-localisation at -300 V to weak-anti-localisation at +200 V (reprinted from [12]).

density is similar to the value of the native carrier density ($4.5 \cdot 10^{13}$ cm^{-2}) making the electric field an efficient tool to probe the phase diagram of this system. The carrier mobility is also tunable with a back-gate [31, 32] and the

increase of both the carrier density and the carrier mobility upon gating is responsible for the decrease of the sheet resistance of the 2DES.

The application of a gate voltage allows one to shift the chemical potential of the 2DES and, because of its peculiar band structure, it is possible to change from single band conduction, for the depleted situation (large negative voltages), to multi-band conduction at high carrier density (large positive voltages) [27]. It has been shown that changing the chemical potential also induces a change of the spin-orbit coupling strength [27] probably responsible for the important change in the magneto-transport behaviour shown in Fig. 1.3b in which a change from weak localisation to weak anti-localisation is observed upon increasing the gate voltage [12].

All these examples show the versatility in probing the physical properties of the $LaAlO_3/SrTiO_3$ interface using an electric field. Superconductivity, another tunable physical property of the $LaAlO_3/SrTiO_3$ system is presented in greater detail in the next section as this is particularly relevant for this work.

1.3.3 Superconductivity in $LaAlO_3/SrTiO_3$

In 2007 Nicolas Reyren et al. observed for the first time a superconducting transition in the electron system below 200 mK [10]. Analysis of these data indicates that this transition is compatible with a two-dimensional Berezinskii-Kosterlitz-Thouless transition. Using the measured critical temperature, the conducting thickness can be estimated from the bulk doping required for such T_c as 10 nm, compatible with the thickness values obtained from the local resistive profile technique described in Section 1.3.1). The study of this interface in parallel and perpendicular magnetic field allowed a superconducting in-plane coherence length of 70 nm and a superconducting thickness of only 12 nm to be extracted, confirming the two-dimensional character of the superconducting state [33].

A year after the discovery of superconductivity, field-effect experiments were performed to tune the superconducting state. Fig. 1.4a reveals the extent of the control of the superconducting state achieved in field-effect devices: superconductivity can be turned on and off and the critical temperature can be modulated over 300 mK. Such experiments uncover a superconducting dome in the phase diagram as plotted in Fig. 1.4b. The possibility to modulate the critical temperature at the $LaAlO_3/SrTiO_3$ interface is the main motivation for studying the infinite-layer cuprates as it will be explained in the next section.

Although the behaviour of superconductivity in this system resembles the one of bulk $SrTiO_3$, there may be differences associated to the details of the electronic band structure. In bulk $SrTiO_3$, one possible scenario to explain superconductivity, explored recently theoretically [34] and experimentally [35, 36] is linked to the proximity of $SrTiO_3$ to a ferroelectric quantum critical

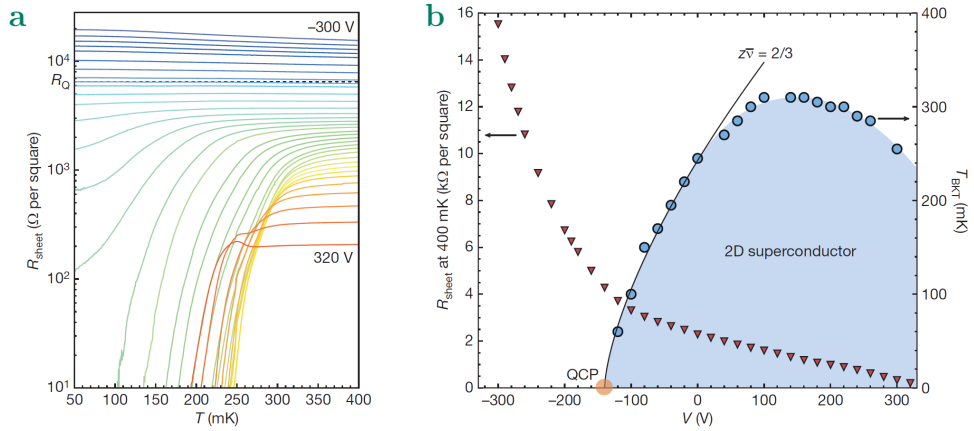

Figure 1.4: Modulation of the superconducting properties upon gating. **a** Sheet resistance as a function of temperature for different gate voltages showing the transition from superconducting to insulating behaviour. **b** Electronic phase diagram showing the critical temperature and the normal sheet resistance as a function of the gate voltage (both reprinted from [11]).

point. In this scenario, the ferroelectric fluctuations provide the pairing interaction for the superconducting carriers. In our group we have shown, for the $LaAlO_3/SrTiO_3$ system, that superconductivity can be observed, albeit without an increased T_c, in proximity of ferroelectricity if ^{18}O-substituted [37] or Ca-doped[1] $SrTiO_3$ substrates, known to be ferroelectric, are used to grow $LaAlO_3$.

The aim of this section was to give an overview of the rich physics around the $LaAlO_3/SrTiO_3$ system as a motivation behind my PhD work. For more information about this topic, the reader is invited to read the following reviews [2, 20, 38–41].

1.4 Motivation to study the infinite-layer cuprate systems

The discovery of high temperature superconductivity (HTS) in cuprate compounds [42] opened a vast field of research: since their critical temperature can be above the temperature of liquid nitrogen, they are promising materials for many applications. This field of research being far too broad and complex to be presented in detail, we overview the important features in Chapter 2.

In my thesis, I focused on infinite-layer compounds (specifically $CaCuO_2$ and $SrCuO_2$), one of the building blocks of the cuprates. In 2012 a noteworthy paper by D. Di Castro and co-workers [43] reported superconductivity in

[1] Data not published

$SrTiO_3/CaCuO_2$ superlattices. These results, described briefly in the following section and in greater detail in Section 2.3, are at the origin of the work presented in this thesis.

1.4.1 Brief description of the $SrTiO_3/CaCuO_2$ bilayer

Similarly to the $LaAlO_3/SrTiO_3$ interface, the $SrTiO_3/CaCuO_2$ system is composed of two insulating materials: $SrTiO_3$, which has a perovskite structure, and $CaCuO_2$, which crystallises in the infinite-layer phase, a structure similar to the perovskite one but missing two oxygen atoms apical to Cu. Once combined together in a superlattice or in a bilayer, this system shows a metallic behaviour and, below 50 K, superconductivity [43, 44]. Interestingly, only the interface is superconducting due to the presence of additional oxygen atoms in the alkaline plane above the last CuO_2 plane; such additional oxygen atoms act as apical oxygens for copper. The $SrTiO_3/CaCuO_2$ system, being central to this work, is presented in greater detail in Section 2.3 while the growth optimisation of this particular bilayer and our attempt to reproduce the superconducting state are presented in Chapter 4. It is worth mentioning that the uniqueness of this system is the presence of a single apical oxygen plane at the interface between $SrTiO_3$ and $CaCuO_2$ inducing the proper doping to make the interfacial $CaCuO_2$ planes superconducting.

1.4.2 Tuning the copper-apical-oxygen distance

The original idea of the present thesis is an attempt to displace the apical oxygen at the $SrTiO_3/CaCuO_2$ interface. Experimentally, a correlation has been established between the apical oxygen to copper distance and the critical temperature in the HTS cuprates. Theoretical calculations also predict that tuning this distance would drastically change the critical temperature; more details are given about the theoretical part in Section 2.1.5. The $SrTiO_3/CaCuO_2$ system, with its single apical oxygen plane, is a perfect candidate to study the role of the copper-apical-oxygen distance in these materials.

In order to displace the apical oxygen, the idea is to use an electric-field, similarly to $LaAlO_3/SrTiO_3$, described in Section 1.3.1, in which a gate voltage is used to tune the interfacial superconductivity. More precisely, for the $SrTiO_3/CaCuO_2$ system, the idea is to modify the position of the negatively charged apical oxygen (O^{2-}) with an electric field, and study the effect of this displacement on the critical temperature.

Chapter 4 is dedicated to this specific project.

1.4.3 Study of the infinite-layer cuprate oxygenation

The presence and/or the position of the apical oxygen in cuprates is a particular example of a more general fact: in TMO the environment of the transition metal is key to determining the physical properties of the compound. Consequently, understanding and controlling the oxygen content as well as the position of the oxygen atoms within the crystal structure is essential.

Chapter 5 presents a study concerning the oxygenation of the infinite-layer phase in cuprates, in particular for $CaCuO_{2+\delta}$ and $SrCuO_{2+\delta}$. This is carried out using various oxidising growth atmospheres during the deposition of the infinite-layer thin films as well as exploring the importance of the A-cation (A=Ca, Sr) and the strain induced by the substrate into the layer. In brief, the chapter discusses how the oxygen content in $CaCuO_{2+\delta}$ and $SrCuO_{2+\delta}$ can be controlled.

The physical properties of oxygen rich $SrCuO_{2+\delta}$ are studied in detail through a variety of techniques and presented in Chapter 6.

Chapter 2

High-temperature superconductors and infinite-layer cuprates

2.1 Cuprates

The term "cuprate" generally indicates a chemical compound in which copper forms a negative complex. Various examples can be found in the halogenocuprates ($[CuCl_4]^{2-}$, $[CuF_6]^{2-}$) and in the more complex compounds as the iodocuprates or the organucuprates [45]. However, in the present work this term will label materials known for their high temperature superconductivity, containing the $[CuO_2]^{2-}$ anion.

Since the discovery of superconductivity in these compounds, a plethora of studies have been published, revealing the richness of the cuprates. The purpose of this chapter is to give a brief overview of what is known in the field, without in any way pretending to be a complete description. The general properties will be just outlined while other topics, more relevant for the present work, will be presented in more details.

2.1.1 Brief history

In the beginning of the 20th century, H. K. Onnes succeeded in liquefying helium. This achievement allowed him and his team to study the resistivity of metals at low temperature. In 1911 he found that the resistance of mercury suddenly drops to zero around 4.2 K [46]. This was the first observation of superconductivity: a new state of matter with perfect conductivity. 20 years later, W. Meissner and R. Ochsenfeld discovered that a superconductor shows also perfect diamagnetism [47]. Other superconducting materials were later discovered in pure metallic elements such as lead or niobium and in various compounds such as the well-known A15-superconductors (e.g. Nb_3Sn).

Alongside such discoveries, the critical temperature (T_c) – the temperature at which a material becomes superconducting – increased from 4.2 K (observed for mercury in 1911) to 22.3 K for Nb_3Ge in 1973. Then for almost 13 years, T_c did not increase.

However, in 1986, a major breakthrough of solid state physics occurred with the discovery of superconductivity in the La-Ba-Cu-O (LBCO) system by J. G. Bednorz and K. A. Müller [42]. They measured a critical temperature of about 30 K, indicating the beginning of high temperature superconductivity. Later in the same year, T_c was raised by about 10 K substituting Ba with Sr to form $(La_{1-x}Sr_x)_2CuO_{4-\delta}$ (LSCO)[48]. Inspired by a hydrostatic pressure study in LBCO revealing an increase of T_c [49], M. K. Wu tried to induce a chemical pressure by replacing La with Y. In this way, he could reach a T_c of 93 K [50] in $YBa_2Cu_3O_{7-\delta}$ (YBCO), probably the most famous cuprate superconductor. YBCO was regarded as a very promising material, being the first material to superconduct above the liquefaction temperature of nitrogen (77 K). The increase of the critical temperature continued with the discovery in 1988 of a member of the $Bi_2Sr_2Ca_{n-1}Cu_nO_{2n+4+\delta}$ (Bi-22(n-1)n) family with T_c above 100 K [51] and 5 years later with the homologous Hg-series having the highest known superconducting transition at 135 K [52] (164 K under pressure [53]).

One of the great goals of modern condensed matter physics is to increase the maximal critical temperature even further. Reaching room temperature superconductivity at ambient conditions would be a fantastic success enabling a variety of applications to come to life.

2.1.2 Crystallographic structure

Cuprates have a crystallographic structure belonging to the tetragonal or the orthorhombic crystal systems, composed of a stacking of different layers along their c-axis forming an elongated unit cell ($c >> a, b$) [54]. They all have a common element: at least one CuO_2 plane which hosts superconductivity when cooled below the critical temperature. A typical structure is sketched in Fig. 2.1a showing the structure of $Bi_2Sr_2Ca_{n-1}Cu_nO_{2n+4+\delta}$ for n=3 (Bi-2223). Most of these compounds can be described by the general formula $MCa_{n-1}Cu_nO_{2n}$, with M being a set of metal oxide layers, for instance $Bi_2Sr_2O_{4+\delta}$ for Bi-2223 [57], which constitute the charge reservoir block and $Ca_{n-1}Cu_nO_{2n}$, a stack of CuO_2 planes intercalated by Ca planes, which is the CuO_2 block; the details of the CuO_2 block will be described in greater detail in Section 2.2. On each side of the CuO_2 block the charge reservoir (CR) provides the charges - electrons or holes - that dope the CuO_2 planes; modifying the composition of the CR block either by chemical substitution (for instance, Sr instead of La for the LSCO system) or by controlling the oxygen content (as in the case of YBCO) allows a precise control of the charge transferred to

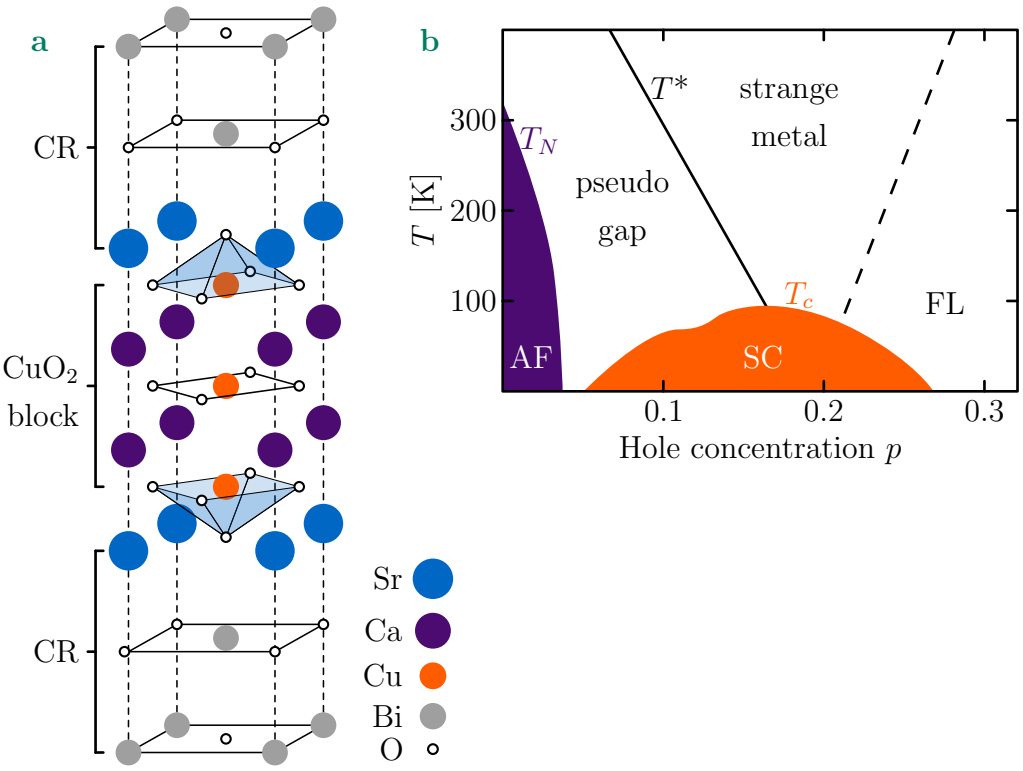

Figure 2.1: General properties of the cuprates. **a** Sketch of their typical layered structure, showing the CuO_2 blocks surrounded by charge reservoirs (CR) (adapted from [55]). **b** Generic phase diagram illustrating the richness of these systems described in the main text. AF, SC and FL stands for the antiferromagnetic, superconducting and Fermi liquid phases respectively while T_N, T_c and T^* are for the Néel, superconducting and pseudo-gap transition temperatures (Adapted from [54, 56]).

the CuO_2 block. As illustrated in Fig. 2.1a the cuprate structure is symmetric about a central CuO_2 plane. This is an important point to keep in mind for the study of the $SrTiO_3/CaCuO_2$ interface, mentioned briefly in Section 1.4.1, and detailed in Section 2.3. Due to their elongated and layered structure along the c-axis as well as the presence of the charge reservoir between the CuO_2 blocks, the CuO_2 interlayer coupling is weak leading to relatively high anisotropy of both the superconducting and normal properties, the former showing for some compounds quasi-2D behaviour [54, 58].

2.1.3 The phase diagram of cuprates

In the following we introduce briefly the generic phase diagram of the cuprates. In undoped crystals, copper has a 2+ valence state and a $3d^9$ electronic configuration. The local structure splits the two $3d-e_g$ orbital states, with the $d_{x^2-y^2}$ orbital becoming the highest in energy, filled with one single electron. With

an electronic band half-filled, one could expect a metallic behaviour, however this is not what is observed. The reason is that these materials are strongly correlated, with a large electron-electron interaction due to a strong on-site Coulomb repulsion, consequence of the localised nature of the $3d$ orbitals. This leads to a splitting of the band into a filled lower and an empty upper Hubbard band (respectively LHB and UHB) and a Mott insulating state[1]. A magnetic interaction between the localised electrons gives rise to an antiferromagnetic (AF) ground state. All the parent compounds (undoped) of the HTS cuprates are AF Mott insulators [54, 59].

Doping these systems leads to complex and very rich phase diagrams. Superconductivity has been observed for both electron (n-type) and hole (p-type) doping but the systems that attracted more attention are mainly the hole doped ones because of their higher critical temperature. The reader interested in a detailed review on the research progress in electron doped cuprates can consult Reference [60]; in the following we will focus on p-type cuprates.

In Fig. 2.1b a generic phase diagram for hole doped cuprates is presented, showing the different electronic states as a function of temperature (T) and hole concentration (p, holes per Cu). Considering the ground state, at low doping the cuprates show the already mentioned insulating AF order, rapidly destroyed when the hole concentration is increased. This gives way to superconductivity, that fills a dome in the $T-p$ diagram with its maxima occurring at around $p \sim 0.16$. Once superconductivity is lost, one recovers a metallic state with Fermi liquid (FL) behaviour. For $p < 0.16$, in a region comprised between T_c and T^*, a region with a gapped density of state but without superconductivity is observed, the pseudo gap regime. Understanding this region of the phase diagram may help understand the mechanism behind the Cooper pair coupling. For larger doping, a strange metallic behaviour is observed in the normal state: for instance, a linear dependence of the resistivity in temperature instead of the T^2 expected for FL.

Before closing this section, we briefly mention one important property related to the superconducting state in the cuprates concerning the symmetry of the order parameter: the superconducting gap is unconventional with a d-wave symmetry as opposed to the s-wave symmetry observed in conventional superconductors. Notice that these compounds show extreme type-II superconductivity, implying the presence of vortices in a magnetic field.

To go further in the impressive work that has been done in the last 40 years concerning the cuprates, the reader is invited to refer to the extensive information contained in the following books and reviews [54, 56, 58, 61–64].

[1] Because of the strong hybridisation between the copper and the oxygen orbitals one should more rigorously call the cuprates charge transfer (CT) insulators [56], the O $2p$ bands being higher in energy than the LHB.

2.1.4 Factors influencing T_c

Among the different cuprates, partially cited in Section 2.1.1, the critical temperature measured at optimal doping spans a broad range, roughly between ∼25 K and 135 K. This indicates that the critical temperature is highly material-dependent and particularly sensitive to various factors that will be described in this section.

Doping As already mentioned in Section 2.1.3, controlling the doping by varying the hole concentration (p) allows one to tune T_c (see Fig. 2.1b). In the underdoped regime (i.e. for doping lower than the optimal doping), increasing the hole concentration raises the superfluid density and enhances the interlayer coupling, resulting in higher T_c. On the overdoped side of the phase diagram, the main effect of increasing p seems to be the reduction of the pairing interaction.

Number of CuO_2 planes The dependence of the critical temperature on the number of CuO_2 planes (n) present in the CuO_2 block is shown in Fig. 2.2a ("multilayer effect"): T_c increases up to $n = 3$, where it reaches its maximal value and then starts to decrease for $n \geq 4$ [55, 57]. Such dependence has

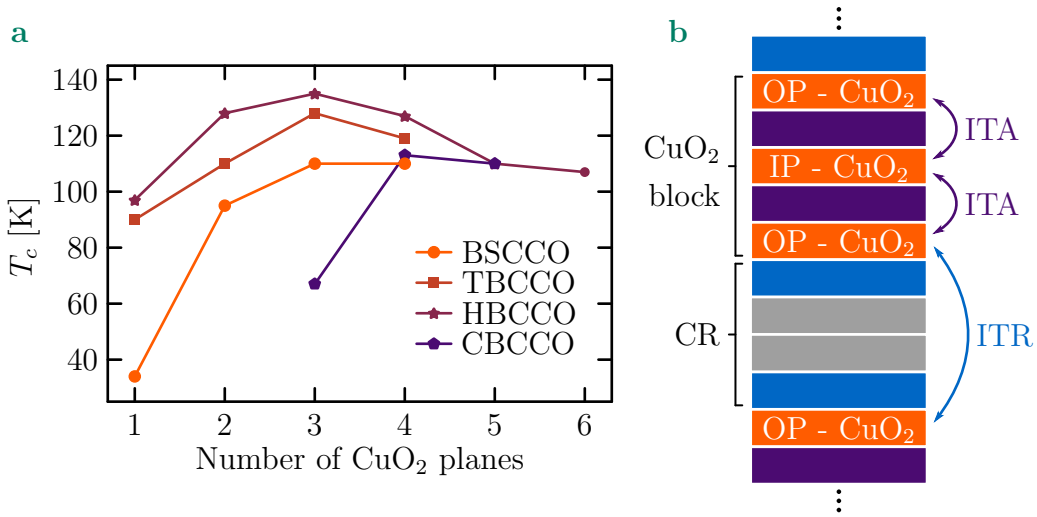

Figure 2.2: Multilayer effect in the cuprates. **a** Critical temperature (T_c) dependence on the number of CuO_2 planes (n) for the following families of multilayers cuprates: $Bi_2Sr_2Ca_{n-1}Cu_nO_{2n+4}$ (BSCCO), $Tl_2Ba_2Ca_{n-1}Cu_nO_{2n+4}$ (TBCCO), $HgBa_2Ca_{n-1}Cu_nO_{2n+3}$ (HBCCO) and $Cu_2Ba_2Ca_{n-1}Cu_nO_{2n+4}$ (CBCCO). The maximal T_c is reached for n=3-4 (data from [65]). **b** Schematic of the different couplings between the various CuO_2 layers: the interlayer (ITR) coupling is between two CuO_2 planes that belong to distinct CuO_2 blocks while the intralayer (ITA) coupling is between two CuO_2 planes belonging to the same block. OP and IP are for outer-plane and inner-plane respectively.

been observed in most of the cuprates families, indicating that such behaviour is quite general.

Different phenomena are at play in these structures. On can mention, for example, a charge imbalance between the inner-planes (IP) and the outer-planes (OP). The charge profile has been measured by nuclear magnetic resonance (NMR) [66] and angle-resolved photoemission spectroscopy (ARPES) [67], showing that the hole concentration in the CuO_2 planes further away from the charge reservoirs is lower than the one in the OP. This is probably due to the presence/absence of an oxygen atom, apical to the CuO_2 planes in question, thought to be crucial in the doping process (see Section 2.1.5). The charge profile is not, on its own, sufficient to fully explain the multilayer effect. For instance, in [67] the authors show that using the doping values of the OP (overdoped) and IP (underdoped) for Bi-2223 does not explain the measured T_c of 110 K, as one would expect a maximum T_c of 60 K .

Another phenomenon, present in the cuprates, that can help to explain the high T_c reported in the previous example, takes its origin in the coupling of the different superconducting layers [68, 69]. As the cuprates have a layered structure, the superconducting planes can be coupled relatively strongly within a single CuO_2 block (intralayer coupling, see Fig. 2.2b) leading to an increase of T_c [70, 71]. The coupling can also occur between two different CuO_2 blocks (interlayer coupling) but is generally small because of the large size of the charge reservoir. However, these two types of coupling can be studied using artificial structures as shown in [72], revealing the importance of these couplings for the value of the superconducting transition temperature. The highest T_c value, for $n = 3$, may also be linked to the fact that the IP are protected, and disorder is consequently lower.

Disorder Among the different parameters that control the critical temperature in the cuprates, disorder can make things quite complicated. As their structure is relatively complex, disorder can occur in various locations and its effect strongly depends on the latter.

In the CuO_2 blocks, deliberate substitution of Cu by Zn is detrimental for superconductivity [54, 56] probably due to its fixed valence compared to Cu. While substitution of Ca with Y (in-between two CuO_2 planes) does not appear to be too dramatic [73] for the critical temperature.

In the charge reservoir, the effect of disorder is strongly dependent on its location too [73, 74]. For defects far from the planes where the apical oxygen atoms are located, their effect is relatively modest, while for defects in the apical-oxygen plane T_c can be strongly reduced. This is particularly true for the single layer cuprates, for which the only CuO_2 plane is in direct proximity to the apical-oxygen planes, being probably the reason for their generally low critical temperature. Considering the multilayer effect, especially for $n = 3$, the IP are protected from disorder in the charge reservoir and T_c is increased.

A meticulous table summarising the effect of disorder and its location can be found in [73].

Reducing disorder is crucial in order to obtain high-T_c compounds; an elegant example achieving this purpose in Sr_2CuO_3 is reported in [75]. By annealing their samples in N_2, between 150°C and 350°C, they managed to order the apical oxygen atoms, increasing T_c from 75 K to 95 K.

Apical oxygen The apical oxygen is the oxygen atom located above Cu along the c-axis, forming an oxygen pyramid with the other oxygen atoms in the CuO_2 plane, as illustrated in Fig. 2.1a; it is thought to be crucial for p-type superconductivity in the cuprates (see for example [76–78] and Section 2.1.5). As the role of the apical oxygen is central to the present study, its relation with T_c is presented in the following section.

2.1.5 Role of the apical oxygen in cuprates

Among the parameters presented in the previous section influencing the critical temperature of the cuprates, the presence and position of the apical oxygen have proven to be key in determining T_c. The importance of its presence was already envisaged a few years after the discovery of the cuprates [76, 79–82]. This was motivated by hydrostatic pressure studies, revealing an increase of T_c with pressure ($\frac{dT_c}{dP} > 0$) in hole doped cuprates [81, 83] but not for electron doped systems; structurally, the main difference between the two families is the presence of the apical oxygen, which is present only in hole doped systems [80]. Hydro-static pressure reduces the lattice volume, affecting all the bond lengths indistinctly [81, 84]. Interestingly, uniaxial pressure studies on different cuprate families showed that the sign of the T_c variation depends on the direction of the applied pressure. Indeed, a pressure applied along the out-of-plane direction (P_c) leads to $\frac{dT_c}{dP_c} < 0$ while for an in-plane pressure (P_{ab}) one observes that $\frac{dT_c}{dP_{ab}} > 0$, suggesting that a long c-axis and potentially a long $d^{\text{apical}}_{\text{Cu-O}}$ is favourable for high critical temperatures [85–87]. Remarkably, the same effect has been observed for a thin film grown on a compressive substrate (mimicking in plane pressure) [88].

Plotting the critical temperature as a function of the Cu-O vertical bond length, see Figure Fig. 2.3 for the single layer cuprates, one observes that T_c scales with $d^{\text{apical}}_{\text{Cu-O}}$. Performing the same analysis for all the cuprates is more difficult because the multilayers have CuO_2 planes without apical oxygen and it becomes non-trivial to compare them. However, the effect of the copper-apical-oxygen distance and its correlation with T_c can be connected theoretically to different electronic parameters, and this can also be generalised to the multilayer cuprates.

Between the different models that have been developed to account for this observation, in the following we discuss the proposition carried out by C. Weber

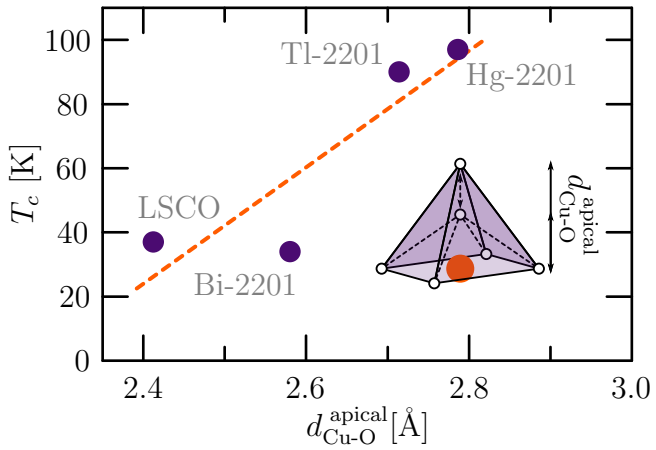

Figure 2.3: Superconducting critical temperature as a function of the copper-apical-oxygen distance for single layer cuprates (data from [65, 89–91]). Inset: detailed view of the apical oxygen position.

et al. [92]. They used a 3-band model to account for the in-plane O $2p$ ($2p_{x,y}$) and Cu $3d$ ($3d_{x^2-y^2}$) orbitals with four parameters to describe the physics in the CuO_2 plane: three different hopping terms (t_{pd}, t_{pp}, $t_{pp'}$), represented schematically in Fig. 2.4a, and the charge-transfer energy ($\epsilon_d - \epsilon_p$) which expresses the difference between the Cu $3d_{x^2-y^2}$ and the O $2p_{x,y}$ energy levels within a CuO_2 plane. Among these four parameters, only $t_{pp'}$ and $\epsilon_d - \epsilon_p$ vary significantly between the different cuprates to eventually explain the large spread of the T_c values. Calculating the superconducting strength Δ_{max} as a proxy of the critical temperature, they show that Δ_{max} (experimentally T_c) is mainly controlled by the charge-transfer energy. In Fig. 2.4b it can be observed that using LSCO as a prototype compound and artificially reducing $\epsilon_d - \epsilon_p$, the superconducting strength is increased, leading to a higher T_c. This trend can be generalised to different compounds (shown in [92]), confirming the essential role of the charge-transfer energy in the determination of the critical temperature among the cuprates.

For the single layer cuprates, $\epsilon_d - \epsilon_p$ can be correlated to $d^{\text{apical}}_{\text{Cu-O}}$ (see Fig. 2.4c) as there is only a single CuO_2 plane with apical oxygen atoms; there is no CuO_2 plane without apical oxygen as in the multilayer cuprates. Calculations show that moving the apical oxygen away from the CuO_2 plane decreases $\epsilon_d - \epsilon_p$ and consequently leads to higher superconducting critical temperature (Fig. 2.4c) as experimentally observed (Fig. 2.3). In this simplified case, the fact that the copper-apical-oxygen distance controls the charge-transfer energy can be physically understood considering that the apical oxygen has a negative oxidation state (O^{2-}) and thus is negatively charged. When this oxygen is brought near to the CuO_2 plane ($d^{\text{apical}}_{\text{Cu-O}}$ is reduced), the electrostatic repulsion at the Cu site underneath increases for other electrons, it is more difficult to move an electron on the copper site and this increases $\epsilon_d - \epsilon_p$ leading to

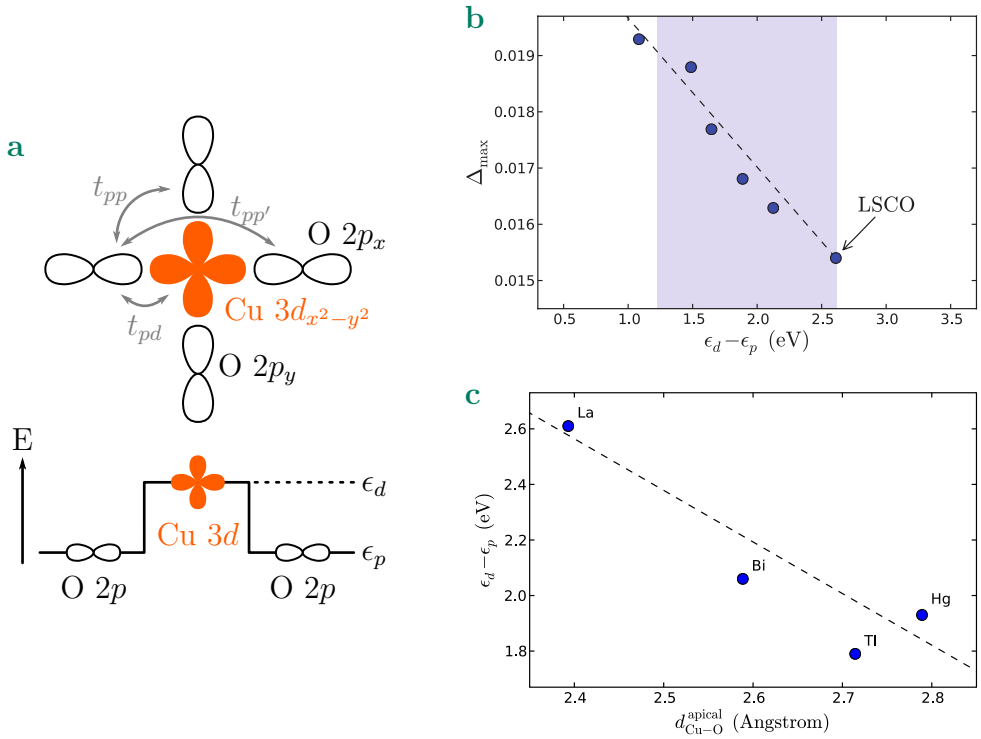

Figure 2.4: Theoretical calculations investigating the role of the charge-transfer energy and $d^{\text{apical}}_{\text{Cu-O}}$ on the superconducting critical temperature. **a** View of a CuO_2 plane showing the relevant orbitals and hopping parameters considered in the calculations (Top). Schematic representation of the Cu $3d_{x^2-y^2}$ and the O $p_{x,y}$ energy levels (Bottom) defining ϵ_d and ϵ_p (Adapted from [92]). **b** Superconducting strength (Δ_{max}) in LSCO calculated as a function of the charge-transfer energy ($\epsilon_d - \epsilon_p$). **c** Correlation between $\epsilon_d - \epsilon_p$ and $d^{\text{apical}}_{\text{Cu-O}}$ for the single layer cuprates. Panels **b** and **c** are reprinted from [92].

more localised charges in the system, an effect obviously not favourable for superconductivity.

Other theoretical works, including different orbitals in their calculations, have brought to light the influence of other electronic parameters on T_c than the charge-transfer energy[2]. For example, in [93] the authors calculated the Madelung potential for the different sites (Cu, planar O and O^{apical}), showing that T_c scales with the energy difference between the $2p_z$ orbital state of the apical oxygen and the $2p_{x,y}$ orbital of the in-plane oxygen atoms. Interestingly, the authors do not find any obvious correlation between T_c and $d^{\text{apical}}_{\text{Cu-O}}$ in their calculation. Including the Cu $4s$ orbital in density functional theory (DFT) calculations and taking into account the first three Cu nearest neighbours hoppings (t, t', t''), the copper-apical-oxygen distance has been shown to be

[2]Note that T_c is not directly calculated. Usually some electronic parameters are calculated, for various compounds, and then compared with experimental T_c.

connected to the hopping range parameter ($r \sim t/t'$) which reflects the long-range hopping strength [94]. The further the apical oxygen, the stronger the in-plane coupling leading to longer ranged hopping and favouring high T_c. More recently, in calculations considering also the contribution of the Cu $3d_{z^2}$ orbital, the energy difference (ΔE) between the Cu $3d_{x^2-y^2}$ and Cu $3d_{z^2}$ orbitals was shown to be relevant in determining the critical temperature [95, 96]. Long $d_{\text{Cu-O}}^{\text{apical}}$ increases the crystal field splitting which enhances ΔE, and from their calculations this leads to higher critical temperature.

Even if these calculations differ in some of their assumptions and consider different electronic parameters, the overall idea is to keep the central Cu $3d_{x^2-y^2}$ orbital isolated, with a small hybridisation with the other orbitals, particularly with the out-of-plane ones. This has been referred as "orbital distillation" in [96]. The analysis of the experimental results and the theoretical models therefore suggest that a large $d_{\text{Cu-O}}^{\text{apical}}$ generally leads to higher critical temperature in the cuprates.

2.2 Infinite-layer cuprates

2.2.1 Structure

In this section, the focus is on one particular type of cuprates: the infinite layer, which is composed of the CuO_2 block shown in Fig. 2.1a. The name of this structure can be understood by looking at the evolution of the multilayer cuprates with the number n of CuO_2 planes as illustrated in Fig. 2.5. When $n \to \infty$ the dominant structure becomes the one of the CuO_2 block composed of CuO_2 planes intercalated with Ca planes, for BSCCO. More rigorously, the infinite-layer structure is the end compound of the series $A_{n+1}Cu_nO_{2n+1}$ (for $n = \infty$) with A an alkaline earth metal (Ca, Sr or Ba) and can be written as $ACuO_2$ [97]. They are considered as the parent structure of the cuprates as they have the simplest structure containing only the CuO_2 block essential for superconductivity [98]. It is worth noting that this structure can be seen as a perovskite structure (ABO_3) missing the two apical oxygen atoms; the lack of the charge reservoir block makes the infinite-layer compounds with a pure alkaline composition undoped compounds which exhibit an insulating behaviour. The absence of apical oxygen atoms reduces the out-of-plane extension of the structure that becomes tetragonal with the space group P4/mmm: the bulk lattice parameters for A = Ca, Sr, and Ba are reported in Table 2.1.

2.2.2 Growth of infinite-layer cuprates

After the discovery of high temperature superconductivity in cuprates, the infinite layers have been extensively studied, because of their simple structure containing only the CuO_2 block. The first report of an infinite-layer structure

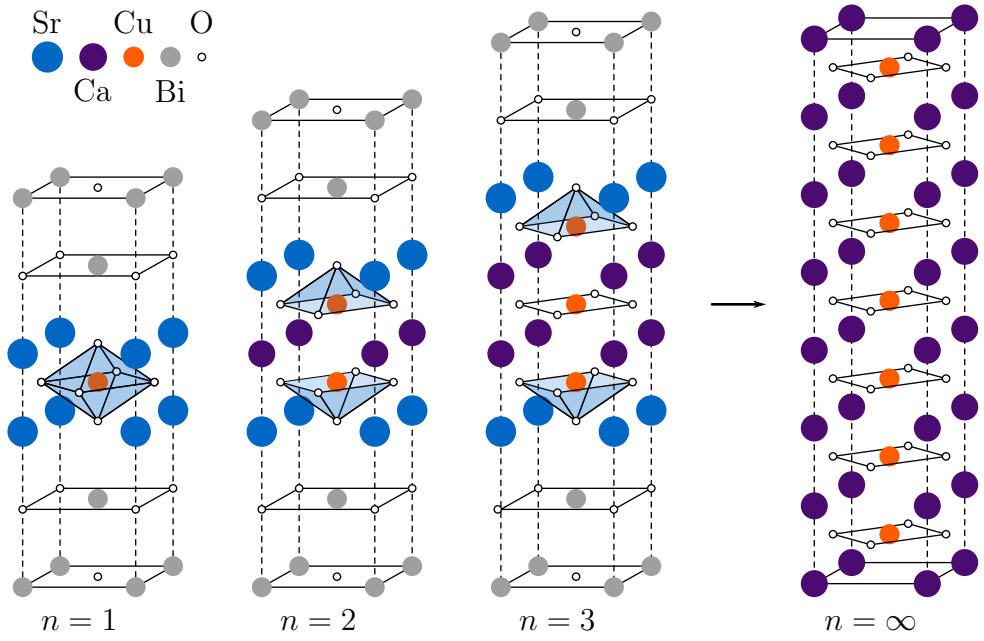

Figure 2.5: Structure of the multilayer $Bi_2Sr_2Ca_{n-1}Cu_nO_{2n+4}$ family used as a prototype for the structure of the multilayer cuprates. For $n = \infty$ the infinite-layer structure is obtained (adapted from [55]).

was for a $Ca_{0.86}Sr_{0.14}CuO_2$ sample grown at atmospheric pressure and high temperature (1423 K) [98]. However, growth at atmospheric pressure does not generally and reproducibly lead to the formation of the infinite-layer phase, for various A-cations. In particular for the single cation (A = Ca, Sr, Ba) composition: growth of $BaCuO_2$ [100] and $SrCuO_2$ [101] has been reported with other phases than the infinite-layer one, while $CaCuO_2$ is not stable [102, 103]. On the other hand, the infinite-layer phase can be stabilised for a broad range of A-cation ionic radii[3] by applying a pressure of several GPa during the growth [103–108], except for $BaCuO_2$, that cannot be stabilised in an infinite-layer structure at all, probably because of its large ionic radius [102, 109]. It is worth mentioning that temperatures higher than 1300 K are generally required to obtain the infinite-layer structure.

Thanks to the impressive development of thin film growth techniques, as PLD, molecular beam epitaxy (MBE) and sputtering, it became possible to grow single phase infinite-layer thin films. The epitaxial strain induced by the substrate mimics the high pressure required for bulk growth allowing different research groups to obtain the pure infinite layer phase $ACuO_2$ with A = (Sr, Ca) [110, 111], Sr [112–114] or Ca [115] in a thin film form. As it is discussed in the next section the possibility to have single phase films, which seems to be

[3]The average ionic radius can be controlled using mixture of Ca, Sr and Ba for the alkaline metal element A in $ACuO_2$ [102].

	$CaCuO_2$	$SrCuO_2$	$BaCuO_2$
A-radius [Å]	1.12	1.26	1.42
a [Å]	3.856	3.925	n/a
c [Å]	3.181	3.431	n/a

Table 2.1: Lattice parameters of the infinite-layer compounds. The ionic radii of the alkaline metal element (A-radius) are extracted from empirical value reported in [99]. The lattice parameters are extracted from powder diffraction files. For $BaCuO_2$, structural data are not available (n/a) as it generally hosts oxygen atoms in the Ba planes and has not been reported in the strictly speaking infinite-layer structure.

difficult for bulk samples, is important in order to understand the appearance of superconductivity in these systems.

2.2.3 Doping of the infinite-layer cuprates

As mentioned in Section 2.2.1, the infinite-layer cuprates $ACuO_2$ (A = Ca, Sr, Ba) show a semiconducting behaviour because Cu is in a 2+ valence state. Metallicity and eventually superconductivity appear upon doping: electron doping is achieved by cation substitution with a trivalent element (e.g. $Sr_{1-x}B_xCuO_2$, B = Nd^{3+}, La^{3+}, Sm^{3+}, Gd^{3+}) [105, 116, 117] and hole doping can be induced by cation vacancies; for example $(Ca_{1-x}Sr_x)_{1-y}CuO_2$ is superconducting, with a critical temperature of 110 K [106]. Interestingly, in the latter, cation vacancies do not distribute randomly, but order in defect planes, leading to the formation of natural superlattices. Similar contrast in scanning transmission electron microscope (STEM) images can be observed for different bulk infinite-layer systems reported to be superconducting [97, 107, 108]. The appearance of superconductivity was then associated with the presence of these superstructures along the out-of-plane axis, as superconducting properties seems enhanced for higher defect layer concentration [106, 108]. Interestingly, in a different work, this superstructure has been associated to the presence of oxygen atoms in the $Ca_{1-x}Sr_x$ planes [118]. If this is correct it suggests that the apical oxygens are crucial to hole dope these infinite-layer systems (see Section 2.1.5).

Beyond the role of the epitaxial strain, thin film growth makes the synthesis of artificial layered structures possible, allowing infinite-layer heterostructures that show superconductivity to be synthesised. While $BaCuO_2$, $SrCuO_2$ and $CaCuO_2$ single films are insulating, $(BaCuO_2)_3/(CaCuO_2)_1$ superlattices show a zero-resistance state at around 30-38 K [119]; similarly $(BaCuO_2)_2/(SrCuO_2)_1$ superlattices superconduct below 50 K [120]. In these heterostructures the doping is thought to originate from the presence of ad-

ditional oxygen atoms in the Ba planes, acting as apical oxygens [121]. One could say that the $BaCuO_2$ layers are acting as charge reservoirs, doping the $SrCuO_2$ and $CaCuO_2$ blocks [122]. This idea was already proposed from the observation of the crystal structure in bulk crystals [108] and investigated in greater detail for thin films in $BaCuO_2/CaCuO_2$ heterostructures [123–125].

2.3 The $SrTiO_3/CaCuO_2$ System

The team of Giuseppe Balestrino in Rome had been investigating superlattices of infinite layer compounds when they discovered that also the $SrTiO_3/CaCuO_2$ structure can be superconducting [43, 44, 126–130]. The two compounds are neither metallic nor superconducting, however, combining them together under certain growth conditions can lead to high temperature superconductivity, as will be presented in this section.

2.3.1 The atomic structure of the interface

$SrTiO_3$ is a perovskite, a structure that differs from the infinite-layer one by the presence of apical oxygen atoms above and below the Ti atom and consequently alternate planes of SrO and TiO_2. Depending on the stacking order, two types of interfaces between $CaCuO_2$ and $SrTiO_3$ are possible: Ca-CuO_2-SrO-TiO_2 or CuO_2-Ca-TiO_2-SrO; a sketch of the second one, which is the relevant interface for the appearance of superconductivity, is shown in Fig. 2.6a. For this interface, one would expect that the last Ca-plane (denoted by CaO_x in the sketch) would be a pure Ca plane without any oxygen. However, in [43, 44, 127] the authors demonstrated that oxygen can be incorporated in the Ca plane at the interface when these systems are grown under highly oxidising conditions, more specifically in an ozone environment. An impressive STEM image acquired in annular bright-field (ABF) mode[4] is shown in Fig. 2.6 revealing intensity between two Ca atoms at the interface: such intensity is associated with the presence of apical oxygen only in the first Ca planes [44]. Line profiles along the first (left) and the fourth (right) Ca plane are shown below the STEM image, demonstrating that, far from the interface, oxygen is not incorporated in the Ca planes. Raman spectroscopy also reveals a shift in frequency of a peak associated to the oxygen bending mode in the CuO_2 planes, between structures grown in O_2 and in the O_2/O_3 mixture. This points toward a change between planar and pyramidal Cu coordination when highly oxidising growth atmosphere is used [127].

The reason for the incorporation of oxygen atoms only at the interface comes from the fact that the last Ca plane is in-between two different struc-

[4] ABF is more sensitive to light atoms such as oxygen as compared to the usual high-angle annular dark-field (HAADF) mode which shows contrast depending on the atomic number.

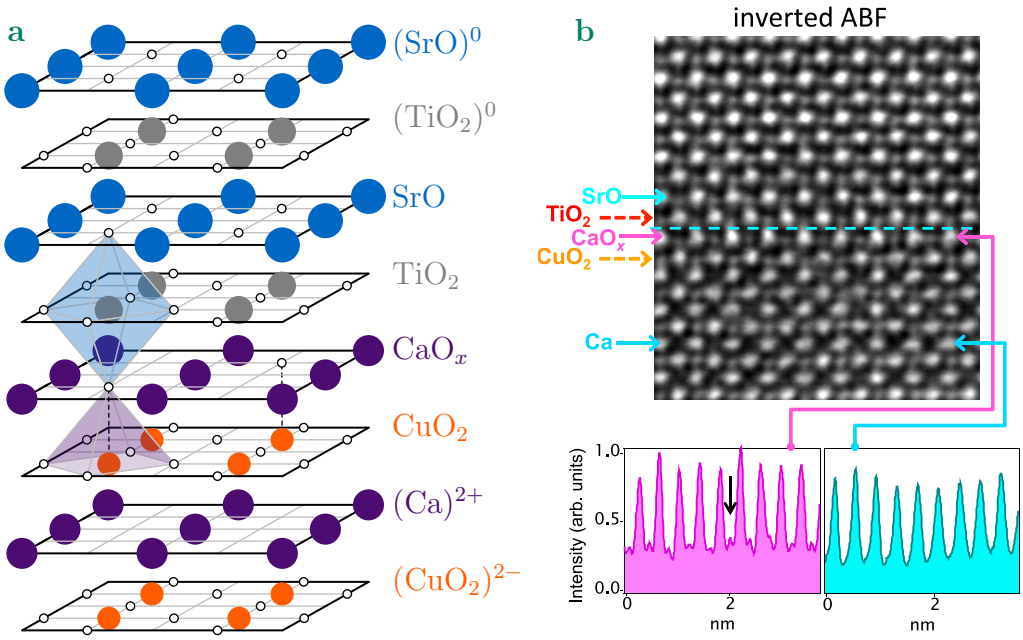

Figure 2.6: Structure of the $SrTiO_3/CaCuO_2$ interface. **a** Schematic representation illustrating the incorporation of oxygen atoms (white circles) in the last Ca plane (CaO_x). The completion of the octahedral cage of the perovskite structure is shown in blue above the Ca plane, while the apical site is highlighted by the purple pyramid. **b** A STEM image in annular bright-field (ABF) mode, revealing the incorporation of oxygen atoms only in the first 1-2 u.c. of the infinite layer. Below this image, two line profiles through the Ca planes are shown: one at the interface (left) and the second one four unit cells further (right). Reprinted from [44].

tures. Looking down: this plane would be part of the infinite layer, with no oxygen, while looking up it belongs to the perovskite structure, with an oxygen atom at the centre of the Ca square to complete the octahedral cage, forming the $CaTiO_3$ unit cell.

Similarly to $LaAlO_3/SrTiO_3$ (Section 1.3), the interface is between a non-polar plane ($SrTiO_3$) and a polar one ($CaCuO_2$). Consequently, an electric field should build up inside the $CaCuO_2$ layers, leading to a potential diverging with the $CaCuO_2$ thickness. A hard x-ray photoelectron spectroscopy study showed that this field is not present in $CaCuO_2$ [128], thus something should be at play in order to compensate for it. Direct charge transfer from the valence band of $CaCuO_2$ ($SrTiO_3$) into the $SrTiO_3$ ($CaCuO_2$) conduction band to compensate the charge of the planes is not possible because the valence band of $CaCuO_2$ ($SrTiO_3$) is lower than the conduction band of $SrTiO_3$ ($CaCuO_2$) [128]. A purely ionic mechanism has been proposed, such as the transfer of 1/2 oxygen atom per unit cell from the top SrO layer into the Ca plane at the interface, leading to a $(CaO_{0.5})^+$ plane instead of $(Ca)^{2+}$, compensating by this means

the growing electric field in $CaCuO_2$ [128].

Therefore, the polar discontinuity between $CaCuO_2$ and $SrTiO_3$ seems to already promote the incorporation of oxygen at the interface; using highly oxidising growth conditions increases the amount of interfacial oxygen atoms, which dopes the system and eventually leads to superconductivity.

2.3.2 Superconductivity in $SrTiO_3/CaCuO_2$

Superconductivity has been reported in both $SrTiO_3/CaCuO_2$ superlattices and bilayers, with a critical temperature of up to 50 K [43, 44, 131]. As illustrated in Fig. 2.7a, only samples with the CuO_2-Ca-TiO_2-SrO stacking order at the interface show superconductivity. If the order is inverted (TiO_2-

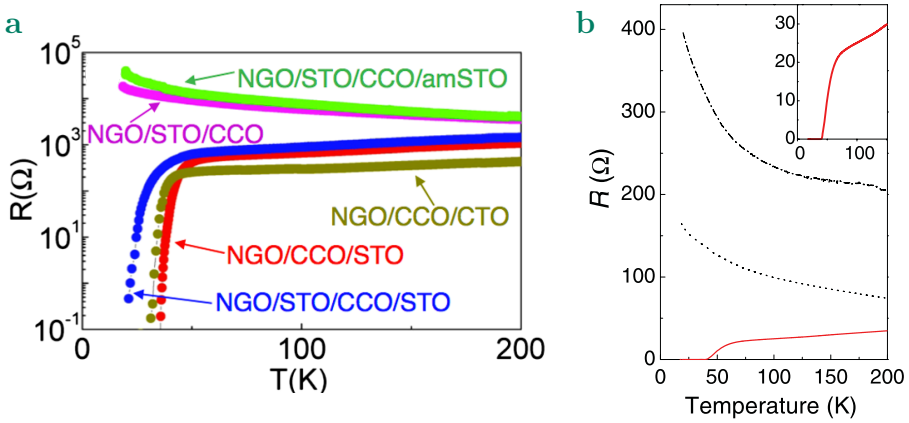

Figure 2.7: Resistance as a function of temperature revealing the superconducting transition in $SrTiO_3/CaCuO_2$. **a** Transport measurement for various heterostructures, with different types of stacking (note that the authors [43, 44] use a substrate/film notation for the stacking order while we use a film/substrate notation in the present manuscript). This demonstrates the relevant role of the CuO_2-Ca-TiO_2-SrO interface for superconductivity in this system. Reprinted from [44]. **b** $R(T)$ of superlattices for different oxidising growth conditions: dotted-dashed line shows a sample grown in pure oxygen, dotted line for similar conditions with a quench in 1 bar of O_2 and finally the solid line exhibits a superconducting behaviour with highly oxidising atmosphere used during the growth (O_2+12% of O_3). Reprinted from [43].

SrO-CuO_2-Ca) the heterostructures are semiconducting. A set of experiments has revealed that $SrTiO_3$ can be replaced with $CaTiO_3$, provided the stacking sequence is preserved; conversely, topping $CaCuO_2$ with amorphous $SrTiO_3$ (α-$SrTiO_3$) does not lead to superconductivity.

In order to obtain a zero-resistance state another condition has to be fulfilled: the presence of additional oxygen atoms in the last Ca plane. Indeed, superconductivity was observed only for structures showing additional oxygen

atoms in the Ca layers at the interface (see Fig. 2.6); the presence of apical oxygen introduces doping into the neighbouring CuO_2 planes. In this case $CaCuO_2$ plays the role of the CuO_2 block, while the interface between $CaCuO_2$ and $SrTiO_3$ acts as a charge reservoir. The insertion of apical oxygen atoms is achieved by using a highly oxidising atmosphere during the PLD growth; Di Castro and co-workers are using a mixture of pure oxygen with 12% of ozone at a total gas pressure of 1 mbar [43, 44]. In Fig. 2.7 the resistance as a function of the temperature is shown for a superlattice grown in pure oxygen (dotted-dashed line) revealing a semiconducting behaviour, while for a similar structure grown in the O_2/O_3 mixture (solid line) the resistance falls to zero below 40 K.

$SrTiO_3/CaCuO_2$ superlattices show multilayer effects similar to the other cuprates [43] indicating that superconductivity occurs in few CuO_2 planes close to the interface. Another observation, pointing toward interfacial superconductivity is brought to light by electron energy loss spectroscopy (EELS) (coupled to STEM) measurements of the O K-edge (shown in Fig. 2.8a). Close to the

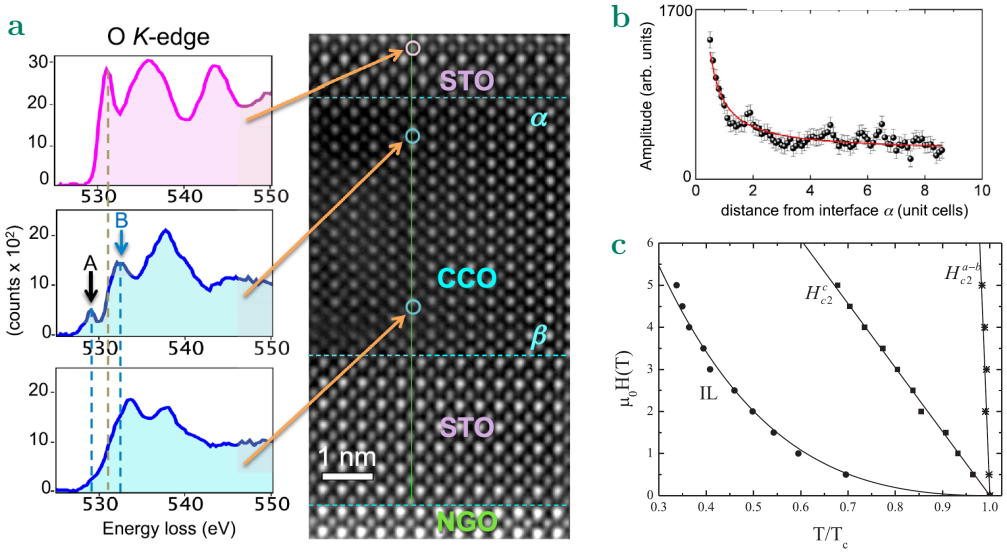

Figure 2.8: Interfacial superconductivity in $SrTiO_3/CaCuO_2$. **a** STEM/EELS measurement of the O K-edge for different depths along the $SrTiO_3/CaCuO_2/SrTiO_3$ system. The presence of the A-peak reveals the presence of delocalised holes near the CuO_2-CaO_x-TiO_2-SrO interface (top), vanishing within few unit cells as seen in **b** where the amplitude of this peak is shown as a function of the distance from the interface. On the other side, close to the TiO_2-SrO-CuO_2-Ca interface (bottom), these holes are not present. This localised doping points toward confined superconductivity (both reprinted from [44]). **c** Critical field/temperature phase diagram of the bilayer, showing the strong anisotropy between the parallel and perpendicular magnetic field directions (reprinted from [129]).

superconducting interface, one measures an additional peak in the EELS spectra, labelled as the A-peak, which is usually associated with delocalised holes in HTS: the peak intensity decreases as one moves away from the interface (Fig. 2.8b) indicating that the doping is confined within 2-3 u.c.

Other experiments have probed the orbital polarization of Cu for superconducting and non-superconducting interfaces: the presence or absence of the apical oxygen determines the degree of crystalline isotropy relevant for the occupation of the $e_g - 3d$ orbital states [43]. Analysis of transport measurements in perpendicular and parallel magnetic fields (Fig. 2.8c) reveals highly anisotropic superconducting coherence lengths between in-plane and out-of-plane directions [126, 129].

All these results point toward interfacial superconductivity for the $SrTiO_3/CaCuO_2$ system. Appearance of superconductivity is linked to the presence of apical oxygen in a single atomic plane, doping the underneath CuO_2 planes, solely at the interface. Such crystalline structure is very similar to the one of multilayer cuprates as well as the one of crystals and multilayers observed for superconducting infinite-layer related compounds.

Chapter 3

Growth and characterisation

3.1 Sample growth

The first step towards the study of our physical system is the growth of the heterostructures: this is the subject of this section. The thin films studied in the present work are deposited using a PLD method which is a widely used growth technique for oxide thin films. It belongs to the broad family of the physical vapor deposition (PVD) techniques.

The working principle of PLD is the following: extremely short pulses from a laser source ablate a target made of the desired material; the ejected species travel towards the substrate in a feather shape (the plume) and once landed, they condense forming the thin film. This process is schematically illustrated in Fig. 3.1. The physics behind this technique is described in the next part followed by a brief description of the system used in our lab.

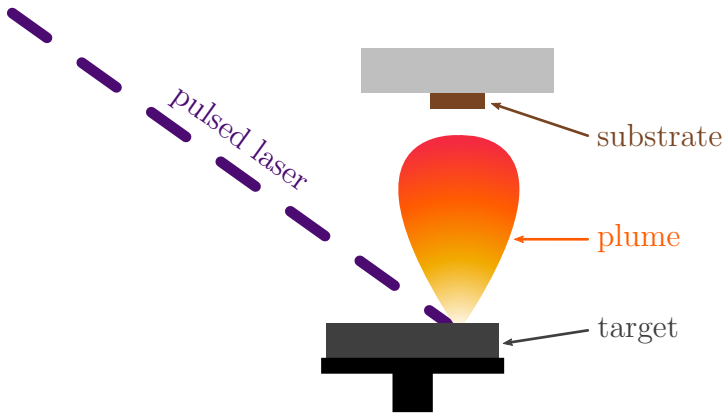

Figure 3.1: Scheme of the ablation process in pulsed laser deposition system.

3.1.1 Pulsed laser deposition: principle

The physics behind PLD is complex and a full description of the processes leading to the growth of a layer is beyond the scope of this chapter. However, it is important to capture the basics of this technique in order to understand the different effects of the various growth parameters. Thin film deposition by PLD can be divided into three steps [132]:

1. Ablation of the target and plasma formation
2. Expansion of the ablated species
3. Deposition on the substrate

1. Ablation of the target and plasma formation In all ablation processes induced by ions, electrons or photons, there are four primary mechanisms describing the particle ejection: the thermal, electronic, macroscopic and collisional mechanism [133].

For a laser-solid interaction, **thermally** activated ablation occurs when the energy of a laser pulse overcomes the latent heat of the target material. Given the power of a laser source, it implies that the duration of a pulse has to be longer than the time required to thermally vaporise an appreciable quantity of material (few nanoseconds per pulse). This implies the existence of a threshold energy below which the target is not ablated. For laser energies higher than the threshold, the target is ablated and deposition of the ejected material becomes possible. If the thermal energy of the ejected species is sufficient, ionisation can occur and a plasma can be formed above the target. The proportion of ionised particles, depending on the temperature, is given by the Saha equation [134]:

$$n_i = \sqrt{2.4 \cdot 10^{15} \cdot n_n \cdot T^{3/2} \cdot e^{-\frac{U_i}{k_B T}}}. \tag{3.1}$$

Where n_i and n_n are the densities (in cm^{-3}) of ionised and neutral particles respectively and U_i (in eV) the first ionisation energy. At typical plasma temperature (∼10'000 K) Eq. 3.1 gives a fraction of ∼80% of ionised particles indicating that a plasma is formed.

The ablation of the target does not occur only through thermal vaporisation. Indeed, various light-matter processes can lead to **electronic** excitations or ionisations which are not thermally activated, thus, contributing to the plasma formation. For example, a strong electron depletion could induce a Coulomb explosion, due to the important repulsion between ions. Other examples leading to ejection of atoms are formation of defects or surface plasmon excitations.

Due to the various effects taking place at the target surface, **macroscopic** mechanism could also play an important role. Exfoliation of macroscopic flakes

is possible when materials with a high thermal expansion coefficient are subject to repeated temperature changes, because of the pulsed nature of the ablating laser. Melting of the target surface can also lead to the ejection of large droplets.

The last of these primary mechanisms relies on ablation of the target by **collision**. In pulsed laser deposition, this is a secondary mechanism, coming from particles back-scattered onto the target (see step 2.).

For the three step model presented here, one assumption is that the laser-solid interactions and the plasma formation occur at the same time [132]. Indeed, their time scale (tens of nanoseconds or less) is much shorter than the one of the plume expansion ($\gtrsim \mu$s). Within this first step, ablated particles are not only interacting with each other (collisions) but also with the laser. This means that the plasma formation is enhanced by the laser-plasma interactions inside the plume too. Without going into details, two photon absorption processes prevail: inverse bremsstrahlung and photoionisation. The former increases the kinetic energy of the electrons promoting ionisation and excitation inside the plume, while photoionisation creates more ionised particles by absorbing a photon. As a consequence, the light-plasma interaction allows the plasma to self-sustain, therefore reducing the effect of recombination.

2. Expansion of the ablated species Once the plasma is formed it travels in the growth chamber. Its kinetic properties before reaching the substrate depend strongly on the initial state of the particles (density and velocity) as well as on the target environment. Obviously, the former depends on the laser pulse particularities, especially its fluence F (energy per unit area) [135]. In the case of low particle density, the ejected species move away from the target ($v > 0$) in a free-flight regime, whereas for high density, the ejected species can reach thermal equilibrium because of collisions. The region where such equilibrium occurs forms a gas/liquid layer close to the target surface called the Knudsen layer (KL), illustrated in Fig. 3.2. This expansion, sometimes called the secondary mechanism, can be described in terms of outflow or effusion. The latter possibly leading the Knudsen layer formation. In both cases the back-scattered atoms can be reflected or absorbed (recondensation) by the target.

Critical to the plasma expansion is the growth atmosphere. Very often, the thin film deposition is done in a reactive gas (e.g. in oxygen for oxide growths). The presence of this gas at a given pressure increases the collision rate and affects the plasma expansion. The work by S. Amoruso and co-workers [135], in which they grew $La_{0.7}Ba_{0.3}MnO_{3-\delta}$ by PLD, is an instructing example. Using an optical emission spectroscopy (OES) technique they are able to obtain time and space resolved images of the plume expansion, for various growth pressures (see Fig. 3.3a).

In a vacuum the plume expands freely because the collision rate is low as

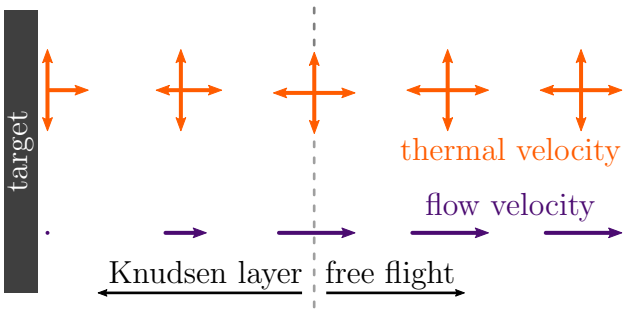

Figure 3.2: Schematic representation of the Knudsen layer, adapted from [133]. The orange (top) arrows represent the kinetic velocity whereas the purple ones (bottom) the flow velocity. In the KL melted by the laser pulses, the particles accelerate toward the vacuum and thermalise because of collisions. Afterwards the KL particles enter a free-flight regime as long as growth is under vacuum.

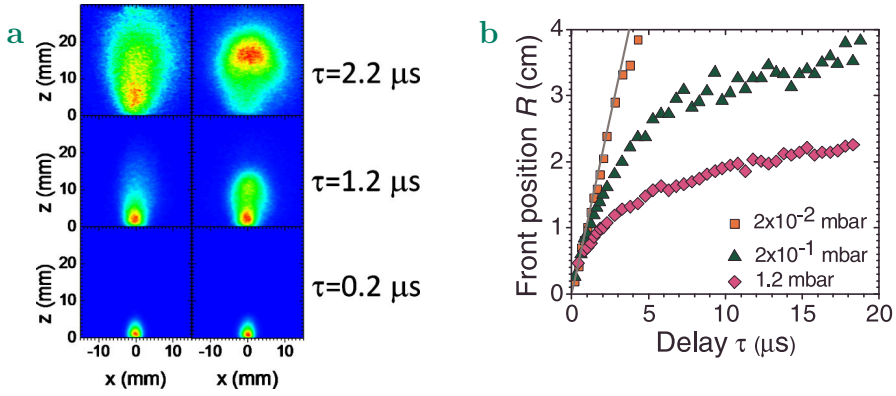

Figure 3.3: Plume expansion immediately after the laser pulse for various oxygen pressure backgrounds. **a** Space and time resolved plume expansion for two different pressures: 10^{-8} mbar (left) and $2 \cdot 10^{-2}$ mbar (right) acquired by OES. **b** Position of the plume front as a function of time. The straight grey line represents the free expansion (in vacuum). Both reprinted from [135]

seen in the left part of Fig. 3.3a (for this pressure a mean free path, l, of few kilometres can be estimated[1]). An oxygen background pressure of $2{\cdot}10^{-2}$ mbar (l is a few millimetres), induces important changes: in the right panel of Fig. 3.3a, a redistribution of the emission to the front of the plume can be observed. However, the dynamic is still comparable to the one in vacuum as shown by similar front position curves in these two conditions (Fig. 3.3b). For pressures 10 and 100 times higher (l is respectively hundreds and tens of micrometres), the plume front is slowed down (green triangles and pink diamonds) which can eventually lead to the complete thermalisation of the plume. This is crucial,

[1]The mean free path is estimated using that $l = \frac{RT}{\sqrt{2}\pi d^2 N_A}$ with R the universal gas constant, T the temperature (room temperature is used), $d = 2.93$ Å the O_2 molecular diameter, N_A the Avogadro's number and P the pressure.

as it completely modifies the way ablated species interact with the ambient gas. An important point to mention is that for a qualitative understanding, the growth details are not essential as the same effect is observed for the deposition of different materials [135–139].

Fig. 3.4 shows a spectral-resolved OES acquired during the growth of a $SrTiO_3$ thin film, from the thesis of R. Groenen [139]. As observed, at higher

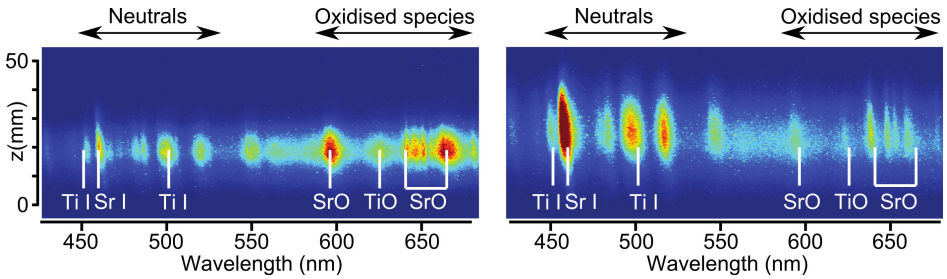

Figure 3.4: Spectral-resolved OES of an $SrTiO_3$ target ablation for two different oxygen pressures: 10^{-1} mbar (**left**) and 10^{-2} mbar (**right**). Reprinted from [139]

oxygen pressure (left) more oxidised species are present in the plasma than at lower pressure (right). This illustrates that the stoichiometry of the species reaching the substrate depends on the atmospheric conditions. This example is for oxygen but other background gases may lead to similar effects depending on the particle-gas interactions, meaning that the gas itself is of paramount importance for proper growth of a specific material. As the kinetics of the ablated particles are affected by the environment, heavy and light atoms will not behave identically and the plume stoichiometry can deviate from the one of the target. This is particularly true for the oxygen content during the growth of oxides in oxidising atmospheres. It is worth noting that the ratio of heavy/light atoms depends also on the laser fluence as light atoms will be faster but more easily deviated than the heavy ones.

Another parameter affecting the plasma expansion is the substrate temperature: high temperatures dilute the background gas around the substrate and consequently the plume front can expand more easily [135]. Its effect is probably less significant than the pressure but this has to be kept in mind for the next part as the temperature is shown to be crucial for the growth.

3. Deposition on the substrate After travelling in the growth chamber, ablated species and derived compounds resulting from interactions with the background gas arrive at the substrate surface. Herein, multiple processes can occur as illustrated in Fig. 3.5a:

> **arrival:** An atom[2] arrives on the substrate surface.

[2]It is not necessarily a single atom, as said in the main text it can be any compound resulting from the ablation and the plasma expansion; the term atom is used for simplicity.

> **surface diffusion:** If its energy is high enough, the atom can diffuse on the surface.
> **nucleation:** When it encounters other atoms on that surface they can bind together and start the nucleation of a new crystal: this is the crystal growth. Some particular location can be present (here a **step site** is shown) promoting for example localisation of atoms.
> **re-evaporation:** Some atoms can be re-evaporated from the substrate if their energy is too high (e.g. temperature close to the boiling point of the material, high kinetic energy or high vapour pressure elements).
> **interdiffusion:** Depending on the chemistry at the surface, interdiffusion can occur with the underneath layer (substrate or film).
> **ablation:** Material will be ablated for high kinetic energies of the arriving atoms. This leads to damages of the substrate/film which are generally not desired.

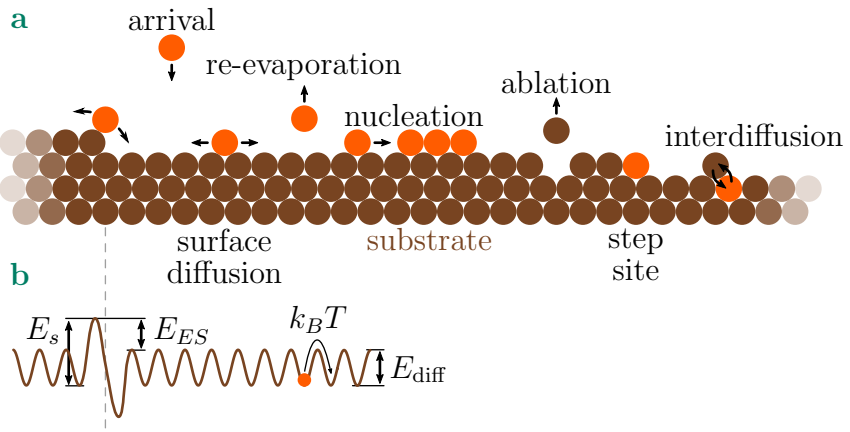

Figure 3.5: **a** Scheme of the different processes at the crystal (substrate or film) surface during the growth of a thin film. **b** Representation of the surface and step potential for the atoms arriving on the crystal. E_s, E_{ES}, E_{diff} and k_BT are defined in the main text. Adapted from [140, 141]

To grow a new layer of material, the ablated atoms have to arrive on the substrate, diffuse over the surface and nucleate to form a full layer. It depends on the kinetic energy with which they reach the surface, but more importantly on the substrate temperature as they will rapidly thermalise. In order to understand how the atoms diffuse at the surface, one has to consider its surface potential. It can be schematically represented with periodic barriers aligned with the lattice of the underneath layer as shown in Fig. 3.5b. From surface diffusion theory [142] the rate (Γ) of jump from one site to the other is a thermally activated process given by:

$$\Gamma = \nu \cdot e^{-E_{\text{diff}}/k_BT}. \tag{3.2}$$

Where ν is the attempt frequency which is basically the vibrational frequency of recently arrived atoms. E_{diff} is represented in Fig. 3.5b and is the diffusion barrier energy in competition with the kinetic energy (the thermal energy $k_B T$). If the substrate temperature is too low, E_{diff} dominates and the diffusion is small. In the extreme case, ablated particles stay where they land, leading to amorphous growths. As seen in Fig. 3.5b the potential at an atomic step can be slightly different, modifying the diffusion around it. The surface potential depends on the coordination number or more generally on the number of surrounding bonds [143, 144]. Consequently, it is not surprising that the potential of the upper terrace, where the adatom is in contact only with the underneath layer, is different from the step potential, where the adatom is also bonded to the step atoms (higher number of bonds). Particles on the upper terraces can be reflected at the step edge because of the Ehrlich-Schwöbel barrier (E_{ES}) [145–147]. Obviously, this has been described for a single particle diffusing over the surface, although many of them arrive and diffuse together. When the incoming flow of material is important, particles will also interact together on the surface (attraction/repulsion, nucleation). These different diffusion phenomena will strongly influence the way a material can grow and different growth morphologies are possible. Before describing the three main possibilities, we introduce the diffusion coefficient [142, 148]:

$$D = \frac{\Gamma a^2}{z} = \frac{\nu a^2}{z} \cdot e^{-E_{\text{diff}}/k_B T}, \tag{3.3}$$

obtained from Eq. 3.2 with z the coordination number and a the intersite distance. Typically for a given flow of particles (F) the length over which an adatom can diffuse is given by [148, 149]:

$$\lambda \propto \left(\frac{D}{F}\right)^{\frac{\gamma}{2}}. \tag{3.4}$$

With γ an exponent that depends on the diffusion processes. With this in mind we can discuss the different growth morphologies. The first one is called the 3D or multilayer growth. This is the case when diffusion is small and effects such as the Ehrlich-Schwöbel barrier are not negligible. The diffusion length (λ) is small compared to the distance between consecutive steps (L) leading to the formation of small islands. Consequently, the growth speed in the direction perpendicular to the substrate dominates over the in-plane diffusion, as illustrated in Fig. 3.6. However when $\lambda > L$ the atoms can explore all the terrace between two steps and this is a necessary condition to have 2D growth. Two types of 2D growth exists depending on the value of λ. For long range diffusion the adatoms are mainly trapped at a step edge (step flow) and the steps move further as schematically represented in Fig. 3.6. At intermediate values of λ, islands can form but they expand to fully cover

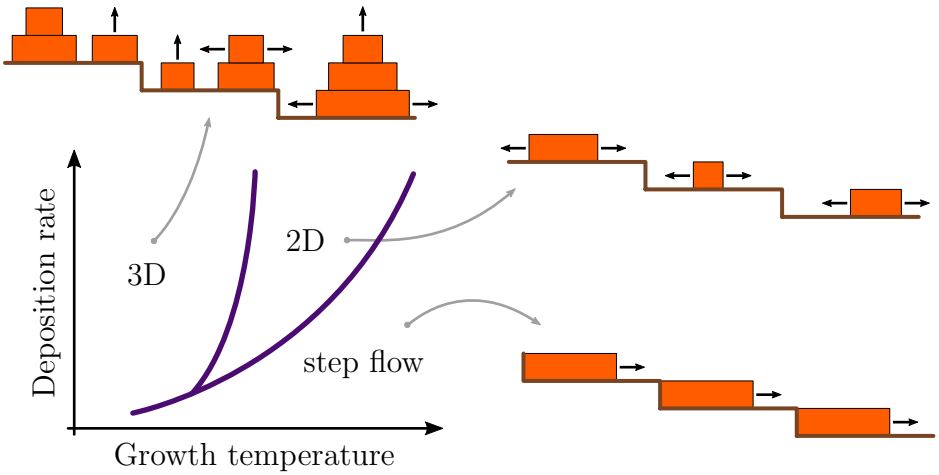

Figure 3.6: Description of the different growth mechanisms depending on the temperature and the deposition rate. The black arrows on the schemes represent the growth direction of different island/layer. Adapted from [148, 150]

the underneath layer before creating new islands on top. This is called the layer-by-layer growth and results in a 2D morphology as well.

Once particles have reached the substrate, the growth mechanisms are principally controlled by diffusion phenomena. Consequently, growth temperature and particle flow[3] are two key parameters to optimise the growth of a given material.

3.1.2 Pulsed laser deposition: our system

The aim of this section is to give more information concerning the specific PLD used for the growth of the thin films deposited in-house by detailing the reachable growth conditions. First of all, our system is composed of three main parts: the excimer laser, the load-lock (LL) and the growth chamber (GC).

The load-lock is a chamber reaching a vacuum of the order of $\sim 10^{-6}$ mbar separated by a gate valve from the GC. It is used firstly as a first pumping stage to insert a substrate in the GC without breaking its high vacuum $\sim 10^{-8}$ mbar. Secondly, the LL allows the annealing of the substrates to remove adsorbates that vaporise below 300°C, a step that avoids contamination of the GC during substrate heating. This step is also used to cure the silver paste required to fix the substrate on its holder (see below).

From the LL the substrate is moved with a transfer arm into the growth chamber and is mounted, facing down, at a vertical distance (d_{TS}) variable between 3 and 7 cm above the target. The target is mounted on a rotating carousel allowing the selection of different compounds (6 targets) in order to

[3]The particle flow depends on the plume expansion as well as the laser repetition rate which is the time between two laser pulses.

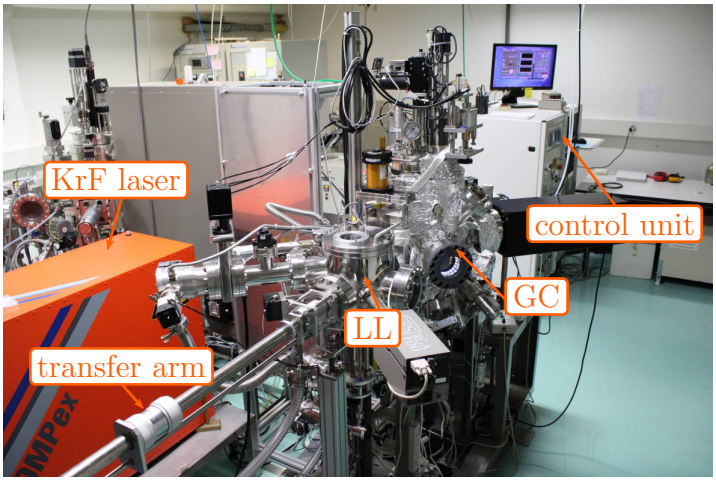

Figure 3.7: Picture of the PLD system used for all the growths in Geneva.

grow multilayers. In the present work different targets are used: $CaCuO_2$ and $SrCuO_2$ are compressed powder pellets from *PI-KEM Limited* and $SrTiO_3$ is a commercial single crystal from *CrysTec GmbH*.

Ablation is realised with a pulsed KrF excimer laser, with a wavelength of 248 nm (in the ultraviolet) and a pulse duration of 25 ns, for which the repetition rate can be controlled up to 50 Hz. The laser beam, after following an optical path with an aperture and mirrors, is focused onto the target by a lens leading to a typical spot size of 7 mm^2 and a laser fluence between 0.5-1.5 J/cm^2.

Two types of atmosphere are mainly used for the depositions: the first one is pure molecular oxygen (O_2) and the second is a mixture of oxygen and ozone (O_2/O_3). The latter has a higher oxidising power [151, 152]. Instead of oxygen and ozone, the use of nitrous oxide (N_2O) as a highly oxidising agent is possible too. In all cases the pressure inside the chamber can be controlled between base pressure (around 10^{-8} mbar) and few millibars. Above 0.05 mbar the gas flow can be regulated between 0 sccm and 20 sccm independently of the pressure as the pumping rate is regulated using a butterfly valve.

In order to produce the O_2/O_3 mixture two types of ozone generators were used in this study:

1. Ozone generator from *Samco Inc.* According to the company specifications and confirmed by mass spectrometer measurements the output mixture is fixed to $5\%O_3/95\%O_2$ at a flow rate of 20 sccm. The generator is fed with pure oxygen (purity 5.0). In order to control the oxidation power in the growth chamber one has to tune parameters such as pressure and gas flow.

2. Atlas UHC from *Oxidation Technologies, LLC.* The percentage of ozone can be roughly controlled between 5% and 20% at a flow rate of 20 sccm

by controlling the power of the generator (see Appendix A). This generator is fed with a mixture of 0.5%N_2/99.5%O_2 (purity of 6.0). N_2 is required to preserve the generator from oxidation.

Oxygen/ozone is delivered to the chamber using stainless steel tubing. The position of the delivery tube (inner diameter 2.0 mm) inside the chamber is controlled by a wobble stick, allowing us to change the tube position as well as the tube-to-substrate distance.

The substrate is pasted on a chromium plate with silver paste (see Fig. 3.8) and can be heated during the growth at a temperature T_g, between 400°C and almost 1000°C, using an infrared (IR) laser (a Nd:YAG laser). The Cr-plate

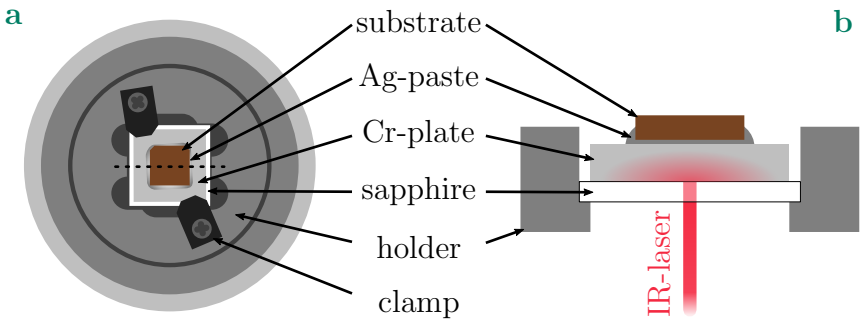

Figure 3.8: Scheme of the substrate holder used for all the growth in the PLD. **a** Top view of the holder. **b** Cross section along the dashed line in **a** detailing the geometry used to heat up the substrate with an IR-laser during the growth.

is clamped to the substrate holder: in between a sapphire plate thermally isolates the Cr-plate from the holder but allows the IR-laser to go through as illustrated in Fig. 3.8b. The substrate temperature in the GC is measured with a set of two pyrometers. A heating ramp of 25°C/min is usually used to reach the above-mentioned temperatures.

After the deposition, samples are usually quenched to room temperature by abruptly switching off the IR-laser while keeping the same growth atmosphere to limit the formation of oxygen vacancies. A gentle cooling rate can also be used but no obvious differences have been observed between samples differently cooled.

3.1.3 Sample patterning

In some cases, especially for electrical transport measurements (Section 3.2.3), a particular shape is required for the device to be measured properly. In the present work, this is achieved using a pre-patterning technique, widely used for the study of the $LaAlO_3/SrTiO_3$ interface [25, 153] and briefly described in this section.

The different steps of the fabrication process are illustrated in Fig. 3.9. Using standard photolithography, a resist mask is patterned on a bare sub-

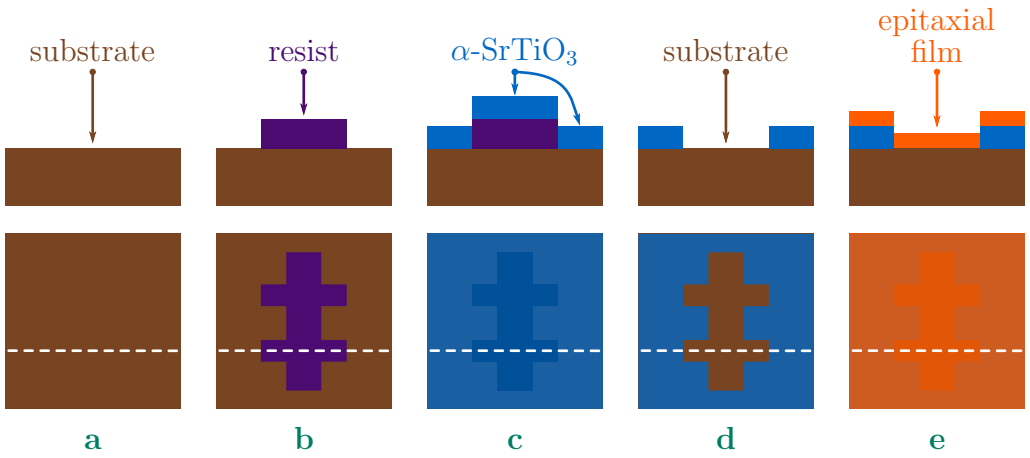

Figure 3.9: Pre-patterning process as described in the main text. **a** Bare substrate (brown). **b** Photoresist mask (purple) after the photolithography. **c** Deposition of α-$SrTiO_3$ (blue). **d** After removing the photoresist, the substrate is left with a hard-mask composed of α-$SrTiO_3$. **e** The thin film (orange) grows epitaxially only where there is no α-$SrTiO_3$. The side view of the structure is shown in the top schemes taken along the white dashed line show in the top views (bottom schemes).

strate (**a** and **b**). Then an amorphous and insulating material, typically $SrTiO_3$ (α-$SrTiO_3$), is deposited at room temperature by PLD (**c**). The resist is lifted-off, leading to a α-$SrTiO_3$ hard-mask leaving openings on the substrate crystalline surface only in the desired areas (**d**). The final step consists in the deposition of the thin film which grows epitaxially only in the crystalline regions of this pre-patterned substrate (**e**).

For $LaAlO_3/SrTiO_3$ this method is well suited, as non-epitaxial $LaAlO_3$ on $SrTiO_3$ is insulating, but if the deposited thin film is a poor insulator or even metallic when non-epitaxial or amorphous then the use of a hard-mask can be an issue.

This method is particularly convenient for sensitive materials, as it avoids any photolithographic steps on the deposited thin film. Indeed, as it will be shown in Section 4.4, the chemicals used during the standard photolithographic steps can be aggressive for the infinite-layer cuprates studied in this work. Moreover, a hard-mask avoids the use of ion-milling that could damage the substrate, or induce oxygen vacancies, especially in $SrTiO_3$ [153, 154]

3.2 Sample characterisation

Surface and structural quality as well as electronic properties are characterised using the following techniques: atomic force microscopy, X-ray diffraction and electrical transport.

3.2.1 Atomic force microscopy (AFM)

AFM is a local probe technique that measures atomic, electrical and magnetic forces at the surface of a sample at the nanometre scale level [155]. In the present work AFM is used to investigate the surface morphology of our samples.

The working principle of AFM hinges on atomic attraction/repulsion between atoms at the surface of a sample and the ones at the end of a tip with nanometric radius mounted on a cantilever. The attractive force is considered to be mostly coming from the van der Waals effect, especially at large distances [156]. However short-range interaction due to overlap of the electrons wave functions can also lead to attraction. The repulsive force originates from both Pauli exclusion principle and electrostatic repulsion of the inner shells electrons [156]. The sum of these interactions leads to the force profile illustrated in Fig. 3.10. Depending on the tip-sample distance the interaction

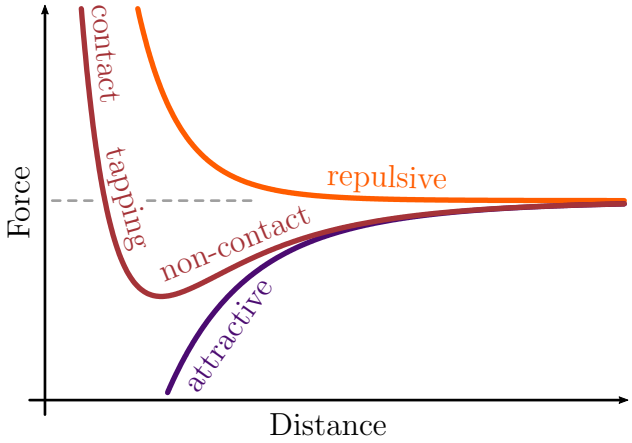

Figure 3.10: Typical force-distance profile between atoms at the sample surface and the ones at the end of the AFM tip. The orange line shows the repulsive force while the purple one the attractive case, the resulting force is shown in brown. The dashed line indicated the zero of the force.

is different, giving rise to three operating modes. The first one is the **non-contact** mode, for large tip-sample distances. Because this mode was not used, in this work, the focus is done on the two others: **contact** and **tapping** modes. In both cases the measurement of the topography is achieved by scanning the AFM tip above the sample surface (x, y).

In **contact** mode the tip is "touching" the sample during the scan: the tip-sample distance is short and the dominating force is the repulsion. The tip height (z) over the surface is adjusted by a piezoelectric element in order to keep its interaction force with the sample constant (equivalently the cantilever deflection). Deflection is measured with a laser beam reflected on the back of the tip and a feedback loop maintains the surface-tip distance accordingly. This measurement mode is similar to the way a blind person reads a page

written in Braille: the page being the sample and the finger the microscope tip. This mode allows one to extract the topography $z(x, y)$ of a sample. Moreover, as the tip is in contact with the surface, it allows one to locally "clean" the sample and see, for example, if particles found on the surface are mobile or not.

The setup for **tapping** mode is similar but the tip is further away from the surface and another piezoelectric element makes the tip vibrate near its resonant frequency. While the tip scans the surface, the oscillating amplitude is kept constant by adjusting the tip height, similarly to the contact mode (see Fig. 3.11). Indeed, when the tip-sample distance is modified (Fig. 3.11

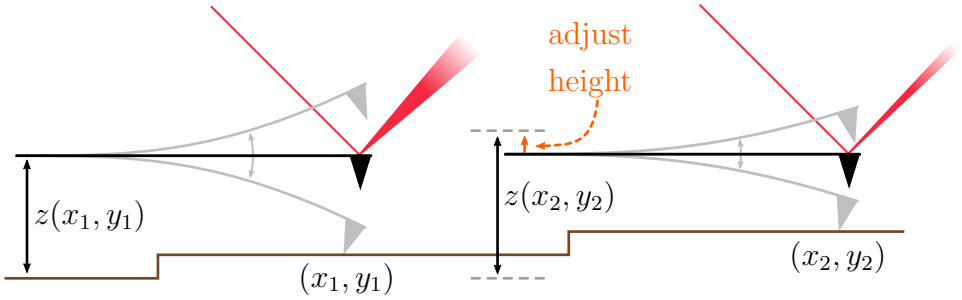

Figure 3.11: Scheme of the working principle for tapping mode. The left Figure is showing the fixed amplitude, measured by the broadening of the laser spot. When the tip goes on the step above (right Figure), the amplitude is reduced and the height has to be adjusted (small arrow) in order to keep the same amplitude as in the left Figure.

right) the interaction force changes and alters the oscillating amplitude and frequency. Adjusting the tip height allows the amplitude to be kept constant and one thus obtains the surface morphology $z(x, y)$. Tapping mode not only gives the topography: looking at the phase difference between the tip excitation and the reflected signal, information on the material can be obtained. For example, a phase contrast can indicate the presence of different materials on the surface (e.g. mixed termination, segregation).

A topographic image gives a qualitative information of the surface, revealing if the thin film surface reproduces the morphology of the substrate or if the growth introduces grains. To compare different samples quantitatively, the surface roughness is a useful value that can be extracted from the topographic image. More details concerning the AFM data treatment and roughness extraction are given in Appendix B.

In the present work, atomic force microscopy measurements were performed with two different systems: a *Bruker* MultiMode and an *Asylum* MFP-3D Infinity AFM. In both cases *Bruker* TESPA-V2 tips with a spring constant of ∼37 N/m and a resonant frequency around ∼320 kHz were used to acquire sample topography.

3.2.2 X-ray diffraction (XRD)

X-ray diffraction is based on the principle of interference: when an electromagnetic wave recombines after travelling through two different paths, it can experience a constructive or destructive interference. A wave with a wavelength λ similar to the interatomic distance (angstroms range) diffracts on atoms. As illustrated in Fig. 3.12, the wave reflected on the second atomic plane travels a longer path than the wave reflected from the first plane. Along

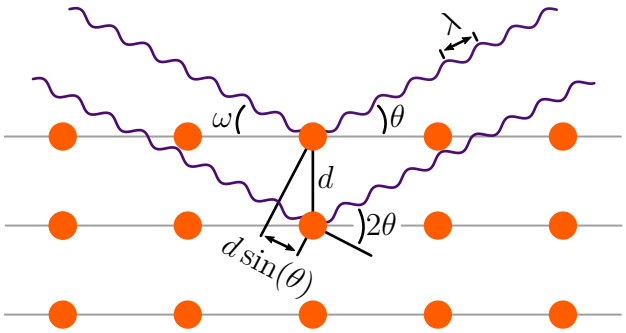

Figure 3.12: X-ray beam (purple wave) arriving on a crystal (ball) with an incident angle ω and diffracted by the latter. The extra path ($d\sin(\theta)$, for $\theta = \omega$) travelled by the wave reflected on the second atomic plane is schematised by the double arrow.

this path difference ($2d\sin(\theta)$, with θ the incident angle and d the distance between two atomic planes) the wave accumulates an extra phase compared to the wave reflected on the first plane. If this phase is a multiple of 2π or equivalently if the extra path is a multiple of the wavelength ($n\lambda$) the two waves interfere constructively. This leads to the well-known Bragg's law:

$$n\lambda = 2d_{hkl}\sin(\theta_{hkl}). \tag{3.5}$$

The Miller's indices hkl indicate the crystalline plane for the reflection. This relation can be generalised in the reciprocal space[4] to [157]:

$$\vec{q} = \vec{G}_{hkl} \tag{3.6}$$

Where $\vec{G}_{hkl} = h\vec{a}^* + k\vec{b}^* + l\vec{c}^*$ is a vector of the reciprocal lattice and $\vec{q}$ is the scattering vector given by $\vec{q} = \vec{k}_{out} - \vec{k}_{in}$, $\vec{k}$ being the wave vector of the incident (in) and reflected (out) X-ray beam. Their direction is determined

[4]The reciprocal space is defined by a set of vectors $\vec{a}^*$, $\vec{b}^*$ and $\vec{c}^*$ respecting the relations: $\vec{a}^* \cdot \vec{a} = 2\pi$, $\vec{a}^* \cdot \vec{b} = 0$ and $\vec{a}^* \cdot \vec{c} = 0$ (the same for $\vec{b}^*$ and $\vec{c}^*$) with $\vec{a}$, $\vec{b}$ and $\vec{c}$ the primitive vectors of the crystal lattice. For more details see [157].

by the position of the source and the detector respectively, meaning that $\vec{q}$ is specific to the instrument position while $\vec{G}_{hkl}$ depends on the measured crystal.

The usual measurements performed using XRD are: $\theta-2\theta$ scan and rocking curves (ω scan). These two measurements are described in the following.

$\theta - 2\theta$ scan Fig. 3.13a illustrates a $\theta - 2\theta$ scan viewed in the reciprocal space. When the incident and diffracted angles increase (represented by the arrows with the colour gradient), the length of $\vec{q}$ increases, keeping its direction unchanged. Each time $\vec{q}$ reaches a point in the reciprocal lattice, i.e. $\vec{q} = \vec{G}_{hkl}$, the interference from the scattered waves is constructive and the measured intensity is non-zero. For an ideal and infinite crystal the signal would be a series of peaks at positions representing a specific periodicity of the crystal. A calculated XRD pattern for a $NdGaO_3$ crystal along the $[hh0]_o$ direction is shown in Fig. 3.13b. Extracting the θ_{hkl} value for each reflection allows the

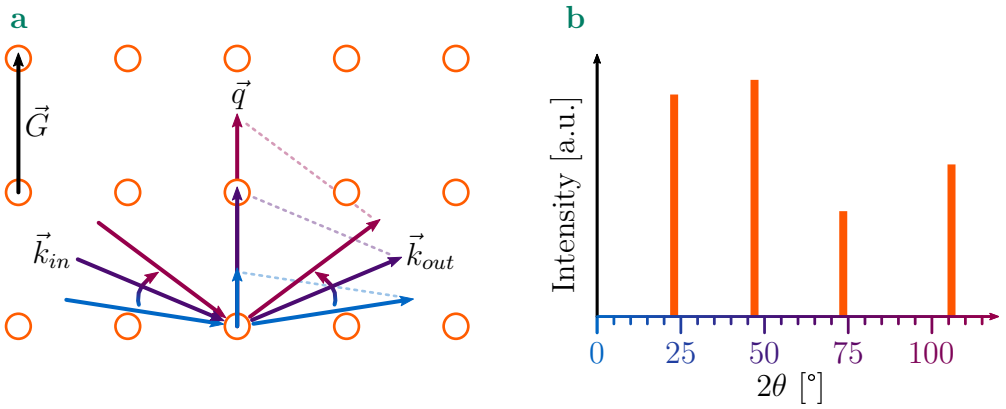

Figure 3.13: Working principle of a $\theta - 2\theta$ scan. **a** Reciprocal space representation of the evolution of $\vec{q}$ during the scan, illustrating the fact that only for $\vec{q} = \vec{G}_{hkl}$ the measured intensity is maximal. **b** Calculated XRD pattern for a $NdGaO_3$ crystal along the $[hh0]_o$ direction. The relative intensities and the θ value for each reflection are calculated using the VESTA 3 software [158] from the crystallographic structure of $NdGaO_3$. In both figures the arrows with the colour gradient represent the increase θ during a scan.

calculation of the d_{hkl} distance using the Bragg formula. With this technique it is therefore possible to estimate the lattice parameters of the compounds.

A thin film grown over a substrate is not an infinite crystal, due to its finite thickness, additional interference effects occur, introducing intensity oscillations around the plane reflection peak. As these oscillations are linked to the finite thickness of the crystal, they are analysed to determine the film thickness (t). Using the angle position of two consecutive maxima, the thickness can be extracted with the formula:

$$t = \frac{\lambda}{2} \frac{1}{\sin(\theta_{n+1}) - \sin(\theta_n)} \tag{3.7}$$

The presence of these oscillations is also a sign of the high crystalline quality of the samples, as they require a high crystalline coherence throughout the film thickness as well as a well defined thickness.

Note that the $\theta - 2\theta$ scans in the present work were analysed with the *InteractiveXRDFit* script developed by Céline Lichtensteiger [159] in order to extract the thickness and the c-axis values of the thin films.

Rocking curve For this measurement the length of the scattering vector is kept constant while the incident angle is changed (ω scan). It is equivalent to tilting the sample as schematically represented in Fig. 3.14a. For a perfect

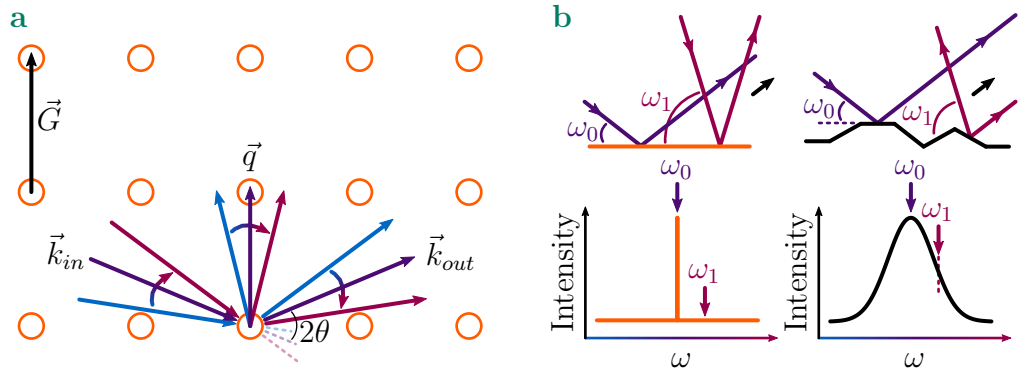

Figure 3.14: Working principle of a rocking curve scan. **a** Reciprocal space representation of the evolution of $\vec{q}$ during the scan, illustrating the fact that only for $\vec{q} = \vec{G}_{hkl}$ the measured intensity is maximal. In **b** is shown a comparison between a perfect sample (orange, left) and a textured one (black, right). The granular sample leads to a broadening of the peak because Eq. 3.6 is satisfied for various ω. The small black arrow represents the detector direction and the ones with the colour gradient the increase of ω during the scan.

crystal a narrow peak is expected around ω_0 such that $\vec{q} = \vec{G}_{hkl}$ as illustrated in the left panel in Fig. 3.14b. Indeed, when $\omega \neq \omega_0$ (e.g. ω_1) the diffracted wave is not pointing towards the detector (represented by the small black arrow). For a granular sample (see Fig. 3.14b, right panel) different incident angles can lead to a correct diffraction condition. Such effect leads to a broadening of the peak and its full width at half maximum (FWHM) reflects the distribution of the different orientations of the selected planes.

All the X-ray diffraction measurements presented in this thesis have been performed in-house with a high-resolution four-circle *PANalytical X'Pert Pro* system. A Cu source is used in order to produce the X-ray beam and a monochromator selects the Cu-$K\alpha_1$ radiation (λ=1.5406 Å).

3.2.3 Electrical transport

Electrical transport measurements are used to shed light on the electronic properties of a compound; a basic description is given in this section.

When electric charges move in a material, an electric field ($\vec{E}$) is produced given by Ohm's relation:

$$\vec{E} = \overline{\rho}\vec{J} \tag{3.8}$$

with $\vec{J}$ the current density and $\overline{\rho}$ the resistivity tensor; the $\overline{\rho}$ tensor elements depend on the material anisotropy. For an electrical current along the"x" direction (J_x) the relation becomes $E_x = \rho_{xx} J_x$. The electric field E_x is linked to the potential drop (V_{xx}) measured between two electrodes separated by a distance L as $E_x = \frac{V_{xx}}{L}$. Knowing the geometry of the conducting channel (width W and thickness t, see Fig. 3.15a), it is possible to calculate the current density $J_x = \frac{I_x}{W \cdot t}$ and estimate the resistivity ρ_{xx}; the longitudinal resistance also reflects the path geometry: $R_{xx} = \frac{\rho_{xx} L}{W \cdot t}$.

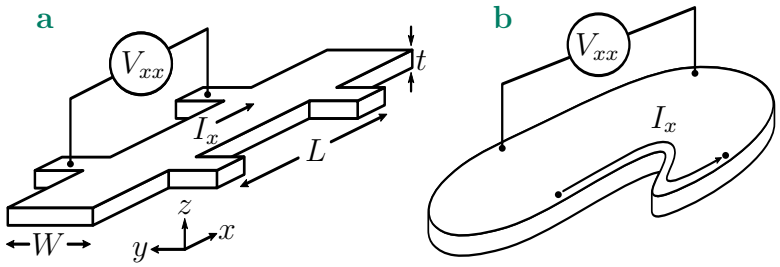

Figure 3.15: Different geometries for electrical transport measurements. **a** A Hall bar geometry with a length L, a width W and a thickness t. **b** A sample with an arbitrary shape illustrating the van der Pauw geometry.

Unless otherwise specified, all the resistance measurements are performed using a four-terminal sensing to get rid of the contacts and wires resistances. The measurement can be performed in a well-defined geometry, as illustrated in Fig. 3.15a for a Hall bar, or by placing the four contacts at the edges of the sample; this is called the van der Pauw geometry and is suitable for an arbitrary sample shape (see Fig. 3.15b). Most of the transport measurements reported in this manuscript have been done using the latter, and more details concerning this method are given in Appendix C.

Electrical transport measurements can be performed under various conditions: it is possible to vary the sample temperature (T), apply a magnetic field (B), change the current (I). The dependence of the resistivity on these quantities yields information on the electronic state of a system. For instance, recording the resistance (or resistivity) versus temperature allows one to discriminate samples with a metallic behaviour ($\frac{\partial R}{\partial T} > 0$), an insulating/semiconducting behaviours ($\frac{\partial R}{\partial T} < 0$) and a superconducting behaviour, characterised by a zero-resistance state below a critical temperature (T_c).

For the electric transport measurements two systems are used:

1. A home-made system, called "Fast-RT", allowing the measurement of the resistance as a function of the temperature between room temperature and 4 K. The sample is mounted onto a rod which is slowly dipped into a standard helium Dewar. Consequently, the temperature is not precisely controlled; the warming and cooling rates, however, can be adjusted by changing the moving speed of the rod inside the Dewar.
2. A Cryofree TeslatronPT cryostat from *Oxford Instruments*, where the temperature can be stabilised between 300 K and 1.5 K within ∼1% of the setpoint. A superconducting solenoid can produce a magnetic field of up to 12 T during the measurements.

3.3 X-ray spectroscopic measurements

3.3.1 X-ray absorption spectroscopy (XAS)

X-ray absorption spectroscopy is an experimental technique that probes the electronic structure as well as the local environment of the atoms in a compound. It relies on the absorption of an X-ray beam by matter: it is element-selective due to the energy dependence of the absorption coefficient. For this reason, one usually uses synchrotron radiation to scan the beam energy.

Considering a slab of thickness t, the transmitted intensity (I_T) of an X-ray beam is given by the Beer–Lambert law:

$$I_T(t) = I_0 e^{-\mu(E)t} \tag{3.9}$$

with $\mu(E)$ the energy dependent X-ray absorption coefficient and I_0 the incoming intensity. For a large energy range the absorption coefficient decreases smoothly with energy, as shown in Fig. 3.16a (orange part of the curve). However, an abrupt increase of the absorption coefficient is observed when the photon energy is equal to or higher than the binding energy of a core electron in an atom [160]. At this energy edge, the core electron is excited to an unoccupied state (Fig. 3.17a). In the energy range where such process happens, the spectra are analysed for their X-ray absorption near-edge structure (XANES), see Fig. 3.16b. The transitions between different energy levels induced by the electromagnetic field are governed by selection rules: for example $\Delta l = \pm 1$ (with l the angular momentum) and consequently a $1s$ electron will be excited to the lowest empty p-state [162]. This gives rise to characteristic energy spectra for each element in a compound, allowing one to probe the electronic states of the different cations and anions separately [163]. The edges are labelled with a letter (K, L, M) and an index such as L_1, L_2 and L_3 that indicates from which shell/subshell the electron originates (K-edge for a $1s$ electron, L_1-edge for a $2s$ electron and $L_{2,3}$-edges respectively for a $2p_{1/2}$ or a $2p_{3/2}$ electron).

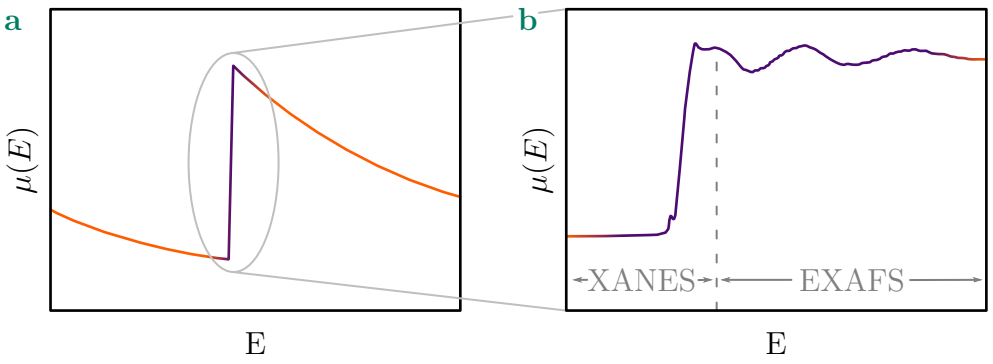

Figure 3.16: Absorption coefficient μ as a function of the incoming photon energy E in a XAS experiment. **a** Schematic graph of the absorption for a large energy range. It illustrates the smooth decay (orange) as well as the abrupt increase (purple) of $\mu(E)$ when a photon is absorbed from an atom (adapted from [160]). **b** Zoom on the absorption edge shown in **a** where the X-ray absorption near-edge structure (XANES) and extended X-ray absorption fine structure (EXAFS) ranges are indicated (adapted from [161]).

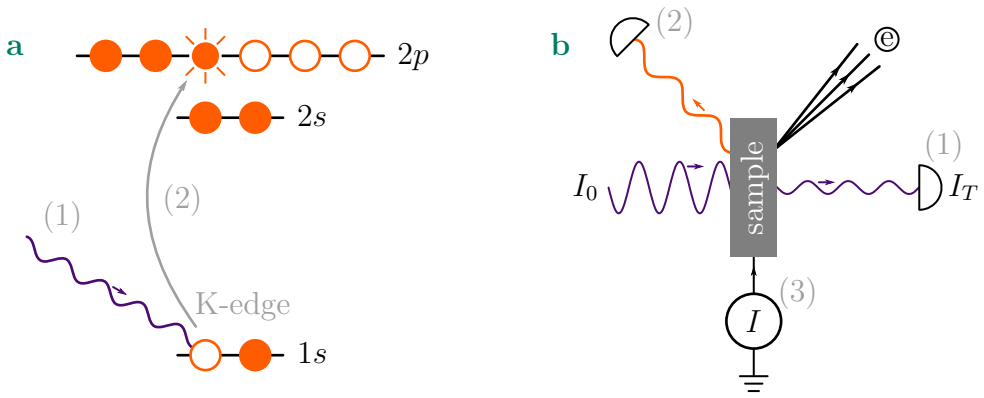

Figure 3.17: X-ray absorption spectroscopy technique. **a** The absorption process of an incoming photon (1), that excites an electron to a higher energy level (2) and promotes the absorber to an excited state. **b** Measurement modes in a XAS experiment: the direct transmission mode (1), the fluorescence mode (2) and the electron yield mode (3) described in the text (adapted from [160]).

For higher incoming photon energies, the core electrons are excited to the continuum (ionisation of the absorbing atom) and $\mu(E)$ oscillates with the energy: this energy region is investigated by extended X-ray absorption fine structure (EXAFS) spectroscopy, see Fig. 3.16b. These oscillations arise from the interference of the photoelectrons and provide structural information on the sample [160]. In the present work, EXAFS spectra were not studied, thus with XAS we will refer to XANES measurements in the following.

Measuring directly the transmitted intensity using soft X-rays (below 1 keV)

is often impossible. Indeed, the absorption coefficient being of the order of μm^{-1} in that energy range, the transmitted intensity vanishes for thin films deposited on a substrate. However, it is possible to measure the absorption coefficient indirectly, thanks to the fact that the absorbing atom is set in an excited state with a core hole, as shown in Fig. 3.17a. Such a configuration is not stable and two decay processes are possible to recover the ground state [160]:

1. an electron from a higher energy core-level fills the deeper core hole and ejects an X-ray of well-defined energy (fluorescence). Total fluorescent yield (TFY) counts the number of emitted photons from the sample, as represented in Fig. 3.17b (2).
2. an electron drops from a higher energy level and fills the core-hole and a second electron (an Auger electron) is excited to the continuum and eventually to free space. In the total electron yield (TEY), the number of electrons required to neutralise the Auger loss is counted, as shown in Fig. 3.17b (3).

The absorption coefficient depends on the filling and position of the energy levels, which gives information about the empty states of the atom under considerations; XAS can also provide information concerning the valence of the atoms, for example.

Before closing this section concerning the XAS technique it can be briefly mentioned that the use of polarised X-ray introduces additional selection rules, allowing one to selectively excite electrons in orbitals with different symmetries [163].

3.3.2 X-ray photoemission spectroscopy (XPS)

X-ray photoemission spectroscopy is a surface sensitive technique which probes the chemical composition of a solid as well as the electronic configuration of the different atoms. The working principle relies on the photoelectric effect: it is a photon-in electron-out (the photoelectron) experiment, with a similar physical concept as XAS (Section 3.3.1).

An X-ray beam illuminates a solid and if the energy of the photons ($h\nu$) is sufficient to overcome the binding energy (BE) of the electrons and the work function (ϕ) of the material, electrons are ejected (the photoelectrons) with a kinetic energy E_k [164–166], according to the following equation:

$$|\mathrm{BE}| = h\nu - E_k - \phi. \tag{3.10}$$

This process is schematically represented in Fig. 3.18. This makes XPS a technique which is sensitive to the occupied states of a solid as opposed to XAS which provides information about the unoccupied states.

An electron spectrometer counts the number of photoelectrons (N_{pe}) as a function of their kinetic energy. The measured spectrum $N_{pe}(E_k)$ consists of a series of peaks at energies that are characteristic of the orbital levels

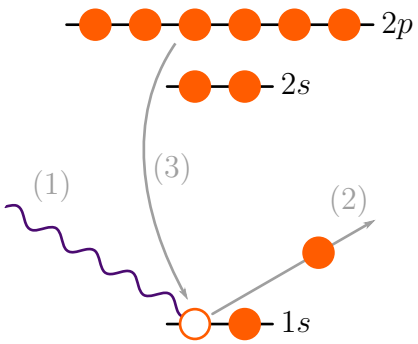

Figure 3.18: Schematic representation of the different steps in a XPS experiment. An incoming photon (1) with energy $h\nu$ can eject a photoelectron (2) from a core level state of an atom; note that the same notation as for XAS is used to label the edges. The excited atom can relax through the decay of an electron from a higher energy level (3) to the core level; such process can also lead to the emission of an Auger electron.

of the atoms in the compound. Consequently, XPS can be used to identify the elemental composition of a solid by identifying these characteristic peaks. Furthermore, the peak area is proportional to the element concentration in the solid [167], such that, from a careful integration of the peak area, the sample composition can be quantitatively determined.

The mean free path of the photoelectrons in a solid is relatively short (a few tens of ångströms to a few nanometres, depending on the material and the kinetic energy of the electrons), therefore only the electrons from the surface region can escape from the solid. Moreover, the emission probability decays exponentially as a function of the sample depth. Thus, the technique is strongly surface sensitive, and the probing depth can be controlled by changing the photon energy using synchrotron radiation and/or the take-off angle (the angle between the sample surface and the spectrometer entrance), thereby increasing or decreasing the contribution from the surface layer.

The binding energy of the core level electrons depends on the valence and the environment of the atom in the lattice. Thus, by observing the relative shifts of the core level peaks in the spectra (so called chemical shifts) we can obtain information about the oxidation state of the atom. The analysis of the chemical shift is however complicated by the screening effects of the final state. In fact, when a photoelectron is ejected from an atom, the remaining core hole will be screened by other charges in the system. The screening mechanism can alter the kinetic energy of the photoelectron, complicating the interpretation of the peak energies and lineshapes. Consequently, assigning a precise oxidation state for a specific atom may be non-trivial.

XPS is performed in an ultra-high vacuum environment to maximise the number of electrons that reach the spectrometer and to preserve the cleanliness of the surfaces.

Chapter 4

Study of the $SrTiO_3/CaCuO_2$ system

4.1 Controlling the copper-apical-oxygen distance in $SrTiO_3/CaCuO_2$

Considering the $SrTiO_3/CaCuO_2$ bilayer system, presented in depth in Section 2.3, one recalls that superconductivity is confined within a few unit cells of the $CaCuO_2$ layer at its interface with $SrTiO_3$. This is a consequence of the single CaO_x plane, providing the necessary apical oxygen for the underneath CuO_2 plane in order to dope the system. As sketched in Fig. 4.1 the infinite-layer film contains a unique apical oxygen plane through the whole structure. The oxygen atoms being negatively charged (O^{2-}), it can be envisaged to displace them using an electric field, an approach that could provide a unique way to control the copper-apical-oxygen distance.

An electric field (E) applied across a dielectric can generate a polarisation (P) through different microscopic mechanisms. For example, if dipoles are already present in the system, they can align with the external electric field. In a crystalline solid, like $SrTiO_3$, such dipoles do not exist a priori, but are created by the application of the electric field, through the displacement of the atoms and/or of the electronic clouds. This can be used to estimate the displacement of the apical oxygen upon the application of an external electric field in the $SrTiO_3/CaCuO_2$ bilayer, as described below.

The polarisation is given by the dipole moment (p) per unit volume (V): $P = p/V$ and $p = Q \cdot d$, with Q the electric charge and d the size of the dipole. For a linear dielectric the polarisation is given by $P = \epsilon_0 \chi_e E$ with ϵ_0 the electric permittivity of free space and χ_e the electric susceptibility which is linked to the relative permittivity (ϵ_r) by $\chi_e = \epsilon_r - 1$ [168].

The electric field that can be applied on $SrTiO_3$ is limited by its breakdown electric field, reported to be of the order of 40 MV/m [169, 170]. This conse-

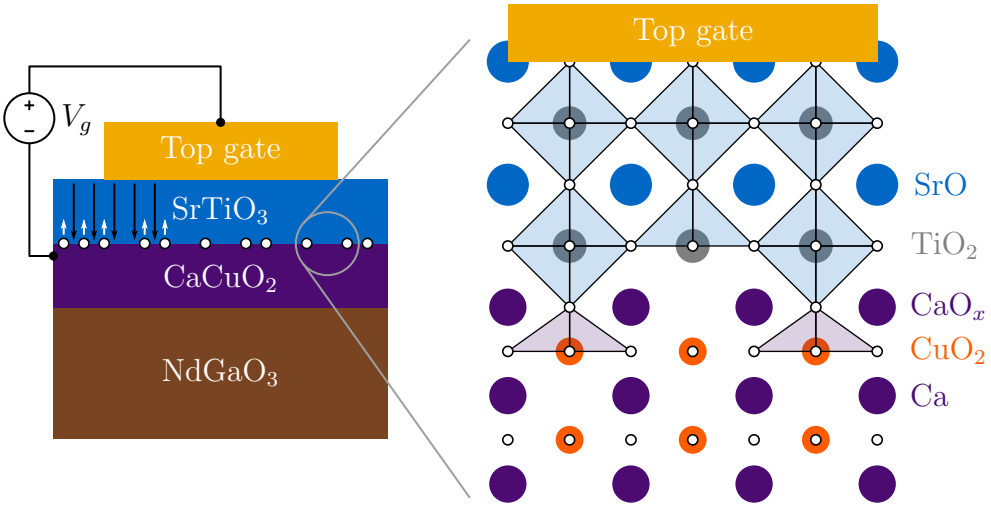

Figure 4.1: Sketch of the top gating experiment in a $SrTiO_3/CaCuO_2$ bilayer. **Left** Macroscopic structure showing the gate voltage and its effect on the single apical oxygen plane. Electric field (black arrows) and the associated displacement of the apical oxygen (white arrows) are illustrated. **Right** Microscopic structure at the interface. The presence of the apical oxygen in the CaO_x plane is emphasised by the light purple/blue (half-)octahedrons.

quently limits the maximal polarisation that can be achieved in $SrTiO_3$: using the linear approximation and $\epsilon_r = 1000$ one estimates that $P \sim 35\ \mu C/cm^2$. In reality $SrTiO_3$ is not a linear dielectric and its relative permittivity is strongly electric field and temperature dependent, leading to a more complicated behaviour. Measurements on $SrTiO_3$ thin films have shown that the maximal polarisation reachable experimentally is of the order of 10 $\mu C/cm^2$ [170], a value that can be used to estimate the atomic displacement of the apical oxygen under the application of an electric field.

Considering a charge $Q = 2e$ for the electric dipole formed inside $SrTiO_3$ (cubic, $a = 3.905$ Å), the distance d of the dipole can be calculated from the polarization: $d = \frac{p}{Q} = \frac{PV}{Q} \approx 0.2$ Å.

This estimation shows that atomic displacements are typically of the order of a few tenths of an ångström. Following the theoretical calculations of [92] (Fig. 2.4c, d) and the empirical observation of Fig. 2.3, a displacement of 0.4 Å leads to a change in T_c of almost 60 K. Such a dramatic effect on T_c can be directly detected by transport measurements and even if only a fraction of such displacement can be achieved, one should be able to observe an effect on the critical temperature.

In order to apply an electric field to displace the oxygen atoms at the interface, we envisage to use a top-gate geometry, as illustrated in Fig. 4.1, which takes advantage of the dielectric properties of $SrTiO_3$. The electric field will be confined between the top-gate electrode and the superconducting layer,

polarising the $SrTiO_3$ layer.

Along with the displacement of the apical oxygens, other effects will also occur when an electric field is applied to the top $SrTiO_3$ layer. For example, it will also act on the other atoms than the apical oxygen, and they shall be displaced too. The fact that the dielectric constant of $SrTiO_3$ depends strongly on the electric field [30] has also to be considered because this will change the dielectric environment of the superconducting layer (this is briefly treated later). Also important is the fact that, as discussed in Section 1.3 for the $LaAlO_3/SrTiO_3$ system, an electric field applied through a material with a high dielectric constant, as $SrTiO_3$, leads to a relevant change of the charge carrier density, allowing one to tune the doping and therefore affecting T_c (see Fig. 2.1b and Section 2.1.4).

As previously discussed, the ability to insert apical oxygen atoms at the $SrTiO_3/CaCuO_2$ interface and consequently to induce superconductivity seems to originate from the particular location of the last Ca plane which is in-between the infinite-layer and the perovskite structures (see Section 2.3). Replacing $SrTiO_3$ with another perovskite with a different dielectric constant leads also to a superconducting interface, as observed with $CaTiO_3$ [44]. This substitution allows the study of the effect of the dielectric environment on T_c. The use of a solid solution can also be envisaged, such as $(LaAlO_3)_x(SrTiO_3)_{1-x}$ which allows a continuous tuning with x from $SrTiO_3$ with its high and strongly temperature/electric field dependent dielectric constant to $LaAlO_3$, with an almost temperature/field independent low electrical susceptibility.

Uniqueness of the $SrTiO_3/CaCuO_2$ bilayer for gating experiments
The electric field-effect in superconductors is not something new: already in 1960 studies of In and Sn thin films revealed that T_c can be tuned with an electric field [171]. In the cuprates, similarly, gating experiments have been reported: for example, thin films of $YBa_2Cu_3O_{7-x}$, $Bi_2Sr_2CaCu_2O_{8+x}$ and $NdBa_2Cu_3O_{7-\delta}$ were measured with an electric field applied using a back-gate [172–175] or using a ferroelectric layer instead of the gate electrode [176–178]. Changes in the critical temperature were observed (see Fig. 4.2) and were in most cases attributed to a change of the charge carrier density, and thus to a doping effect. In YBCO, the possible rearrangement of the oxygen atoms in the Cu-O chains was also envisaged, as a consequence of the electric field [180, 181], although, there is no consensus on this effect [174]. More recently, the strong electric field of a mid-infrared optical pulse, polarised along the c-axis of YBCO, has been used to move the apical oxygen through the excitation of a specific phonon mode associated with $d_{\text{Cu-O}}^{\text{apical}}$ [182].

In all these studies the apical oxygen is potentially displaced because of the electric field. However, it is important to notice that for all the cuprates the structure is symmetric along the c-axis implying the existence of two apical oxygen atoms, one above the CuO_2 block and the other one below (see for

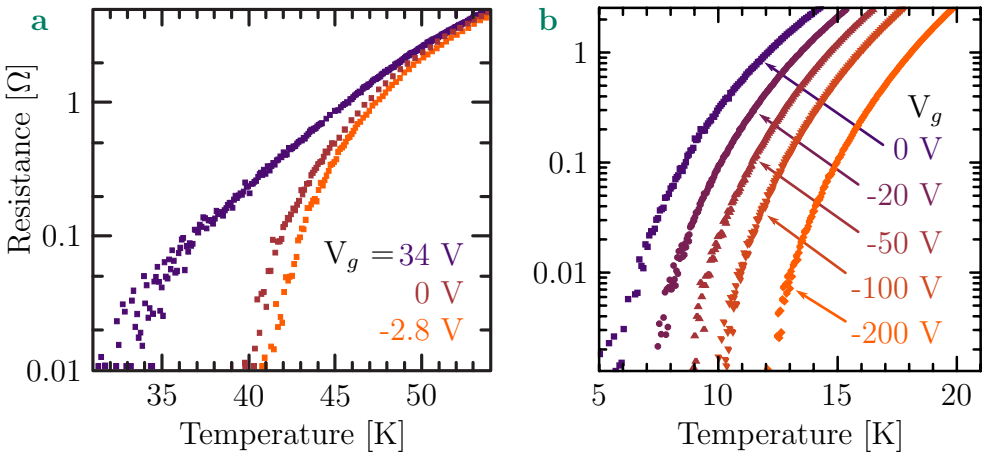

Figure 4.2: Gating experiment in HTS cuprates showing a change of T_c upon the application of a back-gate voltage. **a** Resistance as a function of temperature of a $YBa_2Cu_3O_{7-\delta}$ thin film for different gate voltages applied through a 300 nm thick $Ba_{0.15}Sr_{0.85}TiO_3$ gate insulator. Adapted from [6] and data from [179]. **b** Similar measurements as shown in **a** for a $NdBa_2Cu_3O_{7-\delta}$ thin film; the electric field was applied through a $SrTiO_3$ thin substrate. Adapted from [175]. In both cases a negative gate voltage corresponds to hole doping and an increase of T_c is observed.

example Fig. 2.5). If the electric field can displace the oxygen atoms, then one apical oxygen atom is brought further while the other is approached to the CuO_2 block, therefore compensating each other, as they all move in the same direction.

The $SrTiO_3/CaCuO_2$ bilayer has a single apical oxygen plane, hence the structure is not symmetric. Moreover, as doping is confined at the single interface between $SrTiO_3$ and $CaCuO_2$, complications originating from the multilayer effect are avoided. All these considerations render the $SrTiO_3/CaCuO_2$ interface a unique system to study the effect of $d^{\text{apical}}_{\text{Cu-O}}$ on T_c.

4.2 Growth of the $CaCuO_2/SrTiO_3$ bilayer

The study of the $SrTiO_3/CaCuO_2$ system as well as the realisation of the experiment presented in Section 1.4 and in greater details in Section 4.1, concerning the displacement of the apical oxygen in cuprates, requires to have superconducting $SrTiO_3/CaCuO_2$ samples. The first step toward this achievement is naturally the growth of these heterostructures. Infinite-layer cuprates, particularly $CaCuO_2$ and $SrCuO_2$ were not compounds usually grown in our laboratory, specifically using pulsed laser deposition. In this chapter, the results concerning the growth optimisation of $SrTiO_3/CaCuO_2$ bilayers by PLD are presented.

$CaCuO_2$ is known to be metastable in its bulk form (Section 2.2) [183]: epitaxy however has been shown to be particularly useful to stabilise the infinite-layer structure. The choice of the correct substrate for epitaxy aims at minimising the mismatch with the in-plane lattice parameter of the film. As reported in [43], the $SrTiO_3/CaCuO_2$ heterostructure grows coherently on a $NdGaO_3(110)$ substrate as its in-plane lattice parameters are in-between the ones of $SrTiO_3$ and $CaCuO_2$ (Table 2.1). Ideally, the substrate should be NdO terminated in order to have the correct stacking order at the interface (CuO_2-Ca-TiO_2-SrO), for superconductivity to emerge. In our case this is achieved through the annealing of the substrates, prior to the growth, for 10-15 hours at 1150°C in an oxygen flow, using a tubular furnace. Thanks to the high volatility of Ga, this thermal treatment leads to a crystal terminated with only NdO planes, commonly called single terminated substrate [184–186]. The single termination is evidenced by the step-and-terrace surface morphology observed with atomic force microscopy.

4.2.1 Growth in pure oxygen – optimisation of deposition parameters

The first heterostructures were grown in pure oxygen to avoid any complication coming from the use of ozone. In a first attempt, we tried to reproduce the growth conditions reported in [43, 44] as much as possible. We started growing a $CaCuO_2$ thin film at a substrate temperature of 600°C in 1 mbar of pure oxygen. A target-to-substrate distance of around 3 cm is used, which is the smallest distance for our system in order to avoid touching the sample holder with the excimer laser beam. The laser fluence at the target surface is set to approximately 1.2 J/cm^2, the uncertainty coming from the exact determination of the beam spot size. Using these conditions, $CaCuO_2$ thin films show poor crystalline quality, revealed by the low intensity of the $00l$ Bragg peaks in $\theta - 2\theta$ scans and the absence of finite size oscillations (see for example the orange curve in Fig. 4.3a). Thinking that $CaCuO_2$ samples can be extremely sensitive to air and humidity, we decided to cap these layers with $SrTiO_3$ in order to protect them.

$SrTiO_3/CaCuO_2$ bilayers were grown using different temperatures, pressures and fluences in order to obtain the highest crystalline quality. The first observation is that reducing the oxygen pressure to 0.5 mbar results in more intense diffraction peaks (not shown here), so the pressure was reduced to this value. In Fig. 4.3a an extended $\theta - 2\theta$ scan between 20° and 60° of a thin film grown at 700°C is shown, revealing the 001 and 002 diffraction peaks[1]. The zoom in the 22°-30° range shows the dependence of the 001 reflection on the

[1] $NdGaO_3$ has an orthorhombic structure, the out-of-plane direction for the substrate cut used in our experiments is the $[110]_o$ which corresponds, in the pseudo-cubic notation, to the $[001]_{pc}$.

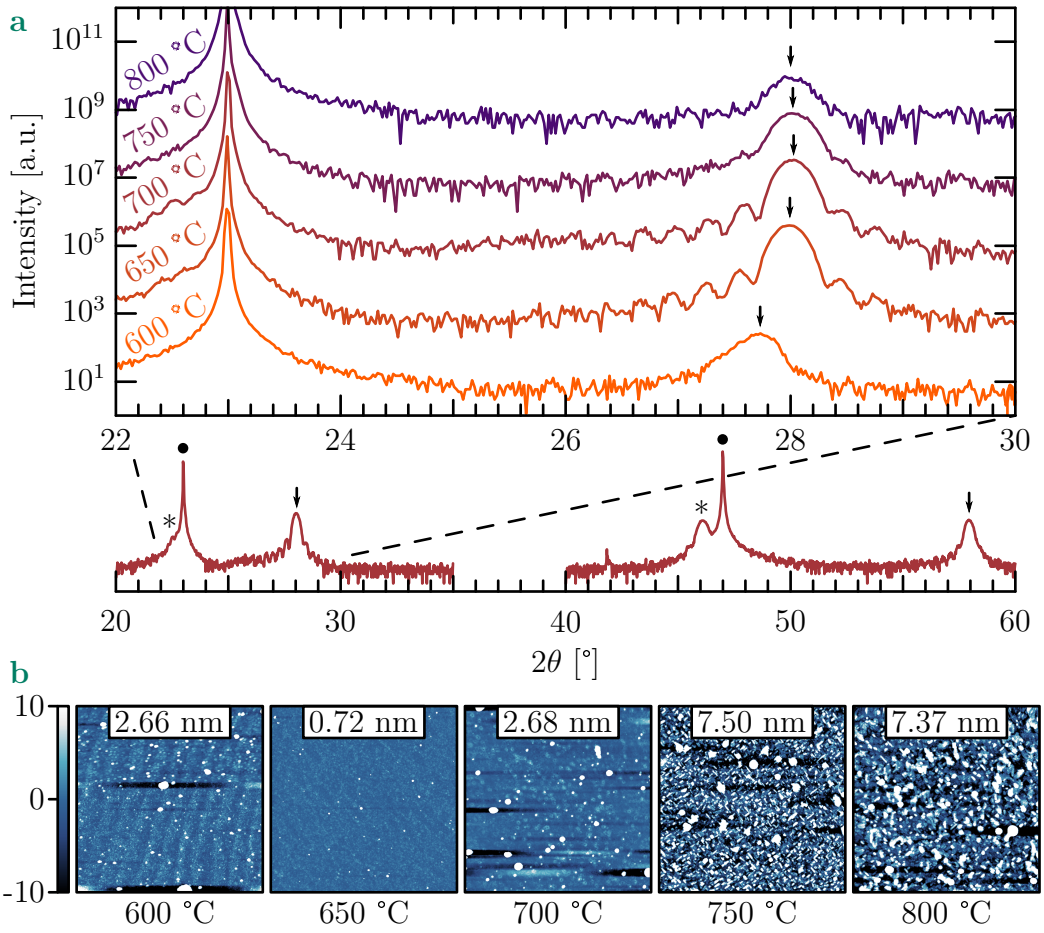

Figure 4.3: Dependence of the crystalline quality for the $SrTiO_3/CaCuO_2$ system upon the growth temperature. **a** $\theta - 2\theta$ patterns for temperatures ranging from 600°C to 800°C. The bottom curve shows a large scan along the [00L] truncation rod for the 700°C grown sample. The diffraction peaks are labelled with dots for the $NdGaO_3$ substrate, arrows for $CaCuO_2$ and asterisks for $SrTiO_3$. The diffraction peaks associated to the (001) planes are shown for $20° < 2\theta < 35°$ and the ones linked to the (002) planes occur in the 40°-60° range. **b** AFM topography measurements showing the typical surface for each growth temperature. The corresponding mean roughness is indicated in the white rectangle. The scanned area is $10\mu m \times 10\mu m$ for all temperatures and the height colour scale on the left is in nanometres.

growth temperature, swept between 600°C and 800°C while keeping the other parameters constant. One notices that increasing the growth temperature from 600°C to 650°C and 700°C improves the crystalline quality of the thin films; the emergence of finite size oscillations indicates the structural coherence of the layers and a well defined film thickness. Based on Section 3.1, a higher growth temperature increases the diffusion length of the adatoms and this tends to reduce the 3D growth mode. The sample surface is also smoother, as evidenced

by the surface roughness decreasing from 2.7 nm at 600°C to 0.7 nm at 650°C (see Fig. 4.3b). Raising further the temperature, the roughness increases to 2.7 nm at 700°C and exceeds 7 nm for higher temperatures. For temperatures above 700°C, the crystalline quality decreases: the presence of large particles on the surface suggests the formation of secondary phases. The growth temperature of 700°C was chosen to be the optimal one as the $CaCuO_2$ 002 peak shows finite-size oscillation unlike the one at 650°C (not shown); later we realised that 650°C is probably better due to the lower surface roughness (see Section 4.3)

The X-ray diffraction scans were analysed using the *InteractiveXRDFit* script [159] in order to extract the lattice parameters and the layer thickness. The analysis of the data for the sample grown at 700°C (see Fig. 4.4a) reveals

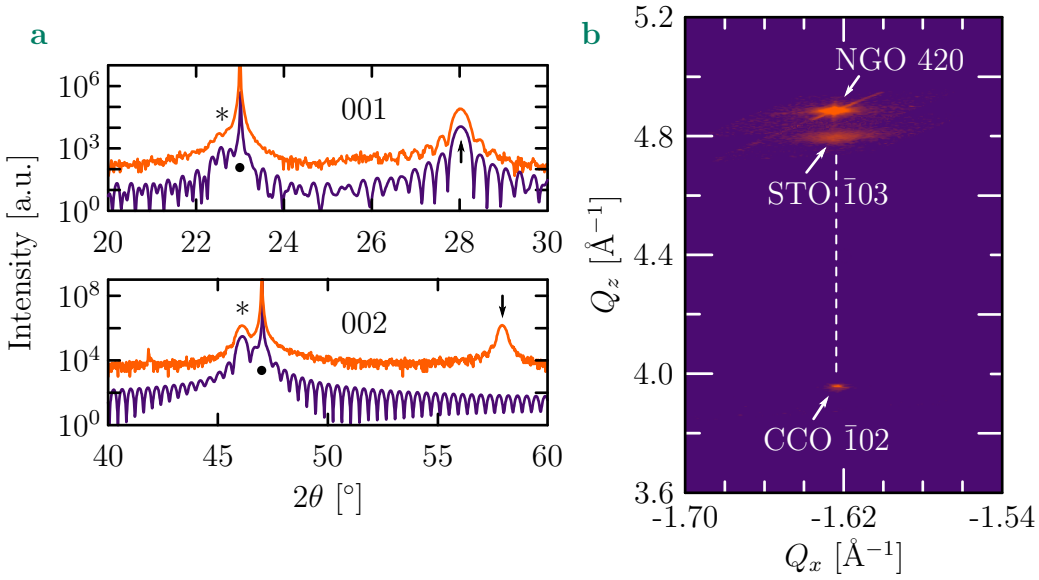

Figure 4.4: Structural analysis of the $SrTiO_3/CaCuO_2$ bilayer deposited in O_2 at 700°C. **a** Analysis of the $\theta - 2\theta$ scans, for the 001 and 002 Bragg reflections. The diffraction peaks are labelled with dots for $NdGaO_3$, arrows for $CaCuO_2$ and asterisks for $SrTiO_3$. The purple curves show the simulations for the $SrTiO_3/CaCuO_2$ bilayer in the top panel and only for $SrTiO_3$ in the bottom panel. **b** Reciprocal space map in the $Q_x - Q_z$ plane around the $\bar{1}03$ and $\bar{1}02$ reflections of the bilayer and the 420 $(\bar{1}03)_{pc}$ reflection of the substrate.

a $CaCuO_2$ thickness of 95 u.c. and a c-axis value of 3.181 Å (2θ=28.02°) in agreement with previous reports in literature [115, 183, 185, 187]. As it can be observed in Fig. 4.4b, the $SrTiO_3$ layer is found to be 61 u.c. thick with an out-of-plane lattice parameter of 3.937 Å (2θ=46.05°) in perfect agreement with strained $SrTiO_3$ which has a bulk lattice parameter of 3.905 Å and a Poisson ratio of 0.24 [188]. A further confirmation of the coherent growth of the heterostructure comes from reciprocal space map (RSM) measurements:

an example is shown in Fig. 4.4b. Both $CaCuO_2$ and $SrTiO_3$ have the same Q_x = -1.624 Å^{-1}, corresponding to the in-plane lattice parameter $a = \frac{2\pi n}{Q_x}$ = 3.87 Å, with $n = -1$ for the $\bar{1}02$ reflection. This value corresponds to the pseudo-cubic, in-plane lattice parameter of 110-oriented $NdGaO_3$.

As highly oxidising conditions are required to induce superconductivity in the $SrTiO_3/CaCuO_2$ system, the oxygen pressure was increased to 0.8 mbar and 1 mbar. At these higher pressures, the 001 $CaCuO_2$ diffraction peak becomes asymmetric and loses its finite size effect as shown in Fig. 4.5a. There-

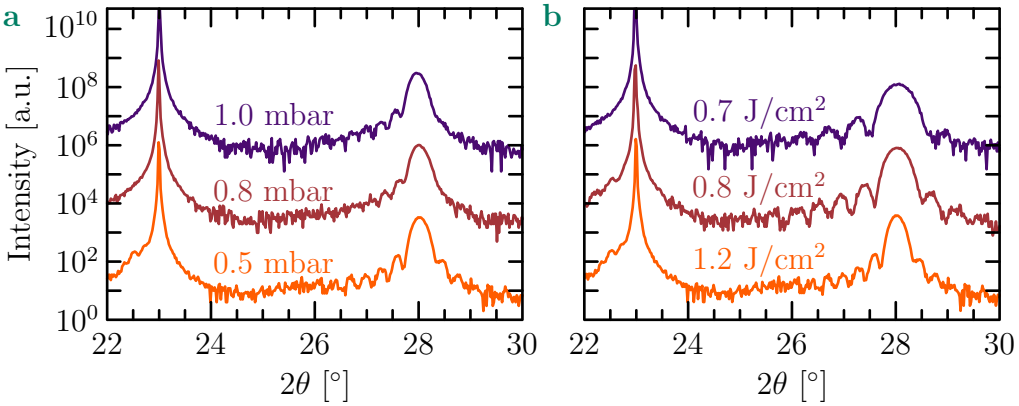

Figure 4.5: Dependence of the crystalline quality for the $SrTiO_3/CaCuO_2$ system for different growth pressures and laser fluences. **a** Influence of the pressure between 0.5 mbar and 1.0 mbar on the crystalline quality, evidencing the partial loss of the finite-size oscillations at higher pressures. **b** Effect of the laser fluence reduction, indicating that only the growth rate is changed.

fore, we kept the oxygen growth pressure at 0.5 mbar. The last parameter we modified has been the laser fluence: decreasing its value to 0.6 J/cm^2, by changing the laser energy, does not change the crystalline quality, it only reduces the deposition rate accordingly (see Fig. 4.5b).

In summary, our best films were obtained for a growth temperature of 700°C in an oxygen atmosphere of 0.5 mbar using an excimer laser fluence of 0.6-1.2 J/cm^2 with the target-to-substrate distance set at approximately 3 cm. If not specified, these values are considered as the growth parameters.

Before presenting the characterisation of films grown in ozone, we mention two experimental observations about the $CaCuO_2$ layer.

Background of dislocations Fig. 4.6a shows a rocking curve around the 001 $CaCuO_2$ diffraction peak: the scan can be seen as the superposition of two curves: the intense and narrow (FWHM = 0.07°) peak originates from the crystalline fraction of the $CaCuO_2$ film while the broad (FWHM = 0.35°) and less intense contribution can be associated with the dislocations present in the film, i.e. regions where the $CaCuO_2$ crystalline perfection is broken [189–

192]. Similar results have been reported in literature, indicating that this originates from distortions in $CaCuO_2$, close to the $NdGaO_3$ interface [130, 185], as illustrated in Fig. 4.6b. The exact nature of this interface has not been

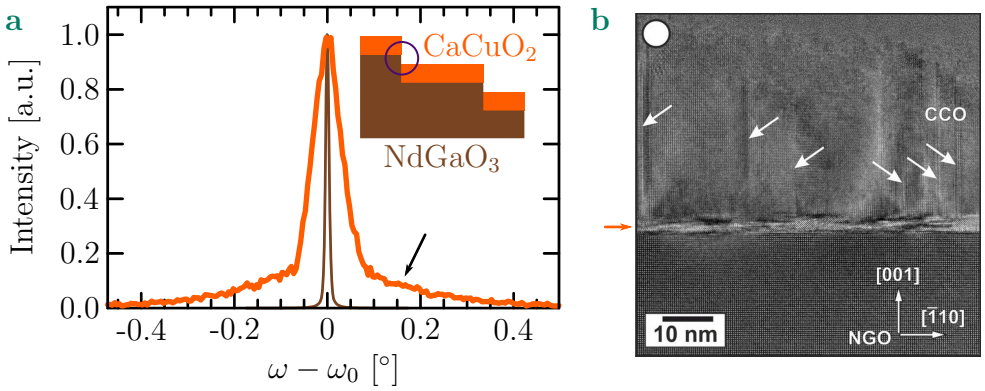

Figure 4.6: Dislocation background in $SrTiO_3/CaCuO_2$. **a** Rocking curve acquired around the $CaCuO_2$ 001 Bragg peak (orange curve), revealing the dislocation background (black arrow) in the $CaCuO_2$ layer. The brown curve shows the data around of the $NdGaO_3$ 220 substrate peak. The inset illustrates the mismatch between the c-axis values of $NdGaO_3$ and $CaCuO_2$. **b** STEM image of the interface between a $NdGaO_3$ substrate and a $CaCuO_2$ thin film (reprinted from [185]). The $CaCuO_2$ structure is distorted at the interface with $NdGaO_3$ (orange arrow) compatible with the rocking curve shown in **a**.

properly investigated but our results are compatible with these observations.

The presence of these distortions has been observed by different groups and using various growth conditions, implying that this is probably intrinsic to the system, and does not originate from particular growth conditions. At the $CaCuO_2/NdGaO_3$ interface there is a mismatch of vertical lattice parameters between the $NdGaO_3$ perovskite structure (c-axis of 3.86 Å) and the $CaCuO_2$ infinite-layer structure with a much smaller out-of-plane parameter (3.18 Å) as illustrated in the inset of Fig. 4.6a. At the edges of the terraces, the layer faces a step larger and incommensurate with its lattice structure. This could be one reason for this distorted interface to appear: the system needs a transition layer to adapt from one structure to the other; after this transition layer, the infinite-layer is much less distorted as seen in Fig. 4.6. Although the same mismatch is present at the $SrTiO_3/CaCuO_2$ interface, it does not seem to affect the emergence of superconductivity, if the $CaCuO_2$ layer is thick enough [130].

Stability of the infinite-layer phase As already mentioned, the samples prepared during the optimisation process were $SrTiO_3/CaCuO_2$ bilayers. $SrTiO_3$ was used as a protective layer because the stability of the infinite-layer $CaCuO_2$ was not certain from the measurements done on single $CaCuO_2$ thin films. However, we realised later, with the optimised conditions that single

$CaCuO_2$ thin films are surprisingly stable in time. This can be observed in Fig. 4.7, where the same sample, a single $CaCuO_2$ thin film, has been measured right after its growth and more than one and a half years later. The

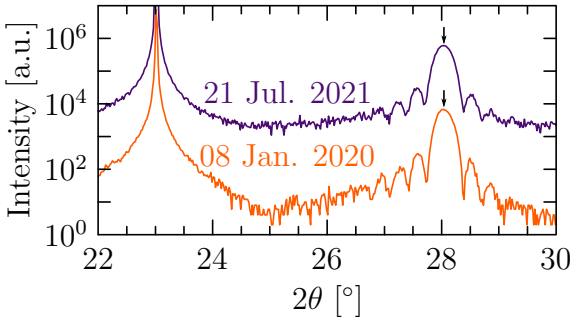

Figure 4.7: Phase stability in time of a single $CaCuO_2$ thin film. The $\theta - 2\theta$ scan shows the $CaCuO_2$ 001 Bragg peak (arrows), measured right after the sample growth (orange) and more than one year and half later (purple). The difference in background noise is due to the use of two different diffractometers.

two measurements indicate that the layer maintains the same stoichiometry (the $CaCuO_2$ 001 peak remains at the same position) and the same crystalline quality (identical finite size oscillations). The consequences of this result are that the $SrTiO_3$ capping layer is not required to protect the $CaCuO_2$ phase since this is stable enough on our time scale; thus, the optimisation of the growth parameters in a highly oxidising atmosphere can be pursued on single $CaCuO_2$ thin films.

4.2.2 Growth in highly-oxidising conditions

The introduction of apical oxygen atoms in the last Ca plane of the $SrTiO_3$/$CaCuO_2$ interface requires highly oxidising growth conditions. As discussed in Section 2.3.2, Di Castro and co-workers use a mixture of oxygen with 12% of ozone to obtain superconducting samples. In the work presented in this chapter, all the samples grown with ozone were deposited in a O_2/O_3 mixture containing 5% of ozone, a limitation due to our ozone generator.

As the $SrTiO_3$ layer is not necessary to preserve the $CaCuO_2$ phase stability, single $CaCuO_2$ films were grown, using the optimal growth conditions described in the previous section, and replacing O_2 by the O_2/O_3 mixture. The XRD pattern of a typical film is shown in Fig. 4.8a (purple curve), compared to a film grown in pure oxygen (orange curve). As it can be noticed the film quality is strongly dependent on the growth atmosphere. The addition of ozone to the growth atmosphere reduces the peak intensity and suppresses the finite size oscillations. Similarly, AFM measurements, shown in Fig. 4.8b, reveal that the surface mean roughness increases from 0.9 nm for O_2 films to 11.6 nm in presence of O_2/O_3. Based on the deposition rate of samples grown in O_2

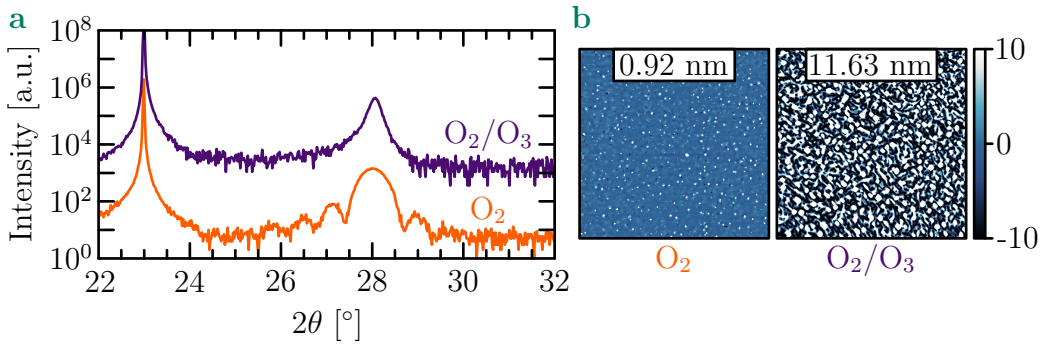

Figure 4.8: Comparison of structural quality of $CaCuO_2$ films deposited in O_2 and O_2/O_3. **a** $\theta-2\theta$ scans, around the 001 reflection, showing that the structural quality of $CaCuO_2$ strongly depends on the growth atmosphere. **b** AFM topography images showing the surface of the two samples shown in **a**. The mean roughness is indicated in the white rectangle. The scanned area is $10\mu m \times 10\mu m$ in both cases and the colour scale on the right is in nanometres.

(5.5 pulses/u.c.), the thickness of the O_2/O_3 sample is expected to be about 14.3 nm. Considering that the roughness is of the same order of magnitude as the total thickness, it is not surprising to lose the finite size oscillations. Additionally, the height distribution (not shown) of the topography is broader than 50 nm, indicating that the growth mode is completely different when ozone is used. However, it is quite impressive that the *c*-axis is still well defined, as a single and well defined peak is observed in the XRD pattern, which may suggest a 3D mode growth (see Section 3.1.1).

The use of different temperatures (600-800°C), pressures (0.1-1.0 mbar) and target-to-substrate distances (3-5 cm) during the growth does not lead to any clear improvement of the crystalline quality, neither reduction of the surface roughness. The deposition of a top $SrTiO_3$ layer does not help to improve the layer quality either.

As obtaining high quality thin films in O_2/O_3 was an issue and as all the samples were semi-conducting (see Section 4.3), a few attempts to introduce interfacial oxygen atoms by different means were tried:

- *In-situ* post-annealing in 0.1 bar of O_2 of a bilayer grown in O_2.
- *Ex-situ* post-annealing in 10 bar of O_2 of a bilayer grown in O_2.
- Use of the O_2/O_3 mixture only for the deposition of the interface region (last ten u.c. of $CaCuO_2$ and the first five u.c. of $SrTiO_3$).
- O_2/O_3 annealing of the $CaCuO_2$ film grown in O_2, before the deposition of $SrTiO_3$ in O_2.
- *In-situ* post-annealing in O_2/O_3 of a bilayer grown in O_2, using a similar pressure as for the deposition.
- The use of N_2O instead of O_2/O_3 as a highly oxidising atmosphere; we note that in this atmosphere we did not manage to grow $CaCuO_2$ at all.

None of these attempts led to a clear and reproducible improvement of the crystalline quality, nor of the electrical transport properties. Most of the samples were still semiconducting, and some were even completely insulating, with a resistance too high to be measured.

4.2.3 Importance of the delivery tube position

It was mentioned in Section 3.1.2 that the position of the gas delivery tube in the PLD growth chamber can be controlled using a wobble stick. All the results presented up to this point were obtained on samples grown before the installation of this wobble stick. For such samples, the delivery tube was positioned as illustrated in the scheme of Fig. 4.9, referred as (pos1). The

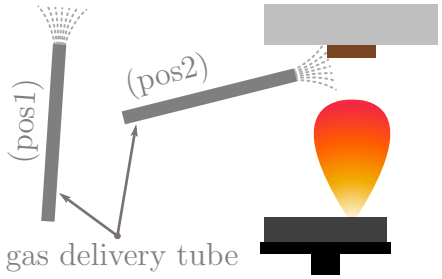

Figure 4.9: Positions of the oxygen and O_2/O_3 delivery tube inside the PLD growth chamber. In (pos1) the tube points away from the substrate and they are separated by a distance of the order of 10 cm, while in (pos2) the tube points directly to the substrate and the tube-to-substrate distance is approximately 1.5 cm.

tube outlet is placed relatively far from the substrate (∼10 cm) and points away from the substrate. As described in the previous section, in (pos1), the film quality is strongly dependent on the gas composition and the use of O_2/O_3 degrades the film quality. In (pos2) the distance between the tube outlet and the substrate is close to 1.5 cm and the tube points toward the substrate (see Fig. 4.9).

The effect of approaching the tube to the substrate, as in (pos2), is shown in Fig. 4.10: the crystalline quality of the layers is high for deposition both in O_2 and O_2/O_3, presenting intense Bragg peaks and finite-size oscillations. Moreover, the surface quality is similar in both atmospheres, with a mean roughness of the order of 1.5 nm as shown on the AFM topography in Fig. 4.10b. This corresponds to approximatively 3 u.c. of $CaCuO_2$ and is relatively small compared to the whole film thickness (∼45 u.c.). It is also interesting to notice that the surface morphology is quite different between the two growth atmospheres.

As seen from Fig. 4.8 and Fig. 4.10 the effect of the position of the delivery tube on the film quality is quite puzzling. We note that despite setting the same pressure in the chamber, the effective O_2/O_3 pressure felt by the plume

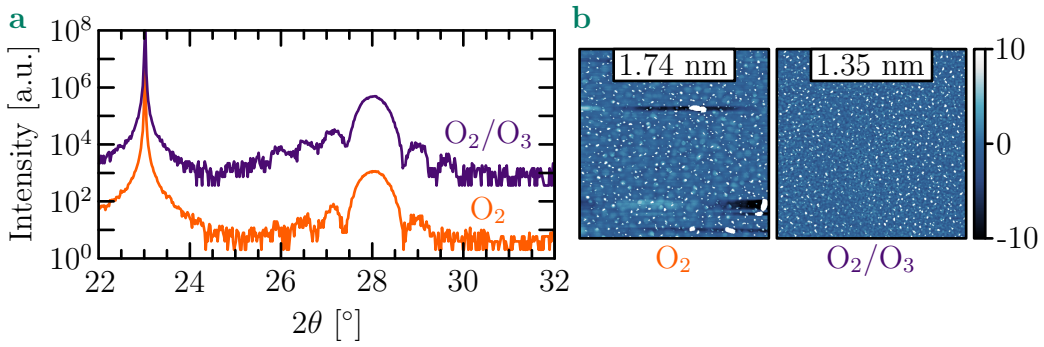

Figure 4.10: Growth quality of $CaCuO_2$ films deposited in O_2 and O_2/O_3 with the delivery tube close to the substrate (pos2). **a** $\theta - 2\theta$ scans, around the 001 reflection, showing that the structural quality of $CaCuO_2$ does not depend on the growth atmosphere. **b** AFM image showing the typical surface of the sample shown in **a**. The corresponding mean roughness is indicated in the white rectangle. The scanned area is $10\mu m \times 10\mu m$ in both cases and the colour scale is in nanometres.

and substrate may be strongly different for the two tube positions. Although we did not find many studies considering the dependence of film quality on the ozone delivery tube position, our result is in agreement with the few existing reports present in literature, where the authors mention that the ozone tube should point to the substrate [193–196] and eventually be close to it [193, 197] for both PLD and MBE.

In (pos2) the tube is much closer to the substrate which is warmed up during the growth, consequently the delivery tube outlet is probably heated by radiation. This would help to decompose the ozone and reduces its percentage in the O_2/O_3 mixture [151, 198, 199]. Even if ozone is produced, it would have a reduced and possibly negligible effect on the oxidising power during the deposition if the temperature of the tube is too high. Quantitatively estimating the role of this effect is difficult but it can be mentioned that for the same tube position with, admittedly, a lower substrate temperature, the deposition of $SrCuO_2$ in O_2 and O_2/O_3 leads reproducibly to different structures depending on the growth atmosphere (discussed in Chapters 5 and 6). This strongly suggests that the oxidising power is effectively higher when O_2/O_3 is used and that ozone is not completely decomposed by the delivery tube being warmed up.

An interesting experiment to shed light on the effect of the tube position would be to perform plasma spectroscopy of the plume [200, 201] for the different tube positions and oxidising atmospheres. Particularly interesting is the fact the alkaline-earth metals (Ca, Sr, Ba) are rapidly oxidised in highly oxidising atmosphere [201] and in our case following the formation of CaO_x depending on the tube position would be especially interesting.

Although the effect of the delivery tube position is still not understood, this result is an important achievement as it makes it possible to envisage the growth of high quality $SrTiO_3/CaCuO_2$ bilayers in O_2/O_3 and hopefully to get superconducting interfaces. Particularly encouraging is the reduction of the $CaCuO_2$ surface roughness; it is indeed difficult to imagine the emergence of superconductivity if the interface between $CaCuO_2$ and $SrTiO_3$ is very rough.

A bilayer grown in (pos2) using the O_2/O_3 mixture is shown in Fig. 4.11 as an example of the structural quality for such films. As it can be observed in

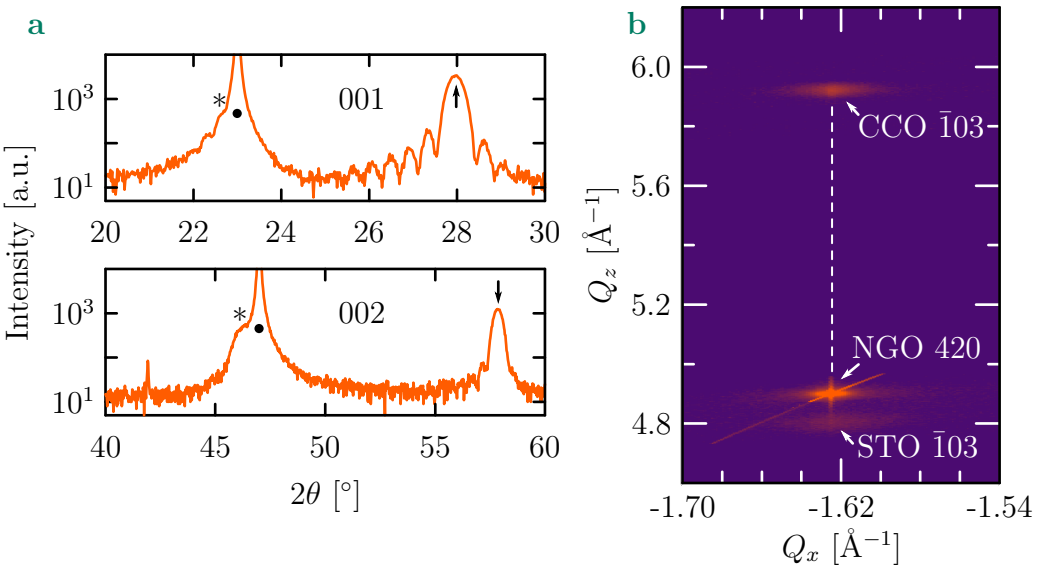

Figure 4.11: Structural properties of a $SrTiO_3/CaCuO_2$ bilayer deposited in O_2/O_3 at 650°C and with the delivery tube in (pos2). **a** $\theta - 2\theta$ for the 001 and 002 Bragg reflections, showing the $NdGaO_3$, $CaCuO_2$ and $SrTiO_3$ peaks denoted by the circles, arrows and asterisks respectively. **b** Reciprocal space map in the $Q_x - Q_z$ plane around the $\bar{1}03$ reflection of the bilayer and the 420 $(\bar{1}03)_{pc}$ reflection of the substrate.

panel **a**, the intense Bragg peaks and the presence of finite size oscillations for both $CaCuO_2$ and $SrTiO_3$ indicating the high crystallinity of this bilayer – the $SrTiO_3$ signal is more easily visible for the (002) plane as its lattice parameter is relatively close to the one of $NdGaO_3$. Fig. 4.11b shows an RSM around the $\bar{1}03$ reflection of the same film, demonstrating that our bilayers are completely strained to the $NdGaO_3$ substrate.

4.3 Electrical transport properties of the $SrTiO_3/CaCuO_2$ bilayer

The results presented up to this point concern the structural properties of the thin films. In this section the focus is on the electrical transport behaviour for the different growth conditions explored previously: O_2 and O_2/O_3 atmospheres, with the delivery tube in (pos1) and (pos2). Superconductivity in the $SrTiO_3/CaCuO_2$ system originates from an interfacial effect (see Section 2.3), emerging in $CaCuO_2$ at the interface with $SrTiO_3$ [44], consequently the results presented in this section are obtained on $SrTiO_3/CaCuO_2$ bilayers. The resistance measurements presented in this section are acquired using the van der Pauw geometry (Appendix C).

A summary of the typical resistivity curves as a function of temperature for the different growth conditions is shown in Fig. 4.12a. The resistivity ρ is estimated from the resistance R using the van der Pauw formula (Eq. C.4) and considering the thickness of the $CaCuO_2$ layer only. The figure shows that single $SrTiO_3$ thin films grown on $NdGaO_3$ are completely insulating while single $CaCuO_2$ thin films show a semi-conducting behaviour. The semi-conducting behaviour is revealed by plotting the data on an Arrhenius plot ($\ln(\rho)$ as a function of $1/T$, see Fig. 4.12b): the linear regime observed at high temperature can be fitted by thermally activated transport: $\rho(T) = A \exp\left(\frac{E_a}{k_B T}\right)$, with E_a the activation energy and k_B the Boltzmann constant. The activation energy for the different growth conditions (oxidising power and tube position) is shown in Fig. 4.13.

For samples deposited in pure oxygen with the delivery tube in (pos1) the resistivity shows a semi-conducting behaviour as a function of temperature (dotdashed orange curve) down to $\simeq$150 K with an activation energy of 30-40 meV. At lower temperatures, another transport mechanism, probably of hopping type, dominates the conduction. Such behaviour of the resistivity has already been observed for samples grown in O_2, as highly oxidising conditions are required to induce metallicity and eventually superconductivity in this system [43].

The introduction of 5% of ozone during the sample deposition increases the electric resistivity (dotdashed purple curve), an effect opposite of what is expected. However, as described in Section 4.2.2 the crystalline quality is reduced when O_2/O_3 is used in (pos1). The morphology of the corresponding AFM topography shown in Fig. 4.8b makes one think of disconnected islands with different heights. This could shed some light on the reason behind the resistivity increase when O_2/O_3 is used as well as on the large spread observed in Fig. 4.13 for the activation energy values, suggesting irreproducible growth conditions. In any case, these growth conditions are not suitable for the emergence of superconductivity, particularly considering the fact that the $CaCuO_2$

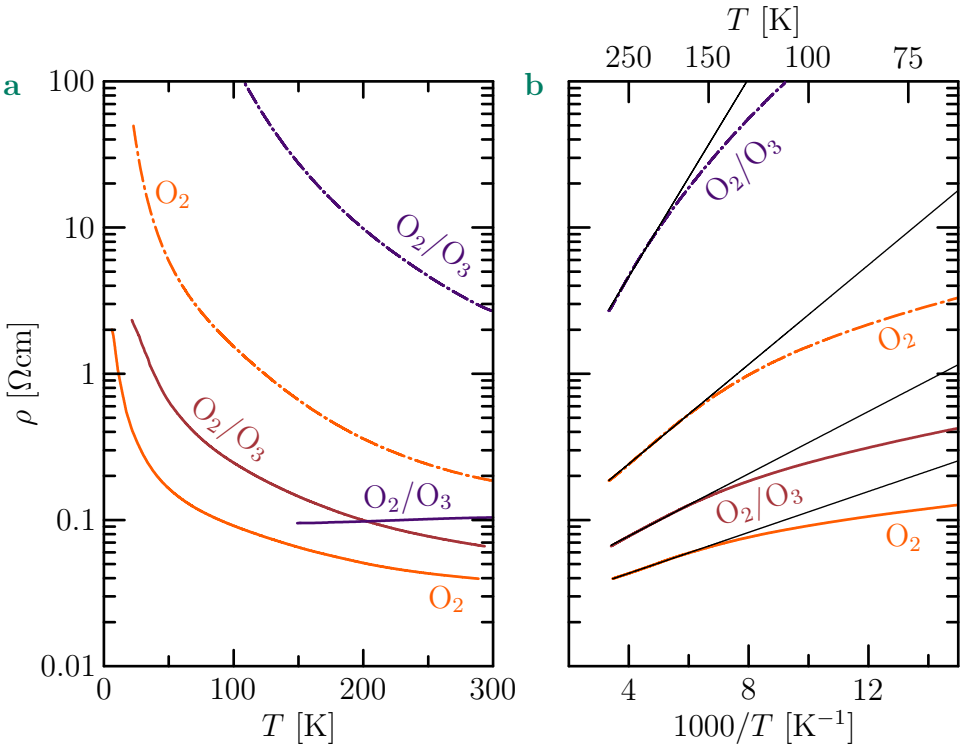

Figure 4.12: Transport properties of the $SrTiO_3/CaCuO_2$ system. **a** Typical resistivity curves for different oxidising power (orange for pure O_2 and purple for O_2/O_3) as well as different delivery tube positions (dotdashed for (pos1) and solid for (pos2)). As described later in the main text, the brown curve is typical for a sample deposited with the O_3 generator on, but without certainty about the actual ozone production. Note that the solid purple curve shows a metallic behaviour. **b** Same data as in **a**, for the insulating samples, shown on an Arrhenius plot. The black solid lines are fits at high temperature assuming a thermally activated transport.

has a high surface roughness which would not favour a high interface quality.

When the delivery tube is approached in (pos2) different transport behaviours of samples nominally grown in the same conditions are observed. This is evidenced by the large variation of the activation energies reported in Fig. 4.13, particularly pronounced for the samples deposited in O_2/O_3 (E_a between 5 meV and 55 meV), for which the value of the resistance at room temperature is observed to vary between 3 kΩ and 200 kΩ from one sample to another. The large variation of E_a using different oxidising conditions[2] (represented by the opened symbols in Fig. 4.13) suggests that the irreproducibility is related to the oxidising atmosphere.

However, we notice that some samples, in particular the ones grown at

[2]The oxidising conditions can be tuned by controlling the pressure, the rate of gas flow or by small changes of the delivery tube position.

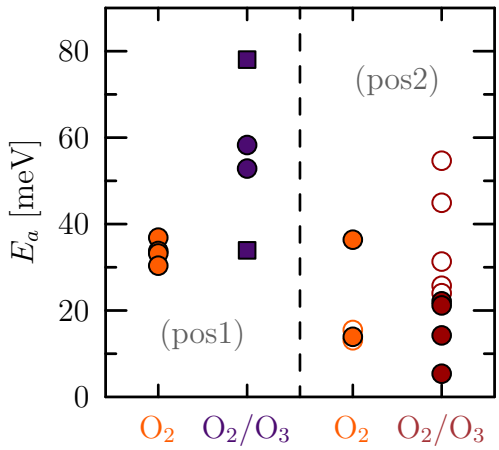

Figure 4.13: Activation energy (E_a) for various $SrTiO_3/CaCuO_2$ bilayers as a function of the oxidising power and the delivery tube position. The colour of the symbols corresponds to the oxidising condition as in Fig. 4.12 and the tube positions are separated in two panels – left for (pos1) and right for (pos2). The circles represent samples deposited nominally in the same growth conditions, while the open symbols emphasise the sample with different oxidising conditions (pressure, gas flow or small displacement of the delivery tube position) and the squares are for samples grown at temperature higher than 700°C.

lower temperature (650°C), show a metallic behaviour, pushing us to pursue our efforts, despite the difficulty obtaining reproducible films. Samples with a metallic behaviour were measured only above 150 K because of their high contact resistance (see Section 4.3.1). Despite the difficulty associated with measuring them at low temperature, this is an impressive improvement, compared to the films deposited with the delivery tube in (pos1) as in that case only insulating samples were obtained. This is an encouraging result indicating that it is possible to obtain superconducting $SrTiO_3/CaCuO_2$ bilayers.

It is worth mentioning that the room temperature resistance of a metallic film is typically about 10 kΩ which is still one order of magnitude higher than the resistance of reported superconducting structures with similar geometry as shown in Fig. 2.7. One possibility is that the oxygen content at the interface is insufficient in order to dope the system to obtain superconductivity. Indeed, the ozone generator used in the present study produces 5% of ozone, while superconductivity has been reported for a gas atmosphere composed of 12% of O_3 [43, 44].

Unfortunately, we started to have a technical issue with our ozone generator, while growing these bilayers: even if the generator was turned on, no ozone was produced and this was happening randomly. This may have occurred because there is no gauge to monitor the presence and the level of ozone in the deposition chamber. We realised this malfunction growing $SrCuO_2$ thin films which are strongly sensitive to the presence of ozone, as described in

Chapter 6. We do not know exactly when this problem happened, but it can question the validity of our results concerning the delivery tube position: the samples supposedly grown in ozone were potentially deposited in pure oxygen explaining the similar structural quality as the ones grown in pure oxygen. We believe that this is the reason behind the strong irreproducibility observed for the sample deposited in O_2/O_3 with the delivery tube in (pos2). However, the metallic behaviour measured for some samples grown with the delivery tube in (pos2) suggests that the tube position is an important parameter for high crystalline quality and conductive $SrTiO_3/CaCuO_2$ heterostructures.

One last point should be mentioned: the XRD measurements being sensitive to the "bulk" of the film show that the whole structure of the metallic film is very similar to the bilayers grown in pure oxygen. However, the transport properties are strongly different indicating that our observation is qualitatively in agreement with the picture of Di Castro and co-workers reporting interfacial conduction. Indeed, the insertion of apical oxygen in the last Ca planes would change the film structure only within 1-2 u.c. (as shown in Fig. 2.6) which is too small to be observed with laboratory X-ray diffraction measurements.

4.3.1 Contact resistance

Before concluding this chapter about the growth of the $SrTiO_3/CaCuO_2$ system, one can mention a general observation for all $SrTiO_3/CaCuO_2$ bilayers, independently of the growth conditions. Usually, the sample is contacted by bonding Ag/Si wires directly on the sample going through the whole bilayer and connecting $SrTiO_3$, $CaCuO_2$ and the interface at once. At room temperature the contact resistance is generally roughly around 50-100 kΩ and it rises up to few MΩ at low temperature, for highly restive samples it can even go above few tens of MΩ making them impossible to measure below a certain temperature.

Different attempts were made in order to reduce the contact resistance:

> deposition of top electrodes (Pt or Au) on the sample surface before the bonding

> small Ag-paste drops deposited before the thin film growth, contacted by direct bonding or by the use of Ag-paste using copper wires.

None of them led to a clear and reproducible improvement of the contact resistance.

In superconducting $SrTiO_3/CaCuO_2$ bilayers provided by D. Di Castro, we measured a contact resistance of the order of 10 kΩ with direct bonding, roughly independent of the temperature. From our experience it seems that the reduction of the contact resistance is concomitant with the reduction of the interface resistance.

4.3.2 Conclusion and outlook for the growths

We succeeded growing $SrTiO_3/CaCuO_2$ bilayers with a metallic behaviour, a result made possible by approaching the O_2/O_3 delivery tube to a few centimetres from the substrate. This result is quite encouraging in our pursuit of superconductivity in the $SrTiO_3/CaCuO_2$ bilayers, which would give us the opportunity to shed light on the role of the apical oxygen for the mechanism of the superconductivity in cuprates.

Our new O_3 generator delivers a O_2/O_3 mixture with an ozone content tunable up to 20% (see Section 3.1.2). This will allow us to study the effect of the ozone percentage on the interface resistivity, and potentially insert enough apical oxygen for observing superconductivity. We are currently working on the optimisation of the growth conditions to obtain high quality thin films with this new generator.

4.4 Technical developments for the gating experiment

The realisation of the experiment presented in Section 4.1 requires the ability to realise a device with a geometry as illustrated in Fig. 4.14. This configuration is necessary to have a well defined geometry for transport experiments, where the conducting channel is affected by the top gate.

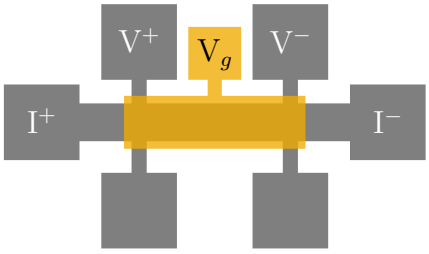

Figure 4.14: Sketch showing the field-effect device for the top gating experiment. In grey, the superconducting channel at the interface between $SrTiO_3$ and $CaCuO_2$, and in yellow the top-gate electrode.

The deposition of a top-gate electrode is usually not an issue: using a lift-off process, a metallic layer on photolithography defined region can be obtained on top of the sample (see Section 3.1.3). This was done for $LaAlO_3/SrTiO_3$ in order to study magneto-transport with both top and back-gate electrodes [32].

The first attempts were done depositing a gold layer onto a $SrTiO_3/CaCuO_2$ bilayer, the gate electrode area being defined by a photoresist. However, for $SrTiO_3/CaCuO_2$ bilayers, the photolithographic process is an issue for the $CaCuO_2$ thin film, in particular the immersion into the photoresist developer. In Fig. 4.15a the bottom curve shows a $\theta-2\theta$ X-ray scan of a bilayer, where the

infinite-layer $CaCuO_2$ peak as well as the one from $SrTiO_3$, the bump on the left of the substrate peak, can be identified. After sonication of the sample for

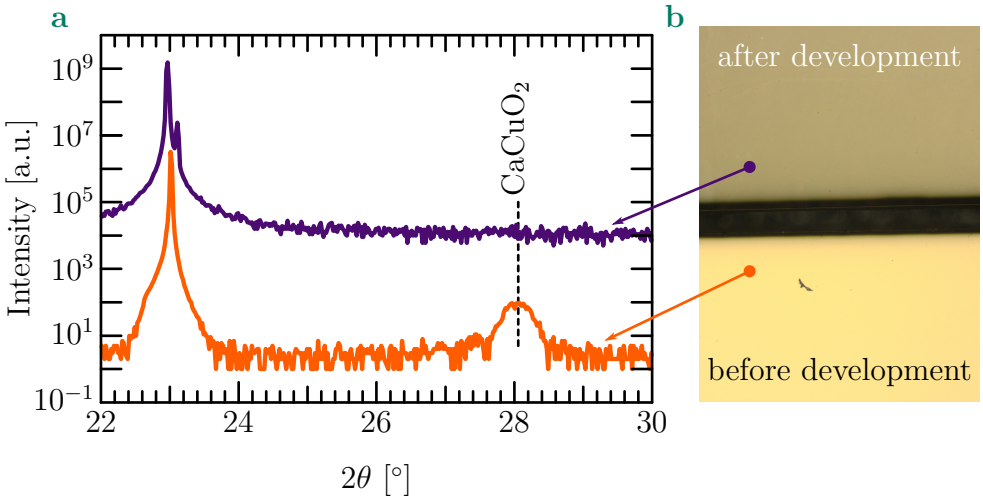

Figure 4.15: Influence of the photolithographic developer on the $SrTiO_3/CaCuO_2$ thin films. **a** X-ray diffraction before (bottom) and after (top) immersing a sample in the developer. **b** Image of the sample after development (top) compared to an as-grown sample (bottom) acquired with an optical microscope.

a few seconds in the photoresist developer (Microposit™ 351 Developer from *micro resist technology GmbH*), the colour of the sample completely changed. This is illustrated in the views from an optical microscope shown in Fig. 4.15b where one notices the difference between the sample after immersion in the developer (top) and a bilayer just after the growth. Measuring X-ray diffraction on the former reveals that the infinite layer $CaCuO_2$ peak is not present anymore (top curve in Fig. 4.15a). The use of photolithography to define the top-gate electrode is therefore challenging in these systems. We indeed observed that the infinite-layer cuprates are very sensitive to any type of solvent, which should be avoided as much as possible. For this reason we didn't try other brands/products for the developer, even if photolithography should be possible as it was reported in $SrTiO_3/CaCuO_2$ superlattices [43].

The deposition of a metallic layer with the shape shown in Fig. 4.14 can also be achieved using a shadow mask. To manufacture these masks, standard machining techniques to pierce holes in a metallic foil can be used. The main limitation of such an approach is the minimal dimension of the holes that can be mechanically achieved, which is of the order of 100 μm. Similar sizes are challenging when using a thin $SrTiO_3$ layer as top-gate dielectric because they can lead to current leakage. In order to achieve shadow masks with holes of the order of tens of micrometres we developed a fabrication process based on electrical discharge machining (EDM).

The working principle of an electrical discharge machining system is shown in Fig. 4.16a: a voltage is applied between a cathode and the metallic piece that has to be machined (being the anode), both immersed in a dielectric liquid. The cathode is progressively approached to the anode: the electric

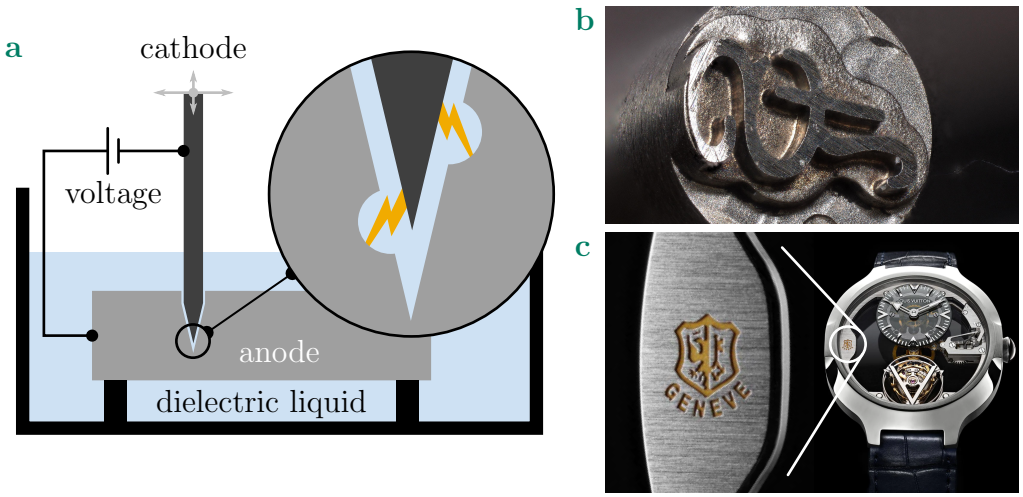

Figure 4.16: Electrical discharge machining. **a** Scheme representing the working principle (described in the main text) of an EDM; the inset shows a zoom of the region between the cathode and the anode during a discharge which determines the erosion process. **b** A hardened steel punching stamp for a jeweller (Sandy Rey, Switzerland) with a diameter of 1.8 mm (image courtesy of Jorge Cors). **c** The "Poinçon de Genève" engraved with an EDM on a *Louis Vuitton* watch [202].

field increases until it reaches the breakdown point of the dielectric liquid. A spark occurs between the electrodes and creates a plasma which remains constrained by the relatively high density of the liquid [203]. Inside the plasma the temperature is of the order of 40000 K, locally melting the anode and the cathode; the vaporisation of the electrodes is however limited due to the high plasma pressure. Because of the mass difference of positively and negatively charged particles inside the plasma, the control of the spark duration (by the electronic circuit of the machine) determines which between the anode (short time < 10 μs) or the cathode (typically 10-100 μs) is more eroded. When the current is stopped, the plasma is quenched and its pressure decreases causing partial explosion of the superheated electrodes as schematically illustrated in Fig. 4.16a (zoom).

EDM can be used to engrave metallic surfaces, pierce metals and cut out pieces when complex shapes have to be manufactured with a high precision. A set of motors is used to control the height of the cathode and its position to engrave or cut out the desired shape into the anode. One of the great advantages of this technique is that the cathode shape is transferred into the anode, as the sparks occur where the distance between the cathode and the

anode is the shortest. Consequently, using a small wire (tens of micrometres in diameter) allows us to manufacture holes/cuts of the right order of magnitude for our top gating experiment. Impressively, the use of scanning tunnelling microscope tips as cathodes provides the ability to pierce holes with a diameter smaller than 10 μm.

The EDM machines that were used in this work for the fabrication process of the shadow masks have been developed and are operated by Jorge Cors and Jean-Claude Crost working in PHASIS, a spin-off company of the University of Geneva. Fig. 4.16b and c show two application examples of high precision EDM: a punching stamp for a jeweller (b) and a high precision engraving (c) using this method to stamp the "Poinçon de Genève"[3] at the University of Geneva.

In order to fabricate the shadow masks for the top gating experiment 50 μm thick brass foils are used and holes are pierced with 200 μm tungsten wires and 40 μm tungsten carbide wires; an example of such a shadow mask is shown in Fig. 4.17a. The mask is then aligned on top of the pre-patterned sample

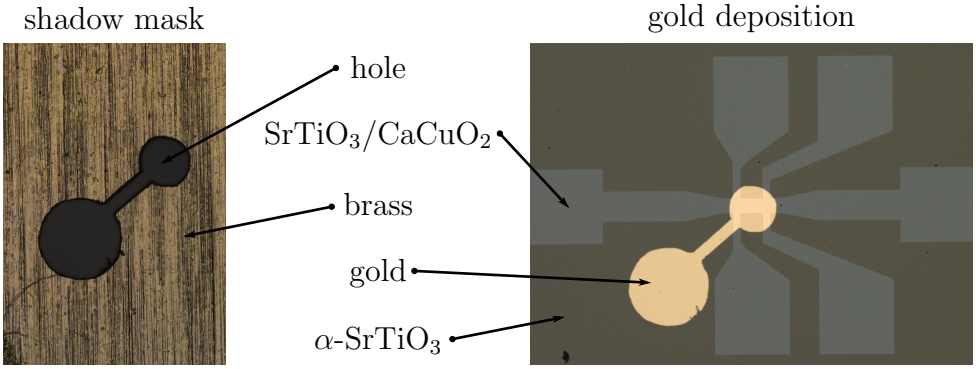

Figure 4.17: Shadow masking for top electrode deposition. **a** The cut-out brass foil realised by EDM for the shadow mask. Using the mask-aligner, a precise alignment of the hole on top of the pre-patterned Hall bar is possible. **b** A field-effect device defined by pre-patterning and shadow masking – gold was used for the top electrode. The diameter of the largest and the smallest circles as well as the width of the connecting line are respectively 270 μm, 160 μm and 40 μm.

using a mask aligner, usually employed for photolithography but adapted for this specific purpose. The mask is fixed with double-sided Kapton tape on the edges of the substrate. The metallic layer can be deposited by sputtering (Au, Pt) or electron beam evaporation (Al, Au, Cr, Cu, Pt, Sc, Ti), the latter being more directional is generally preferred as it leads to much better defined electrodes. A final Hall bar device, with a top-gate electrode, is shown in Fig. 4.17b.

[3]The "Poinçon de Genève" is a hallmark for standard of excellence certifying the origin, quality and reliability of a watch or a jewel on which it is engraved [204, 205].

4.5 Conclusion and outlook

Unfortunately, as our $SrTiO_3/CaCuO_2$ bilayers are not superconducting yet, we have not been able to conduct the gating experiment, presented in Section 4.1, to study the influence of the copper-apical-oxygen distance on the superconducting critical temperature. The preliminary results obtained with the O_2/O_3 mixture are, however, motivating our efforts to search for the optimal growth conditions employing a new ozone generator which allows the delivery of larger ozone content into the chamber.

Chapter 5

Oxygenation of infinite-layer thin films

5.1 Motivation

The infinite-layer cuprates, $ACuO_2$ (A = Ca, Sr, Ba) have Cu in a divalent state, leading to an insulating behaviour. However, these systems can be doped as described in Section 2.2.3: for example, by SrO defect layers in $(Ca_{1-x}Sr_x)_{1-y}CuO_2$ [106] or by apical oxygen atoms in $BaCuO_2/SrCuO_2$ superlattices [120] or $SrTiO_3/CaCuO_2$ heterostructures [43, 44]; in this way infinite-layer based systems become superconducting. For the hole doped heterostructures, the emergence of superconductivity is thought to be associated with the presence of additional oxygen atoms.

The control of the oxygen sublattice can also be used to modify the physical properties of a material in the vicinity of the infinite layer as reported in $LaNiO_3/SrCuO_2$ superlattices [206]. In that work, the presence of apical oxygen atoms was linked to the precise control of the $SrCuO_2$ layer thickness [207, 208], offering a way to control the Ni coordination at the interface. With such an approach, the conducting state of the nickelate layer was changed from metallic (in presence of apical oxygen) to insulating (in absence of apical oxygen). Similarly, the magnetisation of $LaCoO_3$ layers can be enhanced in $LaCoO_3/SrCuO_2$ superlattices through control of the oxygen sublattice in $SrCuO_2$ [209]. Furthermore, the magnetic properties in $SrRuO_3$, sandwiched between two $SrCuO_2$ layers, depend strongly on the octahedral tilts, which can be controlled by different oxygen arrangements in neighbouring $SrCuO_2$ layers [210].

These examples demonstrate the importance of controlling the oxygen arrangement in infinite-layer cuprates to achieve the desired functionality in artificial structures [211]. Consequently, understanding the oxidation process during the growth is crucial and detailed investigations are still needed. In the present chapter, the role of the chemical pressure (alkaline ionic size) and the

growth parameters (epitaxial strain and oxidising atmosphere) used during the deposition of $CaCuO_{2+\delta}$ and $SrCuO_{2+\delta}$ thin films[1] is investigated, demonstrating their importance for the control of the amount of apical oxygen atoms into the infinite-layer structure. Notice that for this study the presence of ozone was established for growth using the O_2/O_3 mixture. The work presented in this chapter was done in strong collaboration with Marios Hadjimichael (also in the group of Jean-Marc Triscone).

5.2 Growth of $CaCuO_{2+\delta}$ and $SrCuO_{2+\delta}$ thin films in highly oxidising atmospheres

Both $CaCuO_{2+\delta}$ and $SrCuO_{2+\delta}$ are deposited using the same PLD system as described in Section 3.1.2, and the growth parameters used here are summarised in Table 5.1 for the two systems. It is important to mention that,

	T_g [°C]	d_{TS} [cm]	F [J/cm^2]	f [Hz]	P [mbar]
$CaCuO_2$	650-700	3-4	0.8	1-2	0.25-0.50
$SrCuO_2$	550-600	4	0.8	2	0.25-0.50

Table 5.1: Growth parameters for $CaCuO_{2+\delta}$ and $SrCuO_{2+\delta}$ thin films. T_g is the substrate temperature during growth, d_{TS} the target-to-substrate distance, F the laser fluence, f the repetition rate and P the pressure. Other parameters, especially concerning the oxidising power will be specified later.

as a consequence of the results presented in Section 4.2.3, the sample growths are done with the delivery tube in (pos2); that is, a tube-to-substrate distance of about 1.5-3 cm with the delivery tube pointing toward the substrate. The oxidising power of the growth atmosphere, being crucial for the present study, can be controlled by means of three parameters: the pressure, the ozone concentration in the O_2/O_3 mixture and the O_2/O_3 gas flow; in all three cases, the higher the parameter value, the higher the oxidising power. Most of the samples have been deposited using the Atlas UHC ozone generator (see Section 3.1.2), allowing the control of the O_3 percentage, the only exceptions being the first $SrCuO_2$ thin films presented in this section.

Fig. 5.1 shows a comparison of $\theta - 2\theta$ scans for $SrCuO_{2+\delta}$ thin films grown onto $SrTiO_3$ substrates in different oxidising atmospheres. The growth in O_2 (bottom curve) leads to films with infinite-layer structure and high crystalline quality. Analysis of the XRD scan reveals a layer thickness of 59 unit cells

[1] In the following we consider $CaCuO_{2+\delta}$ and $SrCuO_{2+\delta}$ as opposed to $CaCuO_2$ and $SrCuO_2$ as the oxygenation process discussed in this chapter can lead to different oxygen content (δ) compared to the infinite-layer phase.

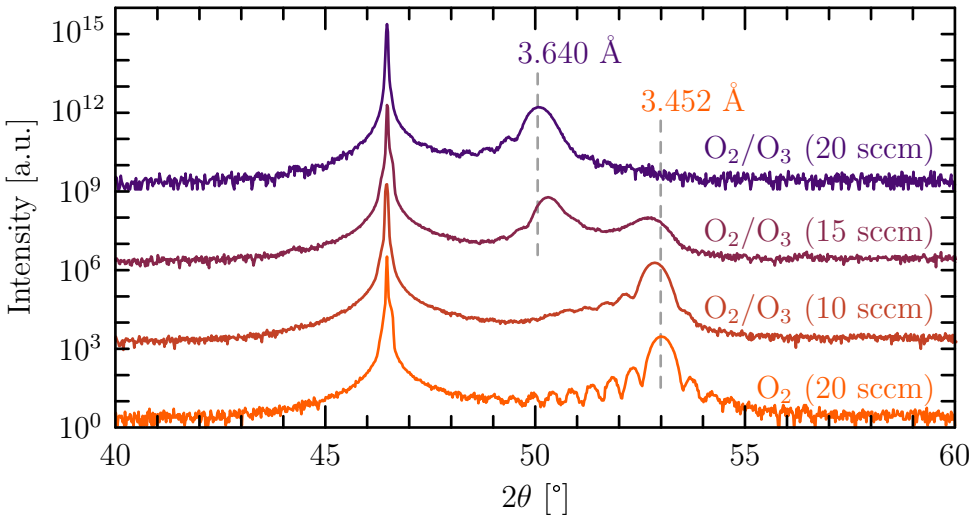

Figure 5.1: $\theta - 2\theta$ scans of $SrCuO_{2+\delta}$ films deposited under various oxidising conditions. The four curves (orange to purple) are acquired around the $SrTiO_3$ 002 and the $SrCuO_{2+\delta}$ 002 Bragg peaks. The bottom curve is a scan of a film deposited in pure oxygen, showing only reflections of the infinite-layer phase. From bottom to top the oxidising power is progressively increased from pure O_2 to O_2/O_3 by controlling the gas flow rate (between 10 and 20 sccm).

(u.c.) and a c-axis of 3.452 Å ($2\theta = 52.990°$), a value in agreement with the literature [102, 111, 114, 212].

Introducing ozone into the chamber atmosphere (5% of O_3) does not lead to a continuous evolution of the lattice parameter but results in a sharp transition to a phase with a longer c-axis (3.640 Å, $2\theta = 50.058°$). The measurements of Fig. 5.1 show a gradual redistribution of the peak intensity between the infinite-layer and the high c-axis phase as the oxidising power is progressively increased. In this case, the oxidising power is increased by controlling the O_2/O_3 gas flow, while keeping the total gas pressure constant (0.5 mbar).

The origin and the properties of the elongated phase will be studied in more detail in Chapter 6, but for the present study we consider, in agreement with previous works [213–215], that such an elongation is linked to the insertion of additional oxygen atoms in the Sr planes, above the Cu atoms.

Films of $CaCuO_{2+\delta}$ show a completely different behaviour from the one of $SrCuO_{2+\delta}$. Fig. 5.2 shows $\theta - 2\theta$ scans around the 001 reflection of $CaCuO_{2+\delta}$ layers grown on $NdGaO_3$, in different oxidising atmospheres. The highly oxidising growth conditions are achieved by keeping the pressure (0.25 mbar) and the gas flow (20 sccm) constant while the O_3 fraction is controlled between 5% and 17%. Despite the increase of ozone content in the gas mixture, the c-axis does not change its value, in contrast to $SrCuO_{2+\delta}$, indicating that $CaCuO_{2+\delta}$ remains in the infinite-layer structure, that is $\delta = 0$, regardless of the oxidising power of the atmosphere. One could argue that a small increase from 3.178 Å

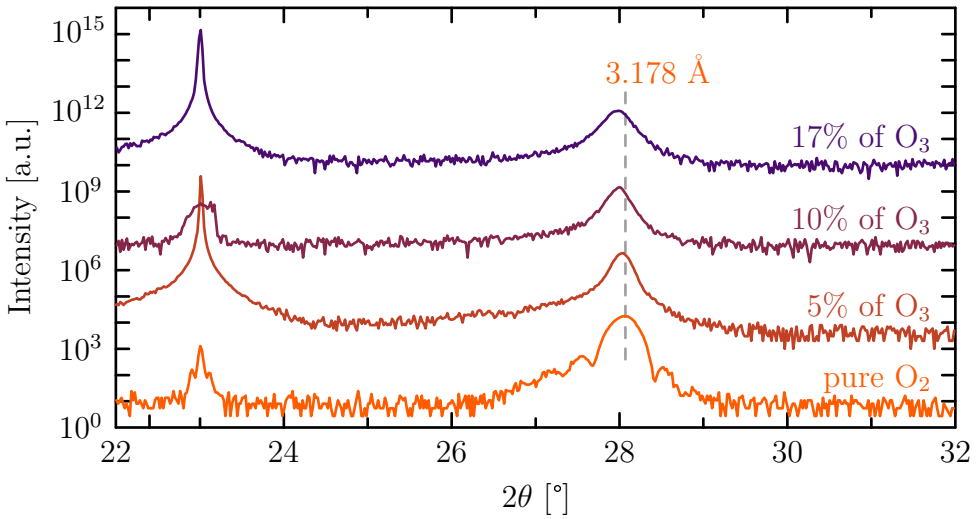

Figure 5.2: $\theta - 2\theta$ scans of $CaCuO_{2+\delta}$ films deposited with various oxidising powers. The four curves (orange to purple) are acquired around the $NdGaO_3$ 110 and the $CaCuO_{2+\delta}$ 001 Bragg peaks. The bottom curve is a scan of a film deposited in pure oxygen, representative of the infinite-layer phase. From bottom to top the oxidising power is progressively increased from pure O_2 to O_2/O_3 with 17% of O_3. The film quality is lower than the one reported in Chapter 4 because these films were grown using the Atlas UHC ozone generator and optimisation is still required as mentioned in Section 4.3.2). Note that for some measurements the substrate peak has a low intensity, this is due to the fact that the films grow slightly tilted compared to the substrate, and aligning the sample for the film and the substrate is not always possible.

(pure O_2) to 3.186 Å (17% of O_3) is observed, compatible with the incorporation of a small amount of oxygen in the $CaCuO_2$ structure as reported in [216]. However, the change in c-axis is much smaller (0.3%) than the one observed in the $SrCuO_{2+\delta}$ case (5.4%) and we can confidently say that $CaCuO_2$ grows in the infinite-layer phase independently of the oxidising power. This corroborates previous studies that have also observed the stability of the infinite-layer structure in $CaCuO_2$ films when deposited in highly oxidising conditions on $SrTiO_3$ [215] and $NdGaO_3$ [44].

5.3 The effect of the epitaxial strain on the oxygenation process

To understand the difference between the two infinite-layer compounds, we investigated the role of the epitaxial strain imposed by the substrate on the films. In transition metal oxides such as nickelates [217, 218], ferrites [219, 220] or cobaltites[221], the insertion of additional oxygen atoms into the al-

kaline/rare earth planes modifies the infinite-layer structure towards first a brownmillerite and then a perovskite phase. When such a transition happens in these compounds, a change from a highly tetragonal phase to a pseudocubic phase occurs with a compression of the in-plane and an expansion of the out-of-plane lattice parameters (see Table 5.2). One could therefore expect that a

	Nickelates				Ferrites	
	$LaNiO_2$	$LaNiO_3$	$NdNiO_2$	$NdNiO_3$	$SrFeO_2$	$SrFeO_3$
a [Å]	3.96	3.84	3.92	3.81	3.99	3.86
c [Å]	3.38		3.31		3.47	

Table 5.2: Lattice parameters for the tetragonal phase of the infinite-layer structure and for the pseudocubic phase of the perovskite structure for nickelates and ferrites. The values are extracted from References [219, 222, 223].

compressive strain imposed on the in-plane lattice parameter of $SrCuO_2$ and $CaCuO_2$ should promote the insertion of oxygen in the Ca or Sr planes, while a tensile strain would make the incorporation of oxygen less favourable.

The in-plane strain values, calculated using the bulk lattice parameters of $CaCuO_2$ and $SrCuO_2$, for films deposited on multiple substrates, are presented in Table 5.3. When $CaCuO_2$ is deposited on $NdGaO_3$, a small tensile

	$LaAlO_3$	$NdGaO_3$	LSAT	$SrTiO_3$	$DyScO_3$
$CaCuO_2$	-1.8%	**+0.1%**	+0.3%	+1.3%	+2.5%
$SrCuO_2$	-3.5%	-1.7%	-1.5%	**-0.5%**	+0.7%

Table 5.3: Strain values (compressive strain in orange, tensile in purple) for 001-oriented $CaCuO_2$ and $SrCuO_2$ on different substrates. The values in bold indicate the best epitaxial match.

strain (+0.1%) is imposed, whereas $SrCuO_2$ on $SrTiO_3$ is under compressive strain (-0.5%). Although these two substrates have been selected because they are the best epitaxial match with the compounds and have been shown to favour the stabilisation of the infinite-layer structure [183], they could indeed hinder or favour the insertion of oxygen.

In order to test a possible strain effect on the incorporation of additional oxygen atoms in the infinite-layer cuprates, compressive strain is applied on $CaCuO_2$ and tensile strain on $SrCuO_2$ films. Considering the data in Table 5.3, $DyScO_3$ imposes a tensile strain of +0.7% on $SrCuO_2$ films, similar to the strain imposed by $SrTiO_3$ but of opposite sign. The XRD measurements for such thin films, deposited in different oxidising conditions, are shown in Fig. 5.3a. They reveal that, similarly to $SrCuO_{2+\delta}$ on $SrTiO_3$, the oxidising power determines the phase of $SrCuO_{2+\delta}$ grown on $DyScO_3$, largely independent of the strain

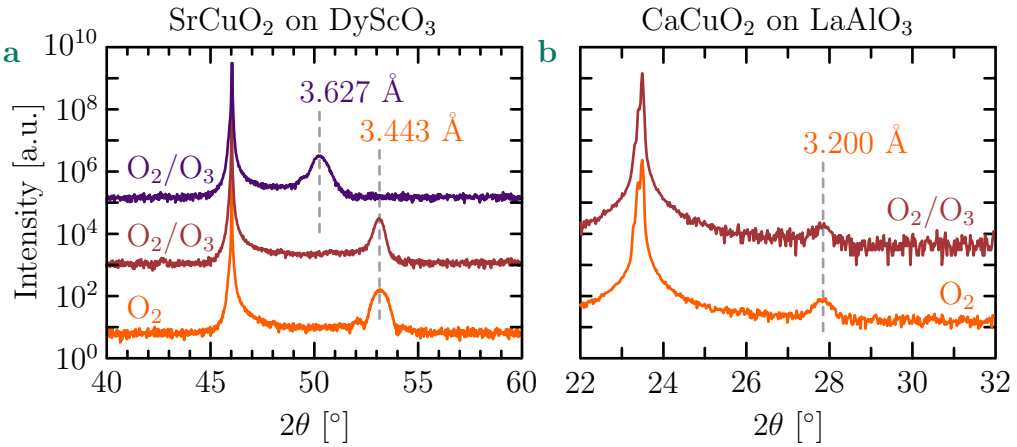

Figure 5.3: $\theta - 2\theta$ scans on $CaCuO_2$ and $SrCuO_2$ thin films with an opposite strain as compared to Fig. 5.1 and 5.2, showing the effect of the oxidising power. **a** $SrCuO_2$ on $DyScO_3$ (-0.7%) in pure oxygen (bottom), using 5% of O_3 at 0.25 mbar (middle) and 5% of O_3 at 0.5 mbar (top). **b** $CaCuO_2$ on $LaAlO_3$ (-1.8%) in O_2 (bottom) and using 5% of O_3 at 0.25 mbar (top).

state. For pure O_2, the infinite-layer structure is observed, while in O_2/O_3, the $SrCuO_{2+\delta}$ phase with the long c-axis is achieved, although this requires a higher oxidising power (in this case a higher pressure was used) than for layers on $SrTiO_3$.

To impose a compressive strain on $CaCuO_2$, $LaAlO_3$ substrates are used (see Table 5.3). Despite the use of O_2/O_3 in our tests and the large compressive strain (-1.8%), the $CaCuO_2$ films remain in the infinite-layer structure, as shown in Fig. 5.3b. Interestingly, a $CaCuO_2$ film deposited at a higher pressure (0.50 mbar) does not show Bragg peaks, indicating that these conditions are not favourable for the growth of $CaCuO_{2+\delta}$. This is in line with our prior observation that $CaCuO_2$ cannot accommodate additional oxygen atoms.

Fig. 5.4 summarises the results for the $CaCuO_{2+\delta}$ and $SrCuO_{2+\delta}$ thin films grown under different strain states and in various oxidising atmospheres. We note that the role of strain does not seem to affect much the ability of the $ACuO_{2+\delta}$ phase to include additional oxygen atoms in the alkaline planes: $CaCuO_2$ remains in the infinite-layer phase, independently of the substrate, contrary to $SrCuO_2$, which becomes $SrCuO_{2+\delta}$ when grown in highly oxidising conditions.

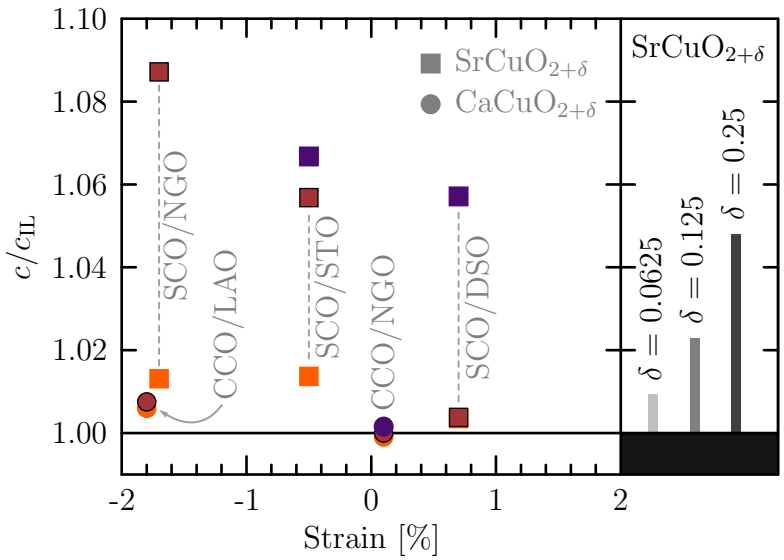

Figure 5.4: Summary of the results showing the out-of-plane axis of the films normalised to the bulk infinite-layer value (see Table 2.1) as a function of the strain state (left panel). Square symbols are for $SrCuO_{2+\delta}$ and circles for $CaCuO_{2+\delta}$, while the oxidising power is represented by the colour of the symbol: orange stands for pure O_2, brown with black border for low oxidising power in O_2/O_3 and purple for higher oxidising conditions (as compared to brown) in O_2/O_3. The following abbreviations are used: CCO for $CaCuO_2$ and SCO for $SrCuO_2$ for the films and DSO for $DyScO_3$, LAO for $LaAlO_3$, NGO for $NdGaO_3$, and STO for $SrTiO_3$ for the different substrates. On the right panel, the calculated c-axis parameter of $SrCuO_{2+\delta}$ for different oxygen contents (δ) is shown.

5.4 The key role of the A-cation size

5.4.1 First-principle calculations

To better understand the key difference between $CaCuO_{2+\delta}$ and $SrCuO_{2+\delta}$, *ab-initio* calculations have been performed. They have been carried out by the team of Prof. Philippe Ghosez at the University of Liège and Dr. Yajun Zhang at the Lanzhou University using the projector augmented wave (PAW) method implemented in the Vienna Ab initio Simulation Package (VASP). The strongly-constrained-appropriately-normed (SCAN) is used as the exchange-correlation functional. A $2 \times 2 \times 2$ supercell, $6 \times 6 \times 7$ k-point mesh and cutoff energy of 700 eV are used for the structural optimisations. The lattice parameters and internal coordinates of atoms are fully relaxed with energy tolerance of 10^{-7} eV and force tolerance of 10^{-3} eV/Å, respectively.

Calculations were performed to investigate oxygen rich structures, allowing one to obtain the theoretical structures of $ACuO_{2+\delta}$ with various $\delta \geq 0$ and different A-cations. Some structures with $\delta = 0$, 0.125 and 0.25 are sketched

in Fig. 5.5. These theoretical structures also make it possible to estimate the formation energy E_f required to insert an additional oxygen atom into the infinite-layer phase, this is discussed in Section 5.5.1.

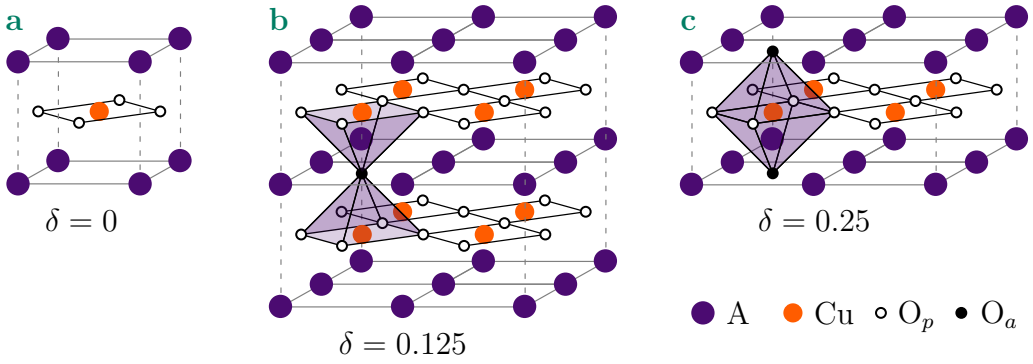

Figure 5.5: Sketches of multiple $ACuO_{2+\delta}$ superstructures for different oxygen contents, showing the apical oxygen sitting in the alkaline A plane and ordering differently depending on δ: here shown for $\delta = 0$ **a**, $\delta = 0.125$ **b** and $\delta = 0.25$ **c**. O_p stands for the planar oxygen, in the CuO_2 planes while O_a represents the apical ones.

As an example, a rough estimation of the amount of apical oxygen present in the $SrCuO_{2+\delta}$ layers can be obtained by comparing the c-axis parameters measured from XRD with the values calculated *ab-initio* for several δ values. Some calculated c-axis values are shown in the right panel of Fig. 5.4. One sees that theory fits the experimental values for $\delta > 0.25$, assuming an oxygen ordering as shown in Fig. 5.5c; this estimation of the oxygen content is in agreement with a previous report for films exposed to plasma annealing [213].

5.4.2 The valence bond sum

The valence bond sum is en empirical method allowing the valence of the atoms in a structure based on the interatomic distances to be estimated. According to I. D. Brown [224], the bond valence sum V_i of the atom i is defined as:

$$V_i = \sum_j s_{ij} = \sum_j \exp\left(\frac{r_0 - r_{ij}}{B}\right) \tag{5.1}$$

with s_{ij} denoting the valence of the bond between the cation (anion) i and the surrounding anions (cations) j; in the present work i corresponds to Sr, Ca or Cu while j denotes the surrounding oxygen atoms. The valence of a specific bond is determined empirically, using $s_{ij} = \exp\left(\frac{r_0 - r_{ij}}{B}\right)$, for which r_0 and B can be determined for a pair of anion-cation by fitting this relation on a large number of known structures, where the interatomic distance (r_{ij}) between atom i and j as well as the atomic valence are precisely known. The

values of r_0 and B are tabulated for a given pair of elements, see for example References [225, 226], allowing one to calculate the valence of a specific atom in any structure. For our calculation, the following values were used for r_0: 1.967 Å for Ca-O [225], 2.090 Å for Sr-O [227] and 1.649 Å for Cu-O [228] and $B = 0.37$ Å, independently on the bond, as suggested in [225].

The bond valence sum, whose calculation depends on the knowledge of the length of the chemical bonds, reflects electronic (amounts of electrons in the bonds) and non-electronic (for instance, steric strain) factors and has been previously used to determine crystalline structures [224, 229]. It is worth mentioning that the calculations were done using unstrained structures, which have been obtained for bulk from the first-principle calculations, but as the strain in these structures is relatively small (Table 5.3), we expect this approach to give reasonable results.

5.4.3 Results

To understand the key factors differentiating the behaviour of $SrCuO_{2+\delta}$ and $CaCuO_{2+\delta}$, we calculated the bond valence sum (V_i) of the different cations (Sr, Ca and Cu) for δ=0, 0.0625, 0.125 and 0.25. As observed in Fig. 5.6a, the bond valence sum is close to +2 for Ca and Sr (purple curves) for $\delta \leq 0.125$ and decreases only slightly for δ=0.25. These results indicate that the A-O coordination environment is not responsible for the different behaviours of $CaCuO_{2+\delta}$ and $SrCuO_{2+\delta}$ as V_{Ca} and V_{Sr} have similar behaviours.

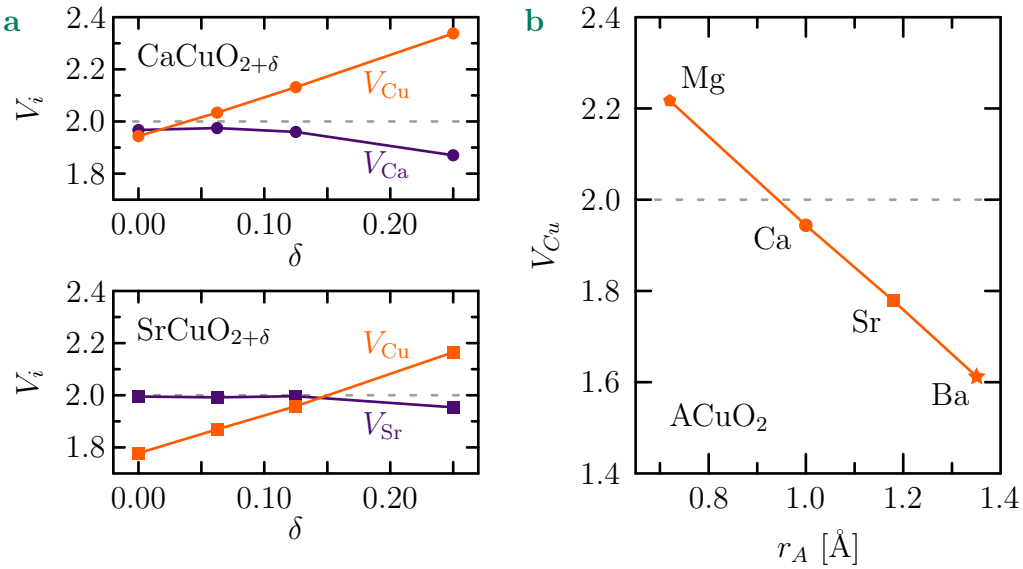

Figure 5.6: Bond valence sum for Ca, Sr and Cu in $ACuO_{2+\delta}$. **a** V_{Ca}, V_{Sr} and V_{Cu} as a function of the oxygen content for $CaCuO_{2+\delta}$ (top) and $SrCuO_{2+\delta}$ (bottom). **b** The Cu valence for various A-cations, as a function of their atomic radius (r_A).

Differently, we see that the bond valence sum of Cu increases linearly as the oxygen concentration is increased. As the radius of Sr is larger than Ca, the smaller Cu-O bond length in $CaCuO_2$ gives intrinsic stronger Cu-O Pauli repulsion and almost saturated coordination. Thus, even for low δ values, Cu-O in $CaCuO_{2+\delta}$ becomes over-coordinated ($V_{\mathrm{Cu}} > 2$) and is not allowed to incorporate additional oxygen atoms (see also Section 5.5.2). Due to the initial smaller V_{Cu} in $SrCuO_2$, $SrCuO_{2+\delta}$ is capable of accommodating extra oxygen atoms before being over-coordinated. Since there is no change in the electronic configuration of Cu in the $CaCuO_2$ and the $SrCuO_2$ structures that modifies its bond valence sum, it seems therefore that the ability of $ACuO_2$ to accommodate apical oxygen is highly susceptible to the A-site ionic radius, the larger the radius, the smaller the initial Cu bond valence and the easier the incorporation of oxygen.

To test whether our argument on the steric strain is general and applicable to other infinite-layer cuprate oxides ($MgCuO_2$ and $BaCuO_2$), V_{Cu} is computed for the four compounds with $\delta = 0$ and plotted in Fig. 5.6. A linear decrease of the Cu bond valence is observed as the radius of the A-cation increases, supporting our argument that doping of oxygen is closely correlated to the A-site atomic radius. Note that $MgCuO_2$ has not been synthesised in experiments, which may be due to its unrealistically high coordination.

5.5 Formation energy of the oxygen rich phase

5.5.1 Theory

Inspired by the first-principle calculations in [230] a definition of the formation energy E_f required to insert a charge neutral isolated oxygen in $ACuO_2$ (A = Mg, Ca, Sr, Ba) can be expressed as follows:

$$E_{f,\mu=0} = \frac{1}{n_D}\left[E_D - \left(E_0 + \frac{n_D}{2}E_{O_2}\right)\right] \tag{5.2}$$

where n_D is the number of additional oxygen atoms, E_D and E_0 correspond to the total DFT-derived energies of the doped and undoped bulk supercells, respectively, and E_{O_2} is the energy of a single O_2 molecule. Physically this equation can be understood as the energy difference between the doped phase and the infinite-layer one, considering that the oxidising environment of the growth (O_2 or O_2/O_3) favours the doped phase. If $E_f < 0$, the oxygen rich structure ($\delta > 0$) is energetically favourable compared to the $ACuO_2$ phase. On the other hand, $E_f > 0$ means that this structure is unfavourable. Note that Eq. 5.2 is evaluated at 0 K and does not take into account the growth conditions as the temperature (T) and the pressure (P); including the chemical potential for oxygen, $\mu_{O_2}(P,T)$, allows one to include these parameters in the

calculations leading to:

$$E_{f,\mu} = \frac{1}{n_D}\left[E_D - \left(E_0 + \frac{n_D}{2}\left(E_{O_2} + \mu_{O_2}(T,P)\right)\right)\right]. \tag{5.3}$$

Using Eq. 5.2 and the fact that for a single oxygen atom one has $\mu_O = \frac{1}{2}\mu_{O_2}$ it can be rewritten as:

$$E_{f,\mu} = E_{f,\mu=0} - \mu_O(T,P). \tag{5.4}$$

The chemical potential can be calculated by the Chemical Potential Calculator, available online [231], based on previous theoretical calculations [232].

5.5.2 Results

To support the results from the bond valence sum and compare with the behaviour shown in Fig. 5.6b, the formation energy $E_{f,\mu=0}$ of the $ACuO_{2.125}$ doped phase for different A-cations is calculated. The results are shown in Fig. 5.7a: a similar "linear" trend can be observed as a function of atomic radius (except for $MgCuO_2$ due to a larger atomic displacement in the defective system). This confirms the key role of the A-cation in the oxygenation process of the infinite-layer cuprates.

To evaluate the effect of the epitaxial strain, the evolution of the formation energy with respect to the strain value is calculated. Fig. 5.7b shows the formation energy ($E_{f,\mu=0}$) of $CaCuO_{2.125}$ and $SrCuO_{2.125}$ under different compressive and tensile strain states. One has to consider that, as shown in Eq. 5.4, the absolute value of the formation energy depends on the oxygen chemical potential; however, using identical growth conditions (O_2 or O_2/O_3, pressure and temperature), the chemical potential adds simply a constant to the formation energy of the different phases. Therefore, the relative values between the unstrained phases and their evolution with strain are the parameters of interest. It is indeed not straightforward to obtain a reliable value of the chemical potential for highly oxidising growth conditions, as an O_2/O_3 mixture is used while pure O_2 is considered in the calculations.

Looking at Fig. 5.7b, a monotonic decrease of formation energy from tensile to compressive strain can be observed for both phases, in line with our experimental results on $SrCuO_{2+\delta}$ (see Fig. 5.4). However, the change in energy ($\sim$ 0.3 eV) due to the epitaxial strain is not enough to overcome the energy difference set by the different atomic radii ($\sim$ 0.8 eV).

We can summarise our investigation on the oxygenation of the infinite-layer thin films as follows. The impact of the growth atmosphere, A-site cation and epitaxial strain on the oxidation of the infinite-layer cuprates has been thoroughly investigated experimentally and by first-principles calculations. The results demonstrate that the Cu-O coordination environment determined by

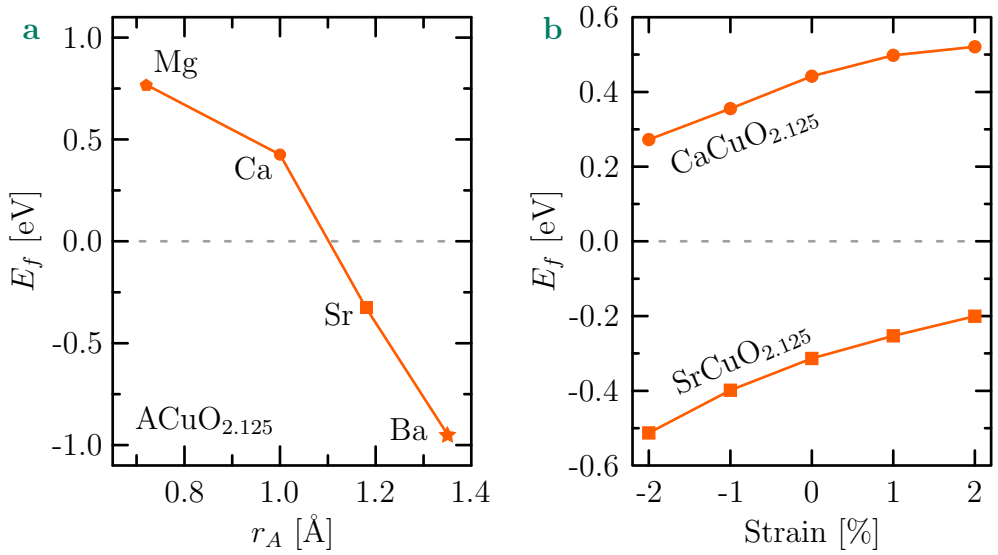

Figure 5.7: Formation energy of $ACuO_{2.125}$. **a** E_f as a function of the A-cation atomic radius (r_A) for the doped phase: the smaller the radius the larger the formation energy, confirming the bond valence sum results shown on Fig. 5.6b. Note that the absolute value of the energy is not relevant as it depends on the pressure and temperature through the chemical potential in Eq. 5.4. **b** Formation energy of $CaCuO_{2.125}$ (circles) and $SrCuO_{2.125}$ (squares) as a function of the strain state.

the A-site ionic radius is the dominant factor that affects the insertion of apical oxygen in the structure. The calculations show that a larger ionic radius leads to a less coordinated planar Cu-O square with a stronger ability to accommodate extra oxygen atoms. Calculations of the $CaCuO_{2+\delta}$ and $SrCuO_{2+\delta}$ structures (for $\delta > 0$) and comparison with other transition metal oxides reveal that incorporation of oxygen is accompanied by contraction of the in-plane and elongation of the out-of-plane lattice parameters. This effect is similar to what happens to a system under compressive strain yet opposite to the effect of tensile strain. Thus, oxidation is revealed to be favoured by compressive epitaxial strain and hindered by the competitive tensile epitaxial strain. Our experimental results highlight that A-site cation and the oxidising power used during the growth are the key parameters that control the oxidation state of the infinite-layer cuprates; the strain induced by the substrate into the film also plays a secondary role. These three parameters may become useful tools to modulate the superconducting properties in cuprate heterostructures.

Chapter 6

Study of the high *c*-axis phase of $SrCuO_{2+\delta}$

6.1 Motivation

$SrCuO_{2+\delta}$ grown in highly-oxidising conditions appears to have an elongated structure along the out-of-plane direction. The origin of this high *c*-axis phase was briefly discussed in the previous chapter, in which it was assumed, based on previous studies [213–215], that the large *c*-axis originates from the incorporation of oxygen in the Sr planes. *Ab-initio* calculations have also shown that the crystalline structures of oxygen rich $CaCuO_{2+\delta}$ and $SrCuO_{2+\delta}$ phases have a longer *c*-axis. In the present chapter, a detailed analysis of this high *c*-axis phase is presented, supporting the above-mentioned idea that the $SrCuO_{2+\delta}$ thin films grown in O_2/O_3 are oxygen rich, that is $\delta > 0$. This work was done in collaboration with Marios Hadjimichael who initiated this research direction and was strongly involved in the project.

6.1.1 Origin of the high *c*-axis phase

$SrCuO_{2+\delta}$ thin films deposited in pure oxygen typically have a *c*-axis of about 3.458 Å: this value matches the infinite-layer structure (i.e. $\delta = 0$), in agreement with previous reports [102, 111, 114, 212]. In contrast, for the growths in a highly-oxidising atmosphere, the *c*-axis is on average 6% longer with $c = 3.668$ Å. In order to understand the possible origins for this high *c*-axis phase, we scanned the literature for reports of infinite-layer related structures with a similar elongated lattice parameter. In the following four possibilities are presented.

Defect layers in bulk materials As mentioned in Section 2.2.3, superconductivity in the hole-doped infinite-layer cuprates is associated with the appearance of defect layers that are naturally ordered as shown in Fig. 6.1a

for $A_{1-y}CuO_2$ (with A=$Sr_{1-x}Ca_x$) [106]. Different types of defect layers have

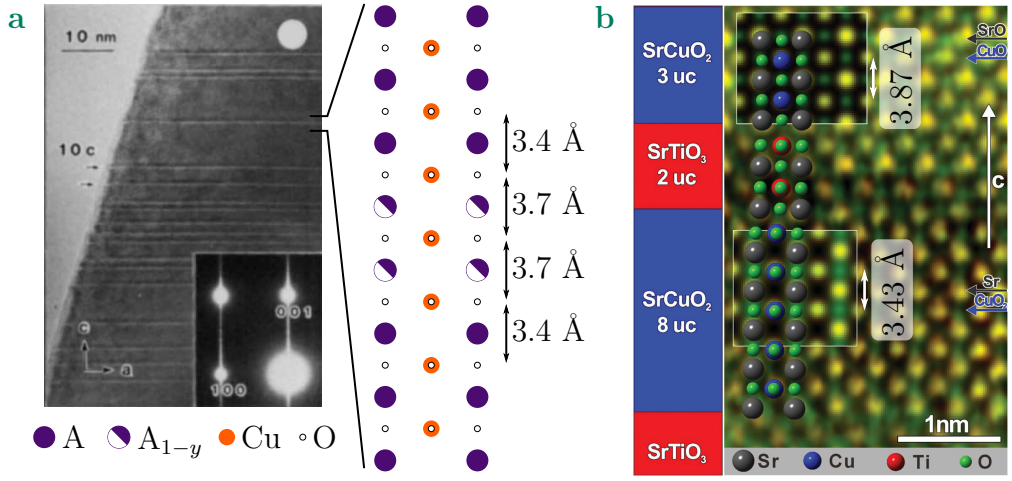

Figure 6.1: Possible origins for the high *c*-axis phase in $SrCuO_{2+\delta}$. **a** High-resolution electron microscope image (left) of a $(Ca_{0.4}Sr_{0.6})_{0.9}CuO_2$ crystal, showing the natural arrangement of the defect layers [106]. A sketch of one possible type of defect layer structure is also shown (right), adapted from [233]. As described in the text, the defect layer could have a different origin than the defective A-cation layer shown in the sketch. **b** Atomically resolved STEM image showing the chain and planar structures observed in a $SrCuO_2/SrTiO_3$ heterostructure for different $SrCuO_2$ thicknesses, reprinted and adapted from [208]. The chain-type structure is observed in the 3 u.c. thick $SrCuO_2$ layer, while the planar-type in the thicker one.

been reported: ordered cation deficient layers (schematically represented in Fig. 6.1a) [233], double Sr layers [97], substitution of a Sr-CuO_2-Sr block by $Sr_3O_{2\pm x}$ [234] or AO_δ-Cu-AO_δ instead of A-CuO_2-A (with A=$Ca_{0.3}Sr_{0.7}$) [118]. In all these cases the distance between two consecutive CuO_2 planes is found to be of the order of 3.7 Å, very similar to our high *c*-axis structure.

Apart from the latter they all involve an excess or a deficiency of A-cations, which is unlikely in our situation as the only difference between the infinite-layer and the high *c*-axis phase is the oxidising power during the deposition of the thin films. Thus, a change of oxygen ordering/content as described in [118] would be more likely to explain the elongated structure.

Chain and planar structure In Fig. 6.1b an atomically-resolved image of a $(SrCuO_2)_3/(SrTiO_3)_2/(SrCuO_2)_8/SrTiO_3$ heterostructure is presented [208]. Depending on the $SrCuO_2$ thickness in the block, the *c*-axis of $SrCuO_2$ is found to be 3.43 Å or 3.87 Å. This difference has been assigned to different orientations of the CuO_2 planes [207, 208]. For films thicker than a critical thickness, which depends on the A-site cation according to theory, the CuO_2 planes are observed to be perpendicular to the substrate surface, the so-called chain-type

configuration. In contrast, thicker films have the usual planar orientation of the CuO_2 planes in the infinite-layer structure.

The critical thickness for the transition between chain and planar structure for $SrCuO_2$ has been predicted to be about 5 u.c. [207]; consequently this mechanism is unlikely to be the cause for the high c-axis we observe in $SrCuO_2$ thin films, as they are all thicker than 10 u.c. Additionally, the c-axis of the chain type configuration is slightly too large to be fully compatible with our observations.

Additional oxygen atoms in the Sr planes The observation of an elongated phase for $SrCuO_2$ is in line with previous works indicating that the infinite-layer structure is modified in presence of ozone [215] or oxygen plasma [213, 214] with an expansion of the c-axis, from 3.45 Å to 3.65 Å. Particularly, in [214], the authors observe by high-resolution electron microscopy the appearance of a $2\sqrt{2}a \times 2\sqrt{2}a \times c_h$ superstructure in the ab-plane as illustrated in Fig. 6.2a (large grey square), after exposure of their thin films to highly-oxidising conditions. This superstructure is associated with the observed high

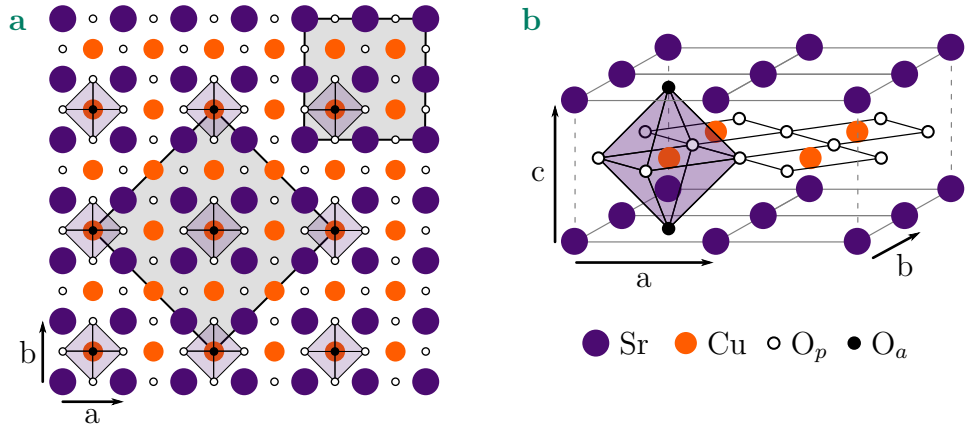

Figure 6.2: Possible structure of the high c-axis phase in $SrCuO_2$. **a** Sketch of the superstructure reported in [214] projected along the [001] direction. The large grey square indicates the $2\sqrt{2}a \times 2\sqrt{2}a \times c_h$ superstructure unit cell while the small one is the $2a \times 2a \times c_h$ illustrated in **b**, both representative of the same oxygen sublattice arrangement. O_p stands for the oxygen in the CuO_2 planes while O_a for the apical oxygen.

c-axis (c_h) as compared to the usual infinite-layer structure $a \times a \times c$. A comparison with previously studied structures of La-Sr-Cu-O compounds that show a similar superstructure allows the authors to conclude that the elongation of the out-of-plane parameter is associated with insertion of additional oxygen atoms in the Sr planes (see Fig. 6.2b). For such a superstructure in $SrCuO_{2+\delta}$ the excess of oxygen atoms is estimated to be of the order of $\delta = 0.25$.

The exposure to a highly-oxidising environment reported in [213–215] is similar to our PLD growth conditions, making this scenario the most convincing to explain the emergence of a high *c*-axis structure in $SrCuO_{2+\delta}$. One of the purposes of the present chapter is to confirm this statement by means of different experimental techniques.

Interestingly, similar elongation of the *c*-axis (3.65 Å) has been reported in electron-doped systems. It has been observed both in Nd-doped [235, 236] and La-doped [237] $SrCuO_2$ thin films. Such an elongation has been shown, by STEM measurements, to be linked to the insertion of apical oxygen atoms in the Sr planes, above the Cu, for samples with sufficient cation substitution. The additional oxygen atoms probably compensate (with holes) the electron doping introduced by the Nd or La substitution of Sr, such that the Cu valence stays 2+. For sufficient substitution this leads to a hole-doped behaviour according to investigations under scanning tunnelling microscopy [236, 237].

6.1.2 Consequences of the oxygen incorporation

Considering that the effect of the O_2/O_3 mixture during the deposition of $SrCuO_{2+\delta}$ is to introduce additional oxygen in the Sr planes, it is easy to understand that the copper valence should be modified. Indeed, when $SrCuO_2$ becomes $SrCuO_{2+\delta}$, copper is expected to be $Cu^{(2+2\delta)+}$, assuming the formal valence states 2+ and 2- for Sr and O. The copper valence can be written as $V_{Cu} = 2 + p$ with $p = 2\delta$, corresponding to hole doping for $\delta > 0$. Depending on the value of p, and consequently on the number of additional oxygen atoms, $SrCuO_{2+\delta}$ could potentially be superconducting (see Fig. 2.1b). As the optimal doping in cuprates is generally around $p = 0.16$ holes/Cu, one could expect the maximum T_c in $SrCuO_{2+\delta}$ for $\delta = 0.08$.

In this chapter the copper valence in $SrCuO_{2+\delta}$ is studied to find out more about the doping in this system with the aim of searching for superconductivity in the infinite-layer cuprates (see Section 6.6).

6.2 Structural analysis

To start with the study of the high *c*-axis phase in $SrCuO_{2+\delta}$, the structure is considered first. Fig. 6.3a shows the $\theta - 2\theta$ scan of a $SrCuO_2$ thin film deposited on $SrTiO_3$ with the infinite-layer structure (orange) in comparison with a $SrCuO_{2+\delta}$ thin film with a high *c*-axis (purple). Both structures are coherently strained to the $SrTiO_3$ substrate, as confirmed by reciprocal space maps around the $\bar{1}03$ Bragg reflections, shown in Fig. 6.3b; this is an indication that strain relaxation is not at the origin of the difference between the two phases.

Among the $SrCuO_2$ samples grown by PLD, we observe a slight variation

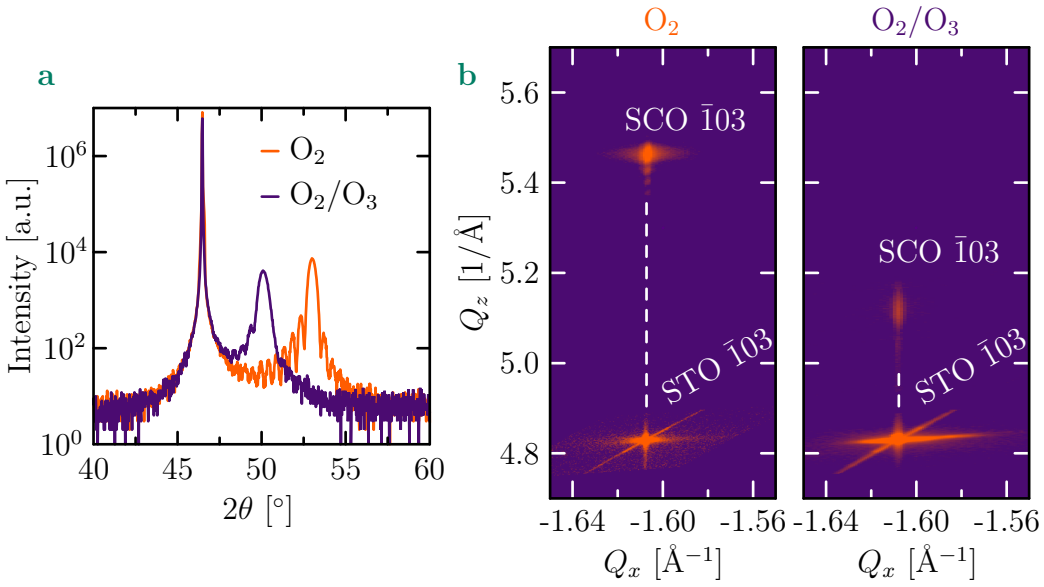

Figure 6.3: Comparison of XRD measurements for samples deposited in O_2 and in O_2/O_3. **a** $\theta - 2\theta$ scan around the 002 diffraction peak, showing the substantial change of c-axis for samples deposited in highly-oxidising growth conditions. **b** RSM around the $\bar{1}03$ Bragg reflections of the films and the $SrTiO_3$ substrate for sample deposited in O_2 (left) and in O_2/O_3 (right). The dashed line is a guide to the eye indicating the coherently strained in-plane structure.

Growth atm.	c_{min} [Å]	c_{max} [Å]	$\bar{c}$ [Å]	σ [Å]
O_2	3.448	3.480	3.458	0.009
O_2/O_3	3.620	3.767	3.668	0.036

Table 6.1: Range of the c-axis measured for 24 samples deposited in O_2 and 23 samples in the O_2/O_3 mixture. The mean c-axis ($\bar{c}$) and the standard deviation (σ) are also indicated.

of the c-axis for layers deposited in nominally identical oxidising conditions, as shown in Table 6.1. Interestingly, the c-axis variation for samples deposited in O_2/O_3 is four times larger than for the ones grown in O_2, indicating that the former is more sensitive to the exact growth conditions. Moreover, we observed that O_2/O_3 samples with the lowest thickness have the largest lattice parameter, which decreases progressively with the number of unit cells as shown in Fig. 6.4. Such a relation between the c-axis value and the film thickness is independent of the mixture total pressure. The variation of the lattice parameter may indicate a higher oxygen content close to the interface with the substrate and a lower one close to the surface of the film. This explanation is in line with the observation that the 002 Bragg peak for samples deposited in O_2 is more symmetric than the one in the highly-oxidising conditions (see

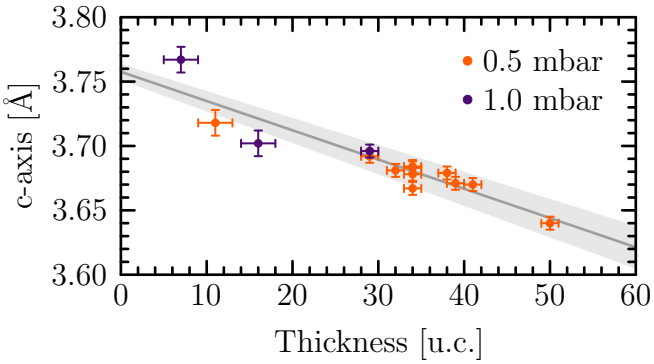

Figure 6.4: Out-of-plane lattice parameter as a function of the number of unit cells for samples grown in different highly-oxidising conditions. The solid line is a linear fit of the *c*-axis versus thickness while the shaded region shows the maximal standard deviation from the fit.

Fig. 6.3a).

To shed light on the origin of the high *c*-axis phase we used a scanning transmission electron microscope to perform measurements for both structures with the aim to be able to observe the additional oxygen atoms. The measurements were acquired by Bernat Mundet (University of Geneva) with an aberration corrected *Titan Themis* microscope, located at the École Polytechnique Fédérale de Lausanne (EPFL), operated at 300 kV with a current between 50 and 100 pA. A HAADF measurement, with a contrast essentially sensitive to the atomic number, is shown in Fig. 6.5a. In order to observe the oxygen atoms, which are too light to be resolved with HAADF, an ABF image was also acquired. The combination of these two images (coloured image) provides us an atomically resolved image that confirms the infinite-layer structure of the films deposited in pure oxygen. This is particularly clear when we extract line profiles along the Sr (purple) and the CuO_2 planes (orange); the latter shows additional intensity between the Cu atoms associated with the planar oxygen atoms.

Measurements of the high *c*-axis phase by means of STEM is more challenging. Exposing the lamella to the electron beam is detrimental to the $SrCuO_{2+\delta}$, as demonstrated by the surface degradation of the thin film after less than two minutes of beam exposure (Fig. 6.5b). This high sensitivity was reported in [213, 214] and was indicated as a key argument to confirm the incorporation of additional oxygen atoms in the Sr planes of the high *c*-axis phase. In the three HAADF images, the crystalline structure consisting of the Sr and Cu cations appears to be compatible with the infinite-layer structure, indicating that the insertion of oxygen in the Sr planes as the origin of the elongated phase is highly probable. Unfortunately, the continuous change of the sample structure under the electron beam did not allow us to perform detailed structural analysis to reveal the presence of additional oxygen atoms.

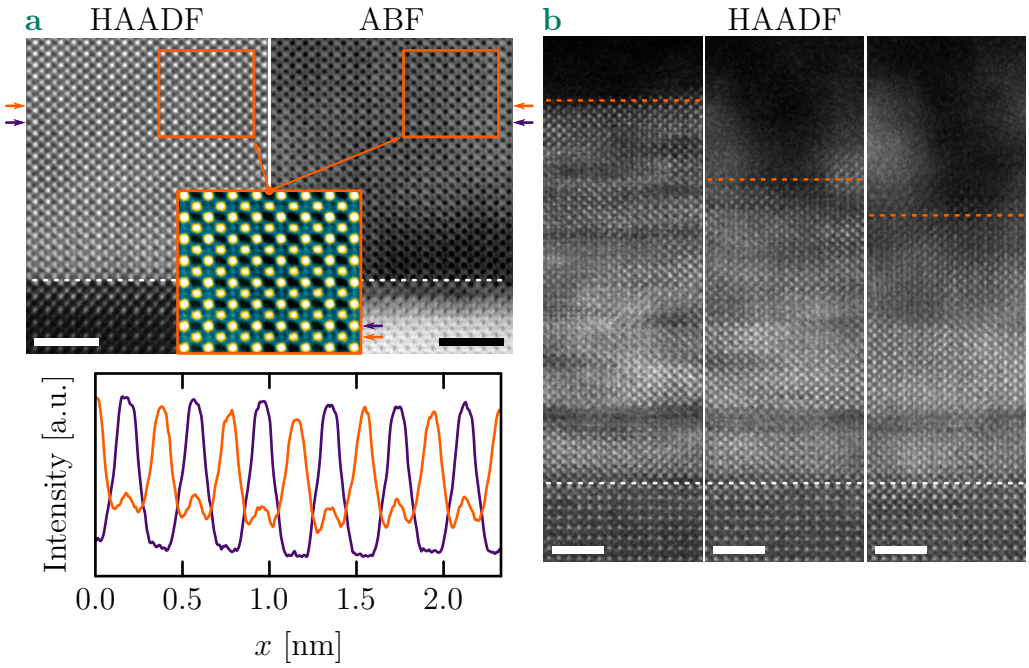

Figure 6.5: STEM measurements of the $SrCuO_2$ and $SrCuO_{2+\delta}$ thin films taken along the [100] zone axis. **a** Atomically resolved HAADF (left), ABF (right) images as well as coloured combination of the two (centre) of a sample grown in O_2. The purple and orange arrows indicate respectively the Sr and CuO_2 planes. Line profiles extracted from the combined image are shown in the bottom panel. **b** A series of HAADF images acquired consecutively in the same sample location, illustrating the surface degradation of a sample deposited in O_2/O_3 when exposed to the electron beam. The exposure time between the first and the last image is of the order of 2 minutes. The orange dashed line highlights the film surface. For both **a** and **b** the scale bar is 2 nm and the white dashed lines indicate the interface with the $SrTiO_3$ substrate.

To get more insight concerning the additional oxygen atoms, we acquired reciprocal space maps looking for signatures of a possible superstructure similar to the ones reported in [213, 214] (see Fig. 6.2). Although we found no evidence for such superstructures in our samples, it does not mean that they do not exist. A new in-plane periodicity (superstructure) originating from the oxygen sublattice should appear if the additional oxygen atoms order. However, it is also possible that the additional oxygen atoms do not exhibit any ordering. In this case, we would not expect to see any superstructure peaks.

With our instrument, we could not detect any superstructure peak; one possibility could be to grow thicker samples. However, if the additional oxygen atoms are located at the apical site but loosely ordered between the different alkaline planes, in-plane diffraction would be impossible because of the lack of coherence.

6.3 Temperature dependence of the *c*-axis

For many cuprates, the hole doping is controlled by the oxygen content of the sample: annealing between 200°C and 500°C in oxidising or reducing conditions indicate that oxygen is very mobile in these systems. Based on this consideration, and in order to confirm our hypothesis concerning the insertion of additional oxygen atoms in $SrCuO_{2+\delta}$, we performed XRD measurements while annealing a high *c*-axis sample in a N_2 gas flow. $\theta-2\theta$ scans were acquired at different temperatures between 25°C and 500°C using the high temperature domed hot stage DHS 900 from *Anton Paar*. These measurements are shown in Fig. 6.6.

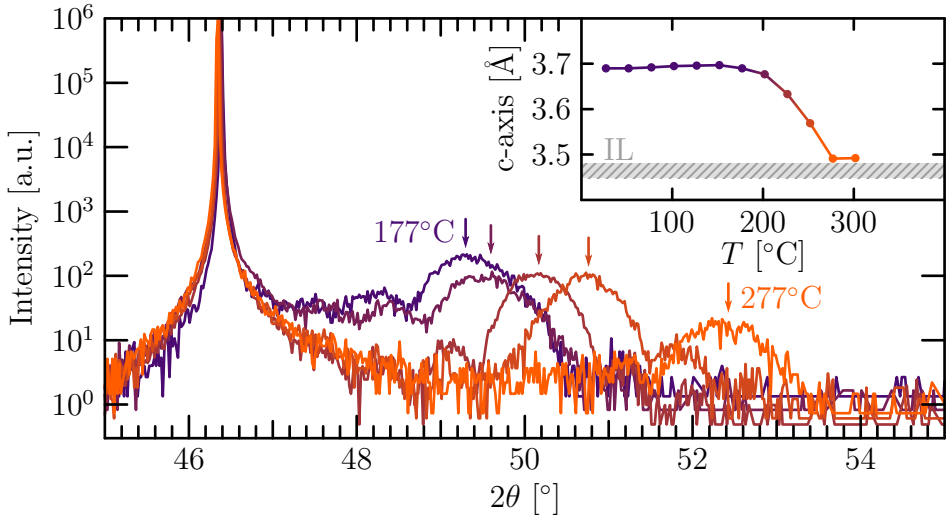

Figure 6.6: XRD measurements acquired on a high *c*-axis $SrCuO_{2+\delta}$ thin film at different temperatures. The temperature is stabilised every 25°C from room temperature up to 500°C. In the main panel are shown the $\theta-2\theta$ scans for 177°C, 202°C, 227°C, 252°C and 277°C (purple to orange). The arrows indicate the position of the $SrCuO_{2+\delta}$ 002 Bragg peak for each temperature. **Inset** $SrCuO_{2+\delta}$ *c*-axis as a function of annealing temperature between room temperature and ∼300°C, the temperature where we lose the peak signal. The grey hatched rectangle shows the range of *c*-axis values measured on various samples with infinite-layer structure ($SrCuO_2$).

Below 175°C the *c*-axis expands slightly, as shown in the inset of Fig. 6.6, without any dramatic change of the structural quality. At room temperature the *c*-axis is 3.690 Å, increasing to 3.697 Å at about 150°C. This increase is probably due to the thermal expansion of the thin film upon heating; the same effect is observed for $SrTiO_3$. At 175°C and above, we notice that the *c*-axis starts to decrease with increasing temperature, reaching 3.492 Å at 300°C. Above this temperature the $SrCuO_{2+\delta}$ 002 Bragg peak intensity is too low to be measured and cooling down the sample does not lead to any recovery of the

peak intensity, indicating that the film is destroyed.

This observation is compatible with a progressive reduction of the $SrCuO_{2+\delta}$ thin film, with δ going to zero as the temperature approaches 300°C. The *c*-axis value measured at 300°C (3.492 Å) is relatively close to the infinite-layer one, confirming that the effect of the high oxidising growth conditions is to incorporate additional oxygen atoms in the infinite-layer structure, leading to $SrCuO_{2+\delta}$ with $\delta > 0$. This conclusion excludes the other possible scenarios that explain the emergence of a high *c*-axis phase as a change or a rearrangement of the A-cations (Section 6.1.1).

Based on previous works [213–215, 236, 237], we can conclude that the oxygen atoms are located in the Sr planes, apically to the Cu atoms. Additionally, highly-oxidising conditions are required to stabilise the high *c*-axis phase, indicating that the additional apical oxygen atoms are probably less bonded than planar oxygen atoms. We can thus expect that they are easily removable upon heating in N_2, in agreement with the shift of the $SrCuO_{2+\delta}$ 002 peak in the $\theta - 2\theta$ scans. It is worth mentioning that the crystalline quality of the thin film is strongly degraded above 225°C, evidenced by the disappearance of the finite-size oscillations. This may be due to a progressive loss of structural coherence as the layer has to accommodate to the new stoichiometry.

6.4 Study of the high *c*-axis phase by X-ray absorption spectroscopy

6.4.1 X-ray absorption spectroscopy measurements

X-ray absorption spectroscopy measurements were performed on a $SrCuO_2$ sample (grown in pure oxygen) as well as on a high *c*-axis $SrCuO_{2+\delta}$ sample (deposited using the O_2/O_3 mixture) in order to compare their electronic properties. The data were acquired by Javier Herrero-Martín (ALBA Synchrotron Light Source, Spain), Gabriele De Luca (University of Zurich, Switzerland[1]) and Marta Gibert (University of Zurich, Switzerland[2]) at the HECTOR endstation of the BOREAS beamline at the ALBA synchrotron [238].

The spectra acquired for the present work were measured in total electron yield with a grazing angle (the angle between the X-ray beam direction and the sample surface) of $\alpha = 30°$, using both linear horizontal (LH) and linear vertical (LV) polarisations as illustrated in Fig. 6.7. The purely in-plane (I_{ab}) component, that is with the electric field (E) of the X-ray beam parallel to the sample surface and consequently to the crystallographic *ab* plane, is given by the LV signal. To extract the out-of-plane component (I_c), the LH signal has to be corrected due to the grazing angle α being non-zero. For an angle

[1]Now at the Catalan Institute of Nanoscience and Nanotechnology, Spain
[2]Now at the TU Wien, Austria

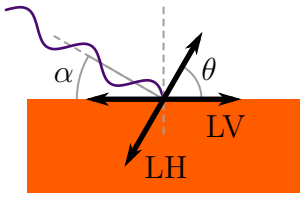

Figure 6.7: Scheme of the geometry used for the XAS measurements. The black arrows represent the electric field direction of the linear vertical (LV) and linear horizontal (LH) polarisations. The grazing angle (α) as well as the the angle between the LH electric-field and the sample surface (θ) are also shown.

θ ($\theta = 90° - \alpha$) between the sample surface and the X-ray electric field (see Fig. 6.7), the measured absorption is given by [239, 240]:

$$I(\theta) = I_{ab} \cdot \cos^2(\theta) + I_c \cdot \sin^2(\theta). \tag{6.1}$$

It is therefore possible to calculate the in-plane and out-of-plane components of the absorption spectra:

$$I_{ab} = I(0°) \qquad I_c = \frac{I(\theta) - I(0°) \cdot \cos^2(\theta)}{\sin^2(\theta)}. \tag{6.2}$$

With $I(0°) = I_{\mathrm{LV}}$ and $I(\theta) = I_{\mathrm{LH}}$. The XAS curves are obtained as the sum of spectra measured with in-plane and out-of-plane linear polarisation, while the X-ray linear dichroism (XLD) is defined as their difference:

$$\mathrm{XAS} = \frac{I_{ab} + I_c}{2} \qquad \mathrm{XLD} = I_{ab} - I_c \tag{6.3}$$

The measurements were acquired at the Cu L-edge and O K-edge and all the spectra were normalised by removing a linear background fitted at low energy, below any pre-edge components.

Fig. 6.8a shows the XAS spectra for a sample grown in O_2 (top curve) measured at the Cu L-edge. Two main peaks are observed due to spin-orbit coupling that splits the $2p$ degenerated core levels in two non-degenerated levels with different total angular momenta $j = l \pm \frac{1}{2}$, where l is the orbital angular momentum. The two peaks are labelled L_3 for $2p_{3/2}$ (at 932.5 eV) and L_2 for $2p_{1/2}$ (at 949.4 eV). Both originate from the transition of an electron from the Cu $2p$ core level to the first Cu $3d$ empty state, written as the $\underline{2p}3d^{10}$ final configuration (where the underline designates a hole in the $2p$ orbitals) [240–247]. These peaks are associated with Cu in the formally Cu^{2+} valence state.

For the sample deposited under highly-oxidising conditions (O_2/O_3), it can be observed in the bottom curve of Fig. 6.8a that the XAS spectra contains an additional component emerging as a high energy shoulder (933.5 eV and

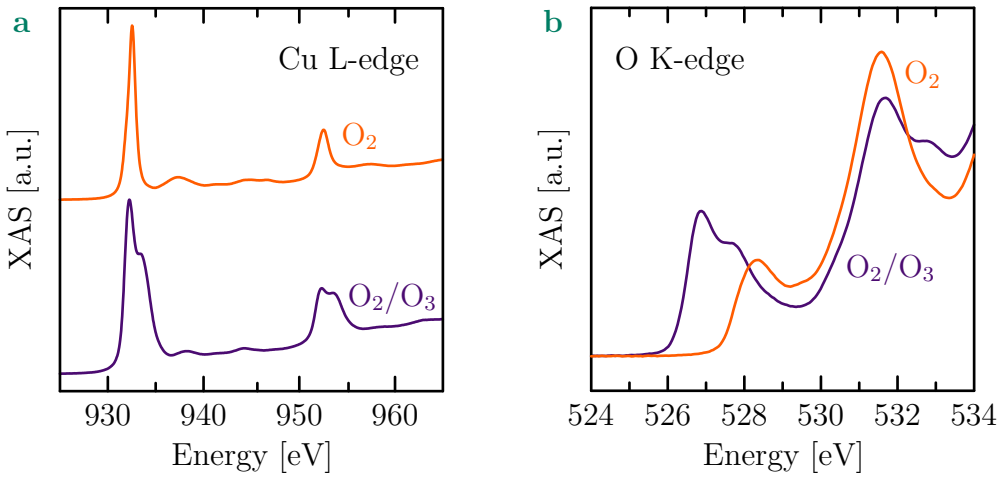

Figure 6.8: XAS measurements as defined by Eq. 6.3 at the Cu L-edge (**a**) and the O K-edge (**b**) for a $SrCuO_2$ thin film on $SrTiO_3$, deposited in pure oxygen (orange curve) and a $SrCuO_{2+\delta}$ on $SrTiO_3$ deposited in O_2/O_3 (purple curve).

953.6 eV) of the Cu^{2+} peaks (932.2 eV and 952.2 eV). This contribution comes from Cu^{3+} as observed in the trivalent Cu in the $NaCuO_2$ compound[3] [241].

Interestingly, a similar high energy shoulder appears for several cuprate compounds upon hole doping for which the holes are transferred to the ligand oxygen (L) [43, 240–249]. The electronic transition producing this shoulder can be written as $2p3d^9\underline{L} \rightarrow \underline{2p}3d^{10}\underline{L}$ (where $\underline{L}$ means ligand hole). The change in the formal valence state of copper strongly supports the presence of additional oxygen atoms in the high *c*-axis phase, leading to hole doping; more details are given in Section 6.4.2.

It is worth noting that these results rule out the possible chain type structure, discussed in Section 6.1.1, as the origin of the high *c*-axis phase. Indeed, in Reference [208], the authors do not observe additional signals to the Cu^{2+} spectra for the chain type structure.

In Fig. 6.8b the O K-edge for the sample deposited in O_2 (orange curve) can be observed. Our data are in good agreement with previous O K-edge measurements in the $Ca_{1-x}Sr_xCuO_2$ infinite-layer compound [242]. The first pre-edge peak around 528.3 eV is usually associated with the electronic transition into a O $2p$ state hybridised with the Cu $3d$; these states form the upper Hubbard band (UHB) [242, 245, 247, 250, 251]. The infinite-layer structure contains only oxygen in the CuO_2 plane: the spectral weight above 530 eV can therefore be assigned to the hybridisation of oxygen with unoccupied states of Sr and Cu located at higher energies.

The O K-edge lineshape for the sample deposited in O_2/O_3 shows multiple additional components (526.8 eV, 527.6 eV and 532.8 eV) that could indicate

[3]The Cu^{3+} notation is used for simplicity, but Cu is not in a $3d^8$ configuration as a hole is transferred to the ligand oxygen leading to the $3d^9\underline{L}$ state.

multiple non-equivalent oxygen sites [243, 251] in agreement with a $SrCuO_{2+\delta}$ oxygen rich phase. Moreover, the appearance of low energy features in combination with the reduction (disappearance) of the UHB peak is a well known effect emerging from hole doping. New states indeed become available in the valence band due to the hybridisation of the Cu $3d_{x^2-y^2}$ with the ligand hole in the O $2p_{x,y}$, a state that is called the Zhang-Rice singlet (ZRS) [245–247, 252, 253], leading to a redistribution of the spectral weight between the UHB to the low energy features.

Information concerning the symmetry of the unoccupied orbitals can be obtained by analysing the polarisation dependence of the XAS measurements, plotted in Fig. 6.9. For the Cu L-edge two types of transitions are allowed due

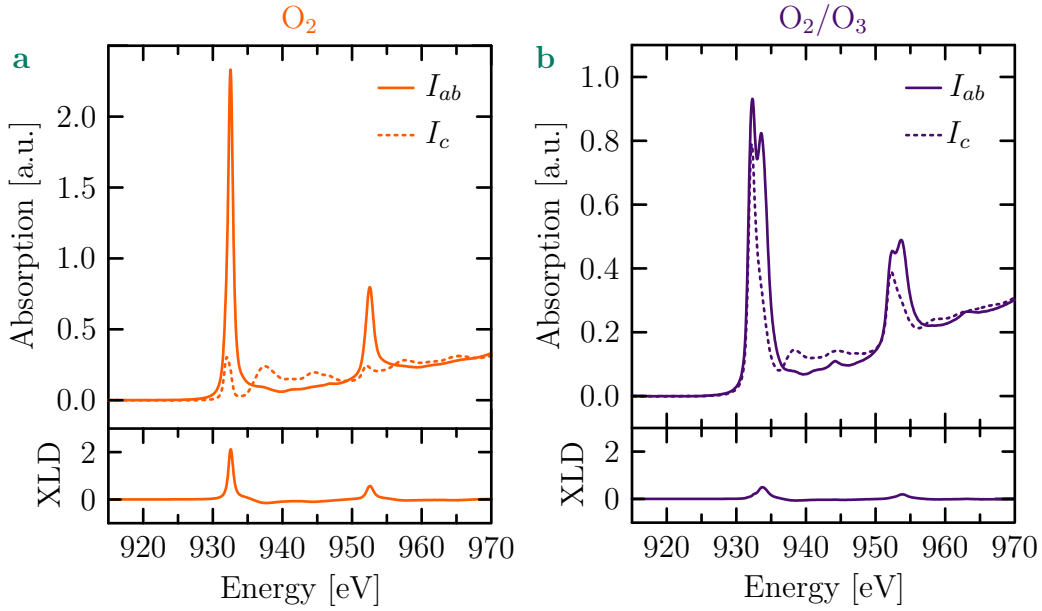

Figure 6.9: Absorption measured at the Cu L-edge for two different polarisations: in-plane (I_{ab}) and out-of-plane (I_c). Panel **a** shows the results for the infinite-layer sample and **b** for the oxygen rich sample. In both cases the XLD (defined in Eq. 6.3) are shown in the bottom panels using the same vertical scale.

to selection rules: between the $2p_{x,y}$ to the unoccupied $3d_{x^2-y^2}$ for $E \parallel ab$ or between the $2p_z$ orbitals to the $3d_{3z^2-r^2}$ for $E \parallel c$ [242]. Usually, in undoped cuprates (electronic configuration $3d^9$ for Cu^{2+}), the empty state (i.e. the single hole) lies in the $3d_{x^2-y^2}$ orbital. Our spectra, plotted in Fig. 6.9a, indeed show a strongly reduced signal for I_c as compared to I_{ab} for $SrCuO_2$, in excellent agreement with previous reports on infinite-layer compounds [208, 240, 242] and other cuprates [239, 242, 245, 252]. This is confirmed by measurements in normal incidence (data not shown) that reveal identical absorption for both LV and LH, reflecting the $3d_{x^2-y^2}$ symmetry of the unoccupied in-plane orbitals.

For the oxygen rich sample (Fig. 6.9b) a reduction of the anisotropy between the two polarisations is observed, especially for the Cu^{2+} features. Considering the small XLD signal around 932.2 eV shown in the bottom panels of Fig. 6.9b, it can be inferred that the environment of Cu is more isotropic, which is the case in the presence of apical oxygen atoms. A reduced anisotropy of the Cu L_3-edge has previously been observed for $BaCuO_{2+\delta}$ containing oxygen atoms in the Ba plane [240]; such comparison strongly suggests that in $SrCuO_{2+\delta}$ additional oxygen atoms lie in the Sr planes, apical to Cu.

The experimental evidence from the X-ray absorption spectroscopy data show the emergence of new spectral features associated with hole doping. Additionally, X-ray linear dichroism reveals a reduced anisotropy, suggesting that the origin of the elongated phase in $SrCuO_{2+\delta}$ is indeed due to additional oxygen atoms, inserted in the Sr planes.

6.4.2 Estimation of the doping

Various works [240, 244, 253–256] have shown that XAS measurements at the Cu L_3-edge can be used to get an estimation of the mean hole doping (p), from the ratio:

$$p = \frac{I(Cu^{3+})}{I(Cu^{2+}) + I(Cu^{3+})} \tag{6.4}$$

with $I(Cu^{2+})$ and $I(Cu^{3+})$ the areas of the peaks centred at 932.2 eV and 933.5 eV respectively.

The two peaks of the XAS Cu L_3-edge are fitted with two Voigt functions and a linear background using the Multipeak Fitting package included in the *Igor Pro 9.0* software; the result of the fitting is shown in Fig. 6.10a. It can be observed that the high energy peak is broader (FWHM∼2 eV) than the one centred at 932.2 eV (FWHM∼1 eV) as previously reported [241, 245]. From the fitting, we can estimate the mean number of holes in $SrCuO_{2+\delta}$ to be roughly $p \simeq 0.68 \pm 0.05$ holes/Cu. The error was estimated by using different backgrounds and/or peak functions for the peak fitting; the main source of error originates from the background subtraction [244]. This result suggests that $SrCuO_{2+\delta}$ is in the highly-overdoped regime (see Fig. 2.1b).

As discussed in Section 6.1.2, and considering that all the holes originate from the additional oxygen in $SrCuO_{2+\delta}$ the oxygen excess is found to be $\delta = \frac{p}{2} \simeq 0.34 \pm 0.03$, which is higher than our rough estimation of $\delta \sim 0.25$ discussed in the previous chapter (see Section 5.4). We can however refine the estimation of the doping from the lattice parameter value. In Fig. 6.10b the *ab-initio* calculated *c*-axis values (see Section 5.4.1) are shown as a function of the doping (orange circles). From these calculations a linear relation is observed for $\delta < 0.3$ and, at higher oxygen content, the *c*-axis value saturates more or less strongly depending on the strain state. This implies that the *c*-axis can be used to estimate the oxygen content of $SrCuO_{2+\delta}$ only at lower

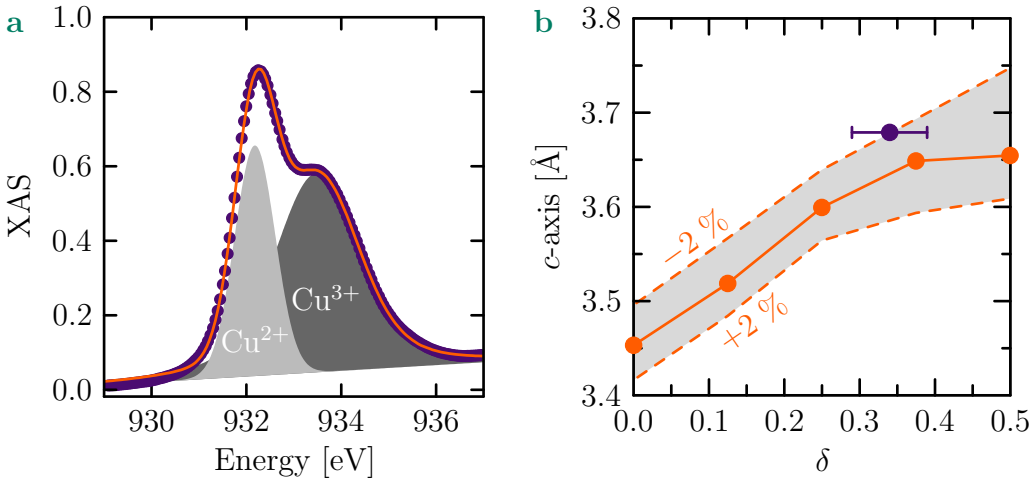

Figure 6.10: Estimation of the doping for the $SrCuO_{2+\delta}$ sample. **a** XAS spectra at the Cu L_3-edge (purple circles) shown with the result of the fitting (orange curve) composed of two Voigt peaks and a linear background. As detailed in the text, the peak centred at 932.2 eV is linked to a formally Cu^{2+} valence state while the one at 933.5 eV is the formally Cu^{3+} component (associated with a ligand hole in oxygen). **b** Value of the *c*-axis for $SrCuO_{2+\delta}$ as a function of δ. The orange circles are the data extracted from *ab-initio* calculations for the bulk system. The purple circle is the experimental result obtained from XAS (shown in **a**) and XRD. The bottom and top dashed lines show the *c*-axis values obtained by *ab-initio* calculations, considering tensile (+2 %) and compressive (−2 %) strain respectively.

doping ($\delta < 0.3$) and due to the saturation it is not reliable at higher oxygen content.

The experimental data (purple circle in Fig. 6.10b) show a relatively good agreement with the *ab-initio* calculations giving us some confidence in the validity of the doping estimation by XAS and confirming the particularly high doping in this system. Interestingly, such a high doping is not easy to obtain in other cuprates, making of $SrCuO_{2+\delta}$ a promising system for the study of the highly-overdoped regime.

6.5 Study of the high *c*-axis phase by X-ray photoemission spectroscopy

We performed preliminary measurements using XPS on $SrCuO_2$ and $SrCuO_{2+\delta}$ deposited in O_2 and O_2/O_3 respectively, to shed light on the valence and structural changes between the infinite-layer and the oxygen rich systems. The surface sensitivity as well as the ability to probe occupied states make XPS a complementary technique to other measurements, reported in the previous

sections (XRD, STEM and XAS). This study was done in strong collaboration with Siobhan Mckeown Walker, working at the Laboratoire de Technologie Avancée (LTA) in Geneva. High resolution XPS spectra were acquired for Sr 3*d*, O 1*s* and Cu 2*p* core levels and are shown in Fig. 6.11. The details

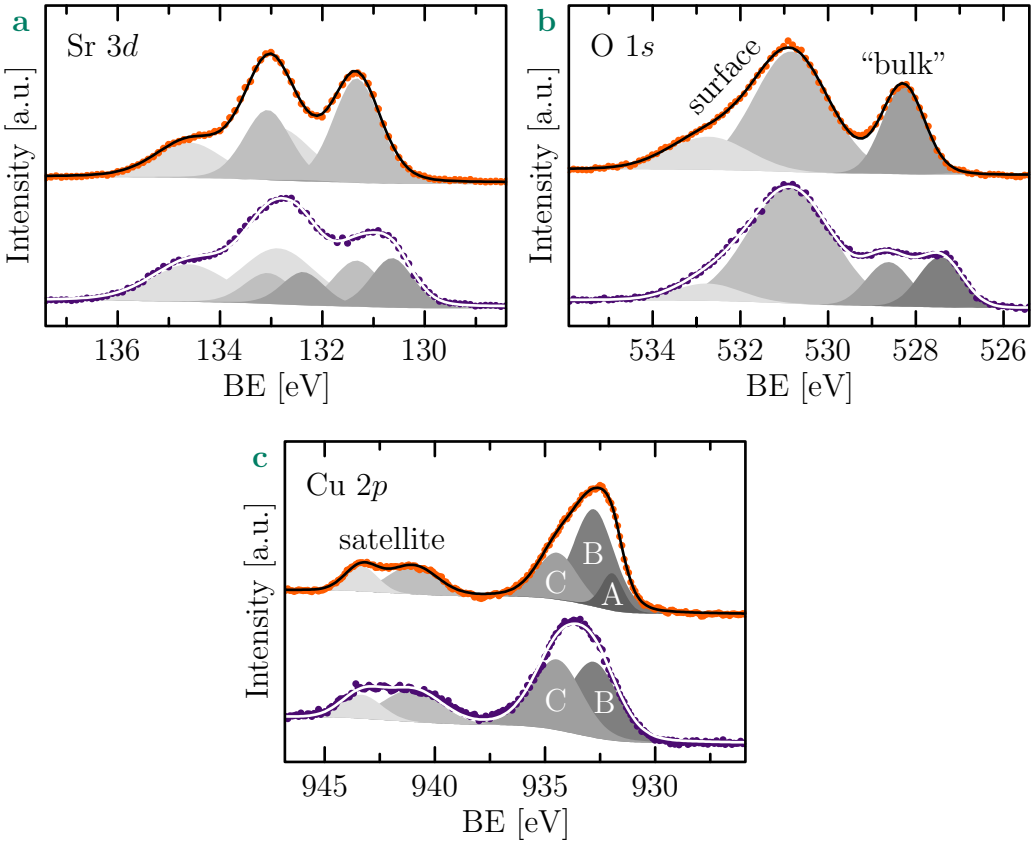

Figure 6.11: X-ray photoemission spectroscopy measurements of the Sr 3*d* (**a**), O 1*s* (**b**) and Cu 2*p* (**c**) core levels. The solid circles are the raw data for $SrCuO_2$ (orange) and $SrCuO_{2+\delta}$ (purple), the light-to-dark grey peaks show the different components used to fit (solid curve) the data.

concerning the data acquisition are presented in the Appendix D together with an analysis of the spectral features originating from the surface of the sample.

The Sr 3*d* spectra of the thin film deposited in O_2 can be fitted using only two doublets (at 134.7 eV and 133.1 eV) as shown in Fig. 6.11a. However, for the ozone deposited film an additional doublet (dark grey) at lower binding energy (132.4 eV) is required to fit the measured Sr 3*d* spectrum. This doublet has a FWHM comparable to the one of the bulk-like peak at 132.9 eV, and has a bulk-like character too. Interestingly, the need of an additional doublet has been already reported for Ca 2*p* at the $SrTiO_3/CaCuO_2$ interface, when apical oxygens are present [128]. In their case, the additional components emerge at

higher binding energies in contrast to what is observed in $SrCuO_{2+\delta}$. Although this difference is not yet fully understood, the need to use an additional doublet for $SrCuO_{2+\delta}$ could be compatible with a new environment for Sr in the structure, when additional oxygen atoms are inserted in the Sr planes. For example, this could be due to the existence of two non-equivalent Sr sites with different oxygen coordination.

The O 1*s* spectra for the oxygen grown sample, shown in Fig. 6.11b, are composed of two peaks: a broad peak at high binding energy (531 eV), that appears in both samples, has been assigned to the presence of a surface $SrCO_3$ layer (see Appendix D). The single and sharp component at 528.3 eV was assigned to the bulk of the film by our angular dependent measurements, and its energy is consistent with the intrinsic cuprate peaks in XPS studies on many other systems [257–262]. The single sharp peak for the sample deposited in O_2 is consistent with the infinite-layer structure, in which all the oxygen atoms are located in the CuO_2 planes and are therefore equivalent. Similarly to the observations in Sr 3*d*, the O 1*s* spectra from the $SrCuO_{2+\delta}$ sample reveal an additional sharp and bulk-like peak at lower binding energy. Interestingly, the spectrum cannot be fitted keeping a component at 528.3 eV, and the position of the two bulk-like peaks were left free in the fitting process, leading to one peak at 528.6 eV and another at 527.5 eV, separated by 1.1 eV. The presence of these two bulk-like components may indicate the presence of non-equivalent O-sites in $SrCuO_{2+\delta}$, which would be in line with the presence of additional oxygen in the Sr planes. This interpretation is supported by a comparison with other cuprates that have different non-equivalent O-sites and show multiple components for the O 1*s* core levels [259, 260, 262–264]. The general observation is that the shape, as well as the number of components making up the O 1*s* peak is strongly dependent on the oxygen arrangement in a given compound, but all the cuprate related O 1*s* peaks are separated in energy by at most 1.5 eV [259].

For the Cu-2*p* spectrum (Fig. 6.11c) two groups of peaks can be seen (see Appendix D). The satellite peaks, at high binding energies (938-946 eV), emerge from the poorly screened final state written as $\underline{2p}3d^9$. The main peak observed for $SrCuO_2$ (930-938 eV) can be fitted using three components, labelled as peaks A, B and C. From the literature [128, 259, 262, 265] we can associate each peak to a different screening mechanism of the Cu 2*p* core hole, as presented in Appendix D. These results confirms the hole doped nature of the $SrCuO_{2+\delta}$ thin film and suggest that the additional oxygen atoms occupy the apical sites. In addition to these screening effects, we can mention that more generally an increase of the hole doping leads to a more and more pronounced shoulder at high binding energy in various cuprate compounds [259, 260, 266–268]. The emergence of this shoulder (compatible with peak C in our $SrCuO_{2+\delta}$) has been observed independently of the specific structure of each compound and consequently independently on the Cu coordination, suggesting

that it can also be indicative of an increase of the oxidation state of Cu, toward a nominally Cu^{3+} valence state in agreement with the XAS data. This is in agreement with other data presented in the previous section of this chapter.

In order to confirm our results, other measurements will have to be performed, taking care to avoid exposing the sample surface to air to prevent surface contamination. Additionally, measuring $SrCuO_{2+\delta}$ at different oxygen content would allow us to follow the evolution of each peak to confirm their physical origin, for example by in-situ annealing in ultra-high vacuum.

6.6 Transport properties

From the previous sections we can conclude that the high *c*-axis phase originates from the insertion of additional oxygen atoms in the Sr planes, leading to the $SrCuO_{2+\delta}$ oxygen rich phase. Consequently, the additional oxygen atoms dope the system according to Section 6.4.2, and one should expect changes in the electrical transport properties. This is indeed what is observed: comparison of resistivity measurements shown in Fig. 6.12a, between undoped $SrCuO_2$ and doped $SrCuO_{2+\delta}$ samples, reveals a change of behaviour from insulating to weakly-insulating, with a room temperature resistivity two orders of magnitude lower. This is also evidenced by the value of the activation en-

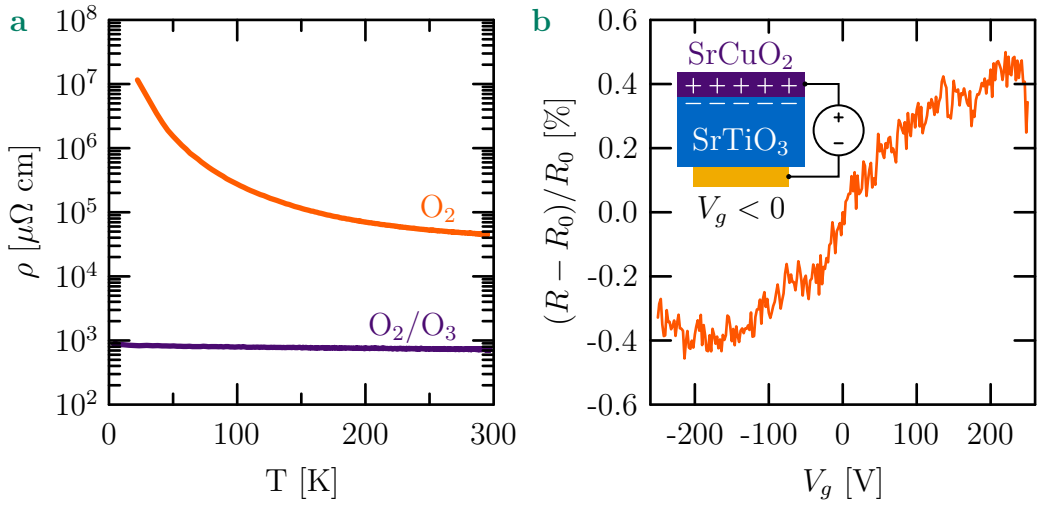

Figure 6.12: Electrical transport properties of the high *c*-axis $SrCuO_{2+\delta}$. **a** Resistivity as a function of temperature for an oxygen rich sample (purple) compared to an undoped infinite-layer sample (orange). **b** Normalised variation of the resistance as a function of the gate voltage for a pre-patterned $SrCuO_{2+\delta}$ thin film, measured at 1.7 K. The saturation observed at high back-gate voltages is due to leakage current through the $SrTiO_3$ substrate. The field-effect experiment was done using a back-gate geometry as schematically illustrated in the inset.

ergy (E_a) extracted by fitting a thermally activated transport above 200 K, as done in Section 4.3 for $SrTiO_3/CaCuO_2$ bilayers. For the undoped sample $E_a = 23.5$ meV while only 2.5 meV is found for the sample with the high *c*-axis. These transport measurements are in agreement with previous studies [213] and are compatible with the hole doping reported in the previous sections.

The sign of the carrier doping has been probed by back-gating field effect measurements presented in Fig. 6.12b. The normalised variation of the resistance $(R - R_0)/R_0$, with $R_0 = R(0\ V)$, is measured as a function of the back-gate voltage, at a temperature of 1.7 K. In our field-effect geometry, a negative gate voltage leads to electron depletion in the $SrCuO_{2+\delta}$ thin film, and consequently increases the hole concentration as illustrated by the inset in Fig. 6.12b. In contrast, $V_g > 0$ this leads to hole depletion. The electrostatic hole doping ($V_g < 0$) induces a reduction of the resistance of about 0.4% indicative of hole transport [173, 174, 176, 177]. While small, the variation of the resistance with the application of positive and negative gate voltages is reproducible upon sweeping the gate voltage multiple times. These transport measurements confirm the *p*-type character of electrical transport of the $SrCuO_{2+\delta}$ thin films, in agreement with the introduction of apical oxygen atoms in this system.

With the proper doping, and consequently the adapted oxygen content, the $SrCuO_{2+\delta}$ system could eventually turn superconducting, which, to our knowledge, has not been observed yet. It is worth mentioning that the absolute value of the resistivity at room temperature, around 1 mΩcm, is compatible with previous reports of superconductivity in many infinite-layer related heterostructures [119, 120, 269–271] and more generally with cuprates, which is strongly encouraging. An approach to search for superconductivity in the $SrCuO_{2+\delta}$ thin films is described in the following section.

6.7 Searching for superconductivity in $SrCuO_{2+\delta}$

The analysis presented so far indicates that the elongated phase of $SrCuO_{2+\delta}$ thin films is due to the insertion of apical oxygen which hole dopes the system, lowering its resistance. The control of the oxygen content during the growth seems difficult: as shown in Fig. 5.1, the change of the *c*-axis with increasing oxidising atmosphere is not continuous, but rather displays a sharp transition to the longer *c*-axis value. Considering the doping value extracted from the XAS measurements, $p = 0.68$ holes/Cu (i.e. $\delta = 0.34$), the $SrCuO_{2+\delta}$ samples are highly overdoped: in order to obtain superconductivity one would have to reduce the doping, i.e. the oxygen content. In the cuprates, the maximum T_c occurs at an optimal doping value of $p \sim 0.16$ holes/Cu. To achieve this

optimal doping in $SrCuO_{2+\delta}$, δ must be equal to 0.08, corresponding to a c-axis of about 3.5 Å, considering Fig. 6.10b.

Based on the results presented in Section 6.3 (Fig. 6.6), the reduction of the c-axis, and consequently the lowering of the doping, can be achieved through annealing of an oxygen rich sample in a reducing atmosphere. This idea is further motivated by the fact that we generally tend to observe a less insulating behaviour for samples with a shorter c-axis. This is evidenced in the inset of Fig. 6.13 by the slope (s) of the normalised resistivity at high temperature[4] for five $SrCuO_{2+\delta}$ samples with different c-axis values. It is worth noting that they

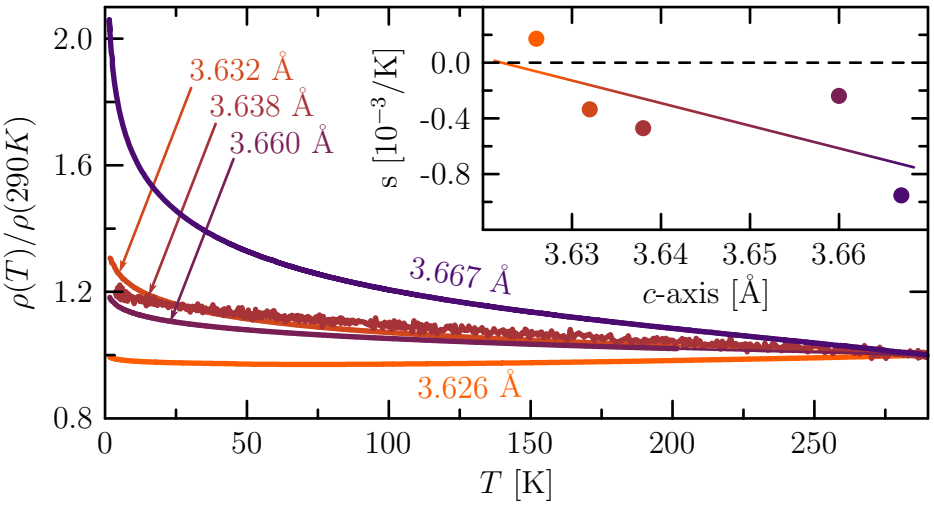

Figure 6.13: Electrical transport behaviour for samples with different out-of-plane c-axis values. The normalised resistance as a function of temperature is shown in the main panel for different c-axis (indicated in the figure for each curve). The inset shows s (the slope of the normalised resistance between 290 K and 150 K) as a function of the c-axis. Interestingly, the sample with the lowest c-axis (3.626 Å) shows a metallic behaviour ($s > 0$) above 75 K (bottom curve).

should be regarded only as a general tendency because some exceptions have been observed. Additionally, the crystalline quality is not the same for the five samples presented here and this can eventually lead to some discrepancies.

The exiting result is shown by the orange curve in Fig. 6.13, showing the normalised resistance of a sample with a particularly small c-axis (3.62 Å, see Table 6.1) and exhibiting a metallic behaviour, at least above 75 K. This result is particularly encouraging for the search of superconductivity in the $SrCuO_{2+\delta}$ system.

The semiconducting behaviour observed for these overdoped samples is somehow puzzling. In cuprates, overdoping usually leads to a metallic state

[4]We define the parameter s as the slope of $\frac{\rho(T)}{\rho(290\text{ K})}$ between 290 K and 150 K; it is extracted by fitting a linear curve over this range of temperatures. This parameter is used as a simple means of representing the "metallicity" of a sample.

with a Fermi liquid behaviour (see Section 2.1.3). This is not what is observed in our $SrCuO_{2+\delta}$ thin films and it can be surprising, but such a high doping ($p \geq 0.5$ holes/Cu) is difficult to achieve in other systems and therefore comparisons are rare. As an example, we can mention the $(La_{1-x}Sr_x)_2CuO_4$ system where in principle the La substitution should allow the study of the full doping range $0 \leq p \leq 2$ holes/Cu. The Cu valence would change from 2+ ($p = 0$) to 3+ ($p = 0.5$) and even 4+ ($p = 1$), which is not favourable for Cu: the system indeed prefers to change its oxygen stoichiometry as illustrated in early work observing that $x = 0.175$ ($p = 0.35$ holes/Cu) is the maximal doping reachable without changing the oxygen stoichiometry. At such doping, the $(La_{0.825}Sr_{0.175})_2CuO_4$ system is still metallic down to 5 K [272].

One should also mention that hole doped infinite-layer $Ca_{1-x}Li_xCuO_2$ ($0.15 \leq x \leq 0.45$) are neither superconducting nor metallic [273, 274]. Various mechanisms have been proposed to explain this behaviour: overdoping, non-localised holes in the CuO_2 planes or absence of apical oxygen [275].

Preliminary experiments of successive short annealings under vacuum (typically 30 minutes at 190°C) are promising: we observe a shrinking of the *c*-axis parameter and the $SrCuO_{2+\delta}$ crystalline quality remains higher than that for continuous annealing in N_2. Unfortunately, resistivity measurements revealed a strong anisotropic behaviour making the measurement not reliable and further reduction experiments have to be attempted.

Conclusions

Since the discovery of high temperature superconductivity in the cuprates, a large effort has been done in order to understand the pairing mechanism in these compounds as well as the different parameters influencing the critical temperature. For these purposes, the study of the infinite-layer cuprates ($ACuO_2$, with A = Ca, Sr and Ba) is relevant as they contain CuO_2 planes, key for superconductivity, while having a simpler structure than most of the cuprates. These compounds are undoped and consequently they display an insulating behaviour. One way to achieve hole doping is through interfacial effects. Insertion of additional oxygen atoms – using highly oxidising growth conditions – in $CaCuO_2$ at its interface with $SrTiO_3$ - was shown to lead to superconductivity in $SrTiO_3/CaCuO_2$ heterostructures.

In Chapter 4, the growth and optimisation of the $SrTiO_3/CaCuO_2$ bilayers deposited by PLD were presented, emphasising the effect of various growth parameters on the structural and electrical transport properties. Despite the difficulty to obtain reproducible growth conditions – in particular when ozone is used – metallic bilayers were obtained, a very encouraging result.

The next step for this project is to induce superconductivity at the interface between $CaCuO_2$ and $SrTiO_3$. One possible way is to increase the oxidising power of the growth atmosphere. Indeed, the samples grown in the present study were obtained using a gas mixture, during the thin film deposition, composed of 95% of O_2 and 5% of O_3 while superconducting $SrTiO_3/CaCuO_2$ heterostructures were reported to be obtained with 12% of O_3. The acquisition of a new ozone generator, with a tunable ozone concentration between 5% and 17%, will hopefully allow us to incorporate enough apical oxygen atoms at the $SrTiO_3/CaCuO_2$ interface to induce superconductivity. This is a necessary step in order to conduct the field-effect experiment proposed in this work. These experiments should allow us to control the position of the interfacial apical oxygen and its distance to the underneath Cu atom - distance that has been predicted to strongly influence the critical temperature: the further the apical oxygen the higher should be the critical temperature.

In Chapter 5 the oxygenation of the infinite-layer $CaCuO_{2+\delta}$ and $SrCuO_{2+\delta}$ was studied. The effect of different parameters such as the oxidising power during the deposition, the strain induced by the substrate onto the film and the size of the A-cation were considered. With the support of *ab-initio* calculations

and the empirical bond valence sum, we demonstrated the key role of the A-cation size for the incorporation of oxygen atoms in the structure of thin films deposited using highly oxidising atmosphere. The larger the A-cation, the easier the insertion of additional oxygen atoms in the structure, leading to an oxygen rich phase $ACuO_{2+\delta}$. Both experimental and theoretical results show that compressive strain favours the incorporation of oxygen atoms in the structure, while tensile strain stabilises the infinite-layer phase. However, the role of the strain is not critical compared to the A-cation size and the oxidising power which dominate for the possible stabilisation of the oxygen rich phase.

Recent theoretical calculations strongly suggest that the additional oxygen atoms prefer to be ordered, to form CuO_3 octahedra aligned along the out-of-plane direction. It would be interesting to see if we can experimentally observe this ordering, for example by measuring possible half order peaks using X-ray diffraction.

The high c-axis phase observed in $SrCuO_{2+\delta}$ when deposited under highly oxidising conditions originates from the insertion of additional oxygen atoms in the Sr planes, apical to Cu, as confirmed by various measurements such as XRD, XAS and XPS presented in Chapter 6. In particular, XAS measurements reveal a system that is strongly overdoped with a hole doping estimated to be of the order of $p \sim 0.68$ holes/Cu leading to an excess of oxygen $\delta \sim 0.34$ in good agreement with theoretical predictions from first-principle calculations. The annealing of $SrCuO_{2+\delta}$ thin films at low temperature ($< 250°C$) under reducing atmosphere (vacuum or N_2) allows the oxygen content and consequently the doping to be reduced, leading to a lowering of the c-axis. These results suggest that the c-axis value can be used to determine the doping level. Particularly promising for the search of superconductivity in these systems is the fact that a metallic behaviour was observed for $SrCuO_{2+\delta}$ thin films with a particularly low c-axis (lower doping).

To get more insights about this system one has to pursue and improve the reduction process in order to remove oxygen atoms without losing the crystalline quality. This seems to be a promising route to achieve superconductivity in $SrCuO_{2+\delta}$ films.

Appendix A

Ozone production

As presented in Section 3.1.2 two ozone generators were used in the present work. For both generators we performed measurements with a residual gas analyser (RGA) connected to the load-lock of our PLD system, in order to characterise them: in particular to estimate the ozone concentration.

Typical RGA spectra – partial pressure (p_m) as a function of the atomic mass (m) – are shown in Fig. A.1. For the estimation of the ozone concentra-

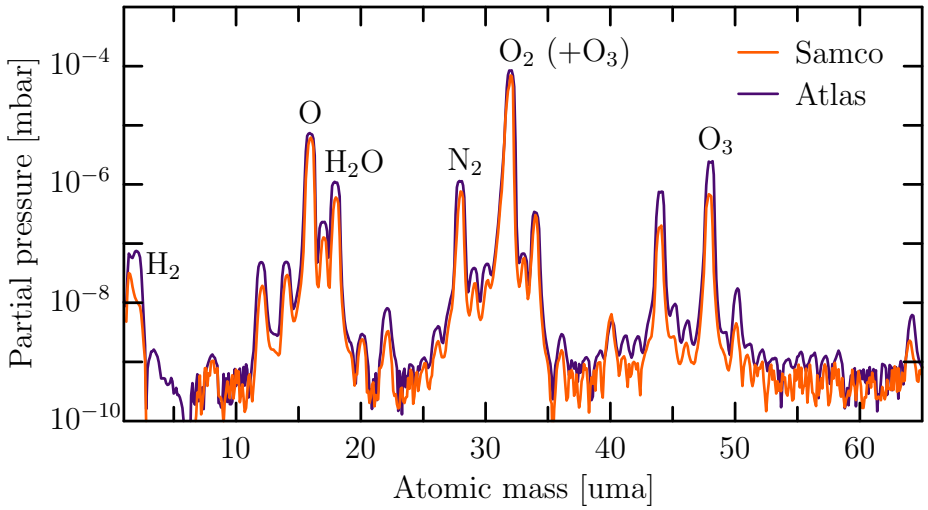

Figure A.1: Examples of residual gas analyser spectra for the two generators used in the present work. Purple and brown are with the generator turned on while the orange curve is for pure oxygen.

tion, the relevant partial pressure peaks are the ones centred at $m = 32$ uma and $m = 48$ uma associated with O_2 and O_3 respectively.

It is crucial to note that for ozone, the principal peak is not centred at $m = 48$ uma as one could think, but rather at $m = 32$ uma as for pure O_2 (Table A.1), which could make the estimation of the ozone concentration non-trivial [276].

	Relative intensity [%]	
***m* [uma]**	**O_2**	**O_3**
16	8.3	9.3
32	100	100
48	-	20

Table A.1: Relative intensities for O_2 ($p_m^{O_2}$) and O_3 ($p_m^{O_3}$), normalised to the peak centred at $m = 32$ uma, data from [276].

However, thanks to the fact that pure O_2 does not contribute to p_{48} ($p_{48}^{O_2} = 0$) it is possible to deduce the ozone contribution to the peak centred at $m = 32$ uma ($p_{32}^{O_3}$) by measuring p_{48}. Indeed, from Table A.1 one sees that $p_{48}^{O_3} = 20\% \cdot p_{32}^{O_3} \Rightarrow p_{32}^{O_3} = 5 \cdot p_{48}$ and the ozone concentration can be estimated from:

$$\frac{p_{32}^{O_3}}{p_{32}} = \frac{5 \cdot p_{48}}{p_{32}}. \tag{A.1}$$

Before having technical issues with the ozone generator from *Samco Inc*, it was producing a fixed percentage of ozone, estimated from the RGA measurement in Fig. A.1 (orange curve) to be 4.9%, in good agreement with the 5% indicated by the manufacturer.

For the Atlas UHC from *Oxidation Technologies, LLC* the percentage can be tuned by controlling the generator power. A RGA spectra is shown in Fig. A.1 (purple curve) revealing an ozone percentage of 14.5%. The dependence on the generator power is shown in Fig. A.2a confirming that the percentage of ozone can be tuned between 5% and almost 20%, slightly lower than the 22% indicated by the company.

It is worth noting that when dealing with ozone in our PLD there is a delay time between any action on the ozone generator and its effect in the growth chamber, for example when the generator is started, one has to count 2-3 minutes before observing a roughly stable ozone percentage. Moreover, as shown in Fig. A.2b when the generator is turned off (black arrow) it can take a few hours to remove the ozone from the chamber, while keeping the gas flow.

One has to keep in mind that these measurements were done in the load-lock of our system and the exact value could be a bit different, but it gives a general understanding of what is happening when ozone is used in our system.

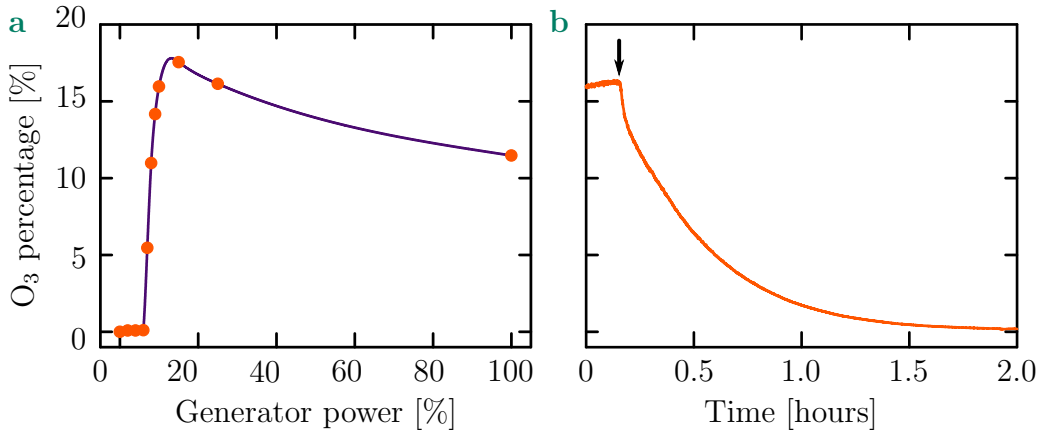

Figure A.2: Ozone percentage (using the Atlas UHC generator) in the deposition chamber of our PLD as a function of the generator power (**a**) and time (**b**). In panel **a** the purple line is a guide for the eyes and in panel **b** the black arrow indicates when the generator was powered off.

Appendix B

Atomic force microscopy: data treatment

The purpose of this Appendix is to describe the procedure used in order to extract useful information from atomic force microscopy. All the AFM data analysis are done with the software *Gwyddion* [277]. Generally, the raw data need some data treatment as shown in Fig. B.1a. The first step is to level

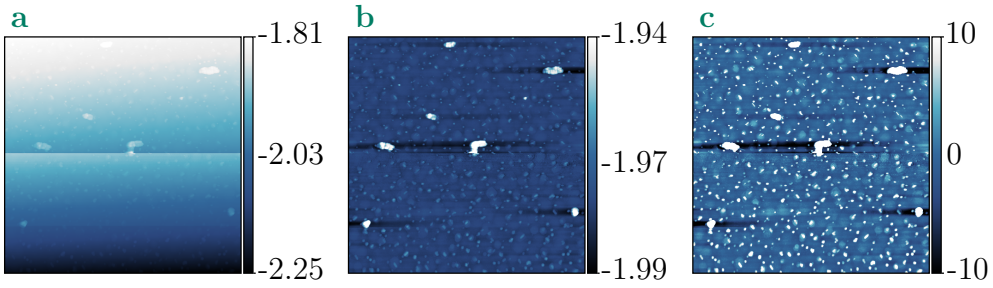

Figure B.1: AFM data treatment. **a** Raw data. **b** Data after the subtraction of a polynomial background. **c** Data after adjustment of the mean height to zero. The scanned region is 10 μm $\times$ 10 μm and the colour scales are in nanometres.

the data, indeed the measurement is done at the nanometre level thus any tilt of the sample will induce important changes in the topography. Moreover, if the tip is modified (e.g. picking up some dust) its interaction with the sample changes and the measurement change suddenly. This could be the reason of the sudden jump in the middle of the scan (Fig. B.1a). A more subtle effect (not seen here) which is generally visible for larger scans is a bowing of the data due to the way the piezoelectric element is controlling the tip height. In order to get rid of these artefacts each line of the scan is levelled by subtracting from it a polynomial background of degree 2, the resulting image is the Fig. B.1b. After this step the roughness can be extracted. *Gwyddion* is calculating the mean

roughness (ρ_{Mean}) and the root mean square roughness (ρ_{RSM}) as following :

$$\rho_{\text{Mean}} = \frac{1}{N}\sum_{n=1}^{N} \mid z_n - \overline{z} \mid \quad , \quad \rho_{\text{RMS}} = \sqrt{\frac{1}{N}\sum_{n=1}^{N}(z_n - \overline{z})^2} \tag{B.1}$$

Where N is the total number of points in the scan, z_n is each individual $z(x, y)$ and $\overline{z}$ the average tip height. The first one gives the average distance to mean value and the second one is the standard deviation of the height distribution. Because of the quadratic term, the latter is more sensitive to particles/holes that deviated significantly. For this reason, the mean roughness is mostly used in this work.

The last step of the data treatment is to bring the mean height to zero, this is simply to compare different scans with the same colorscale (Fig. B.1c).

Appendix C

Van der Pauw method

In 1958 L. J. van der Pauw proposed a new method to measure resistivity of lamella with an arbitrary shape [278, 279]. By the mean of two measurements (see Fig. C.1a):

1. R_{AB} (current from A to B and voltage between C and D)
2. R_{BC} (current from B to C and voltage between D and A)

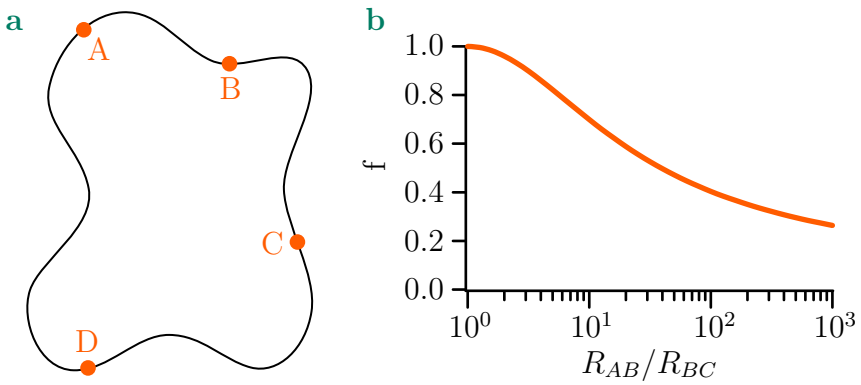

Figure C.1: **a** Sketch of a sample with an arbitrary shape illustrating the contacts order (A, B, C and D). **b** Solution of Eq. C.3 showing f as a function of the resistance ratio. Both adapted from [278].

It is possible to extract the resistivity by solving:

$$\exp\left(-\frac{\pi t}{\rho}R_{AB}\right) + \exp\left(-\frac{\pi t}{\rho}R_{BC}\right) = 1. \tag{C.1}$$

The solution of this equation is given by:

$$\frac{\rho}{t} = \frac{\pi}{\ln(2)}\frac{R_{AB}+R_{BC}}{2}f \tag{C.2}$$

with f illustrated in Fig. C.1b and given by:

$$\cosh\left(\frac{R_{AB}/R_{BC}-1}{R_{AB}/R_{BC}+1}\frac{\ln(2)}{f}\right)=\frac{1}{2}\exp\left(\frac{\ln(2)}{f}\right). \tag{C.3}$$

Basically, the resistivity is the average of the two resistances rescaled more or less, depending on the anisotropy, by a factor $\frac{\pi}{\ln(2)}f$. This is assuming that the contacts (A, B, C and D) are at the sample edges and are sufficiently small compared to the lamella. Moreover, calculations account for a homogenous thickness over the sample and finally the surface should not have isolated holes for Eq. C.1 to apply.

By abuse of language the term "van der Pauw measurement" is often used even if only one resistance is measured and then rescaled by $\pi/\ln(2)$. It is more a way to say how the resistance is measured and it generally gives a good approximation of the resistivity. Indeed the samples that are measured generally in Geneva have rarely $\frac{R_{AB}}{R_{BC}} > 5$, thus f is usually bigger than 0.8. Meaning that $R_{AB} \sim R_{BC}$ and consequently:

$$\frac{\rho}{t}=\frac{\pi}{\ln(2)}R_{AB}. \tag{C.4}$$

Appendix D

X-ray photoemission spectroscopy measurements

Details about the data acquisition

XPS data were acquired with a Versa Probe III system from *Physical Electronics* using a monochromated Al K_α source with a photon energy of 1486.6 eV. Energy scale linearity was calibrated with the Au $4f_{7/2}$ and Cu $2p_{3/2}$ peaks at 84.03 eV and 932.67 eV respectively. Samples were isolated from ground and an electron flood gun (1 V) as well as a low energy (10 V) Ar^+ bombardment were used to mitigate charging effects. Spectra shown in this study were measured with a Pass Energy of 55 eV and a 100 μm X-ray beam spot size on the sample. Samples were transferred through air and no measures were taken to remove the adventitious carbon layer. There was no evidence of Ti signal from the substrate, so it was assumed that there was no contribution to the Sr or O signal from the substrate. The energy scale was subsequently referenced to the Sr $3d_{5/2}$ peak of $SrCO_3$ at 132.9 eV. Fittings were performed in PHI MultiPack from *Physical Electronics* using mixed Gaussian-Lorentzian lineshapes and a Shirley background.

Surface contamination

Comparing data for the Sr-3*d* spectrum (not shown here) taken at different take-off angles – at 75°(more bulk sensitive) and at 45°(more surface sensitive) – we observed that the doublet at 134.7 eV (light-grey in Fig. 6.11a) has a higher intensity in the more surface sensitive geometry, indicating that it lies closer to the surface than the lower binding energy doublet (133.1 eV). We can consequently deduce that the associated Sr species originate from a surface layer and the doublet at lower energy, with sharper peaks, is more representative of the underlying $SrCuO_2$. The same was observed on $Bi_4(Sr,Ca)_6Cu_4O_{16+x}$

where this peak was associated with a $SrCO_3$ surface layer [257, 258]. This assignment is further confirmed by a peak at 288.4 eV in the C 1s spectra (not shown) and the peak at 531 eV in the O 1s spectrum (Fig. 6.11b) whose intensities show the same angular dependence, and whose binding energies are consistent with measurements on carbonates in the literature [257–259, 262]. Moreover, as shown in Table D.1, taken together, the peaks assigned to the presence of a surface layer correspond to a composition in reasonable agreement with the stoichiometry of $SrCO_3$. The remaining peaks are also roughly

	$SrCuO_2$		$SrCuO_{2+\delta}$	
	Sr:Cu:O	Sr:C:O	Sr:Cu:O	Sr:C:O
Experimental	32:23:45	13:22:65	25:26:49	16:14:70
(Expected)	(25:25:50)	(20:20:60)	(23:23:54)	(20:20:60)

Table D.1: Elemental composition for both $SrCuO_2$ and $SrCuO_{2+\delta}$ samples measured by XPS, given in percentage. The experimental values are extracted from the area of the different core level spectra of Sr, Cu, C and O, considering that the features, with higher intensity at 45°take-off angle, originate from carbonates on the sample surface. The expected values are expressed referring to the stoichiometric composition (assuming $\delta = 0.37$).

compatible with the expected stoichiometry for the $SrCuO_2$ film. The same argument can be used to deduce the presence of $SrCO_3$ on the surface of sample deposited in O_2/O_3, likely occurring because the films were stored in air prior the XPS measurements.

While the spectral feature around 531 eV in the O 1*s* spectra is considered to originate mostly from surface contamination in the cuprates [259, 262] reports on different compounds suggest that part of the intensity can be intrinsic to the bulk-like cuprates [258, 262]. This would potentially explain slight oxygen deficiency of the measured composition compared to the expected stoichiometry (see Table D.1). This example demonstrates the key role of the sample preparation in order to keep the surface as clean as possible, in order to assign a physical origin to each spectral feature in XPS. Note that for the sample deposited in the O_2/O_3 mixture, a higher oxygen content is observed (according to the measurement presented in Table D.1), which is in line with the insertion of extra oxygen atoms in this heterostructure and the XAS measurements presented in the previous section.

Core level analysis

O-1*s* In Reference [262], the authors associated the lowest energy peak in the O 1*s* spectra to the apical oxygen in $YBa_2Cu_3O_{6+\delta}$. This indicates that the peak at lower binding energy (527.5 eV) in Fig. 6.11b may also be related

to the oxygen in the Sr planes, which would be apical to Cu. However, as it can be noticed, the spectral weight of these two bulk-like peaks (527.59 eV and 528.6 eV) is really similar, which suggests that the assignment of this peak to the apical oxygen may not be correct, and the reality may be more complicated. Performing a systematic study at different oxygen contents, on an oxygen rich sample, would clarify the origin of this peak.

Cu-2*p* In contrast to the Sr 3*d* and O 1*s* peaks the relative intensity of the Cu 2*p* peak components does not show any angular dependence, indicating that the Cu 2*p* signal is probably intrinsic to the cuprate film. The Cu 2*p* spectra exhibit four peaks associated with $2p_{1/2}$ and $2p_{3/2}$ due to spin-orbit splitting and their respective satellites; only the Cu $2p_{3/2}$ are shown in Fig. 6.11c.

As mentioned in Section 6.5 the main peak observed for $SrCuO_2$ (930-938 eV) can be fitted using three components, labelled as peaks A, B and C. From the literature we can associate each peak to a different screening mechanism of the Cu 2*p* core hole, see for example [128, 259, 262, 265]. Considering first the undoped case where copper is expected to be formally divalent, peak C is generally assigned to a local screening of the Cu core hole, by a hole in the ligands of the surrounding oxygen sites, written as $\underline{2p}3d^{10}\underline{L}$. Peaks A and B are generally considered to be due to final states with more delocalised screening [251]. In particular peak A is assigned to non-local screening, written as $\underline{2p}3d^{10}$, where the hole from the core-hole site is pushed onto the ligand oxygen of the neighbouring CuO_4 plaquette ($3d^9\underline{L}$), creating a ZRS. Comparing the Cu 2*p* spectra of the infinite-layer and the oxygen rich phase in Fig. 6.11c the disappearance of peak A[1] can be observed as well as a clear increase of peak C compared to peak B. The reduction of peak A is consistent with the suppression of the ZRS non-local screening which is expected in a heavily hole-doped system where many ZRS already exist in the CuO_2 planes [265]. The suppression of this screening channel is expected to be compensated through local screening, which could account for the increase of peak C in the oxygen rich sample [265]. However, it is interesting to consider that the increase in peak C could be associated with an increased contribution from screening by out of plane orbitals, which was shown to make an important contribution to the line shape in systems with an apical oxygen [280]. In this case, the increase of peak C in the oxygen rich sample provides additional evidence that the additional oxygen atoms in $SrCuO_{2+\delta}$ occupy the apical site, while the suppression of peak A simultaneously suggests hole doping of the CuO_2 planes in the same sample.

[1]It is worth noting that the peak A has been reported to be difficult to observe using soft X-rays, probably explaining its low intensity in our measurements [128, 261].

Remerciements

Je dois le succès de mon doctorat à l'implication de plusieurs personnes que j'aimerais remercier chaleureusement, en essayant de n'oublier personne.

Tout d'abord un très grand merci à **Jean-Marc Triscone** sans qui rien de tout cela n'aurait été possible puisqu'il a accepté de m'accueillir dans son groupe pour y accomplir mon doctorat. Son enthousiasme pour la physique et tout le temps qu'il m'a consacré ont été et sont toujours une source d'encouragement.

Merci à **Stefano Gariglio** qui a co-supervisé ma thèse. J'ai beaucoup appris au travers de toutes nos discussions et ses conseils ont toujours été très appréciés, tout particulièrement pour la rédaction du présent manuscrit.

Je souhaite remercier **Christoph Renner**, **Daniele Di Castro** et **Jochen Mannhart** qui ont accepté de faire partie des membres du jury de ma thèse ; en particulier pour tout le temps qu'ils y ont consacré ainsi que pour leur présence lors de ma défense.

Au sein du groupe Triscone, j'aimerais remercier toute l'équipe LAO/STO dans laquelle j'ai débuté mon doctorat, tout spécialement **Danfeng Li** et **Margherita Boselli** aux côtés de qui j'ai appris tous les rudiments du travail dans les laboratoires. Leurs conseils et leur expérience ont été très enrichissants pour moi. Merci également à **Gernot Scheerer** et **Ritsuko Eguchi** qui ont rejoint l'équipe LAO/STO et avec qui j'ai eu de bonnes discussions.

Par la suite j'ai travaillé sur les cuprates "infinite-layer" où j'ai été rejoint par **Marios Hadjimichael** que j'aimerais remercier pour son infaillible soutien. Son investissement que ce soit pour les croissances, les mesures ou l'analyse des résultats, sa grande connaissance de la littérature ainsi que nos nombreuses discussions ont été très enrichissants pour moi et je lui en suis infiniment reconnaissant. Un grand merci à **Bernat Mundet** qui a mesuré nos échantillons par microscopie électronique en transmission à balayage ainsi qu'à **Clémentine Thibault** qui a rejoint ce projet tout récemment.

Je tiens à remercier tous les membres actuels et passés du groupe Triscone pour l'ambiance agréable qui règne au sein du groupe et pour toutes les discussions que nous avons eu ensemble. Merci à **Claribel Dominguez**, **Marta Gibert**, **Hugo Meley**, **Céline Lichtensteiger**, **Javier Del Valle**, **Lukas Korosec**, **Giacomo Mazza**, **Lucia Varbaro**, **Jennifer Fowlie**, **Stéphanie Fernandez**, **Willem Rischau**, **Christian Weymann**, **Sara Catalano**,

Elias Ferreiro, **Davide Valentinis** et **Ivan Rojkov**.

Un grand merci à **Marco Lopes** pour son soutien technique sans failles, qui effectue un travail impressionnant et a permis la réalisation de bien des projets ; sa disponibilité ainsi que ses nombreuses idées sont toujours les bienvenues.

J'aimerais encore remercier **Fabienne Hartmeier** et **Nathalie Chaduiron** pour leur aide administrative constante tout au long de ma thèse, sans qui les choses auraient été bien plus compliquées, en particulier pour les étapes finales ainsi que l'organisation de ma défense.

Je suis reconnaissant envers toute l'équipe administrative et technique avec qui j'ai eu la chance de travailler : **Heriberto Amores**, **Pierre Bouillot**, **Sandro D'Aleo**, **Marie-Anne Gervais**, **Elisabeth Giudicelli**, **Tony Gulizia**, **Grégory Manfrini**, **Sébastien Muller**, **Dragana Pantelic**, **Christophe Schwarz**, **Laurent Stark** et **Spiros Zanos**.

Le travail présenté dans cette thèse n'aurait pas été possible sans la collaboration avec de nombreuses personnes. Merci à **Jorge Cors** et **Jean-Claude Crost** pour la fabrication des masques par électroérosion, à **Daniele Di Castro** et **Giuseppe Balestrino** pour la fabrication d'échantillons supraconducteurs et leurs précieux conseils pour la croissance des films. Merci également à **Yajun Zhang** et **Philippe Ghosez** pour les calculs théoriques, à **Marta Gibert**, **Gabriele De Luca** et **Javier Herrero** pour les mesures spectroscopiques d'absorption des rayons X, et finalement à **Siobhan Mckeown** pour les mesures spectroscopiques de photoémission des rayons X ainsi que nos nombreuses discussions.

Au sein du département de la matière quantique j'aimerais encore remercier **Ivan Ardizzone**, **Christophe Berthod**, **Pablo Cayado**, **Alexandre Fête**, **Michele Filippone**, **Iaroslav Gaponenko**, **Enrico Giannini**, **Ignacio Gutierrez**, **Hugo Henck**, **Alexey Kuzmenko**, **Ivan Maggio-Aprile**, **Alberto Morpurgo**, **Carmine Senatore**, **Jérémie Teyssier**, **Philippe Tückmantel**, **Nicolas Ubrig** et **Yixi Zhou** ainsi qu'en dehors du département **Duncan Alexander**, **Andrea Caviglia**, **Marc Gabay**, **Alexandru Georgescu**, **Antoine Georges**, **Mark Huijben** et **Michel Viret** qui ont tous participé à la réussite de ma thèse d'une manière ou d'une autre.

Au cours de mon parcours j'ai eu le privilège de rejoindre l'équipe du Physiscope, animant des ateliers sur diverses thématiques de la physique pour les élèves du primaire et du secondaire afin d'éveiller leur curiosité scientifique. Un immense merci à toute l'équipe de direction et technique en particulier à **Olivier Gaumer**, **Céline Lichtensteiger**, **Céline Corthay** et **Miguel Iglesias**. J'ai énormément apprécié ces moments et j'ai beaucoup appris sur la communication scientifique.

Avant de terminer j'aimerais remercier toutes les personnes impliquées dans la relecture d'une partie ou de l'entièreté de ma thèse et pour leur retour qu'il soit scientifique ou linguistique. En plus des membres du jury un grand merci

à **Marios Hadjimichael**, **Céline Lichtensteiger**, **Siobhan Mckeown** et en particulier à **Audrey Puttemans** qui a pris le temps de tout relire malgré qu'elle ne soit pas du tout dans le domaine scientifique.

Pour terminer j'aimerais remercier ma famille qui m'a soutenu tout au long de mes études et qui ont pris le temps de venir assister à ma défense bien qu'ils ne parlent pas un mot d'anglais. Enfin, un immense merci à ma femme **Mirona** qui m'a épaulé et encouragé dès le début, sans elle à mes côtés cela n'aurait pas été pareil, merci.

Bibliography

[1] P. Zubko, S. Gariglio, M. Gabay, P. Ghosez, and J.-M. Triscone, Annual Review of Condensed Matter Physics **2**(1), 141 (2011).

[2] H. Y. Hwang, Y. Iwasa, M. Kawasaki, B. Keimer, N. Nagaosa, *et al.*, Nature Materials **11**(2), 103 (2012).

[3] A. Gozar, G. Logvenov, L. F. Kourkoutis, A. T. Bollinger, L. A. Giannuzzi, *et al.*, Nature **455**(7214), 782 (2008).

[4] V. Berezinskiĭ, Soviet Journal of Experimental and Theoretical Physics **34**(3), 610 (1972).

[5] J. M. Kosterlitz and D. J. Thouless, Journal of Physics C: Solid State Physics **6**(7), 1181 (1973).

[6] C. H. Ahn, J.-M. Triscone, and J. Mannhart, Nature **424**(6952), 1015 (2003).

[7] Y. Kozuka, M. Kim, C. Bell, B. G. Kim, Y. Hikita, *et al.*, Nature **462**(7272), 487 (2009).

[8] M. Basletic, J.-L. Maurice, C. Carrétéro, G. Herranz, O. Copie, *et al.*, Nature Materials **7**, 621 (2008).

[9] A. Ohtomo and H. Y. Hwang, Nature **427**, 423 (2004).

[10] N. Reyren, S. Thiel, A. D. Caviglia, L. F. Kourkoutis, G. Hammerl, *et al.*, Science **317**, 1196 (2007).

[11] A. D. Caviglia, S. Gariglio, N. Reyren, D. Jaccard, T. Schneider, *et al.*, Nature **456**, 624 (2008).

[12] A. D. Caviglia, M. Gabay, S. Gariglio, N. Reyren, C. Cancellieri, *et al.*, Physical Review Letters **104**, 126803 (2010).

[13] M. Ben Shalom, M. Sachs, D. Rakhmilevitch, A. Palevski, and Y. Dagan, Physical Review Letters **104**, 126802 (2010).

[14] A. Brinkman, M. Huijben, M. van Zalk, J. Huijben, U. Zeitler, *et al.*, Nature Materials **6**, 493 (2007).

[15] J. A. Bert, B. Kalisky, C. Bell, M. Kim, Y. Hikita, *et al.*, Nature Physics **7**, 767 (2011).

[16] N. Nakagawa, H. Y. Hwang, and D. A. Muller, Nature Materials **5**, 204 (2006).

[17] N. C. Bristowe, P. B. Littlewood, and E. Artacho, Physical Review B **83**, 205405 (2011).

[18] L. Yu and A. Zunger, Nature Communications **5**, 5118 (2014).

[19] P. Delugas, A. Filippetti, V. Fiorentini, D. I. Bilc, D. Fontaine, *et al.*, Physical Review Letters **106**, 166807 (2011).

[20] S. Gariglio, A. Fête, and J.-M. Triscone, Journal of Physics: Condensed Matter **27**, 283201 (2015).

[21] O. Copie, V. Garcia, C. Bödefeld, C. Carrétéro, M. Bibes, *et al.*, Physical Review Letters **102**, 216804 (2009).

[22] M. Sing, G. Berner, K. Goß, A. Müller, A. Ruff, *et al.*, Physical Review Letters **102**, 176805 (2009).

[23] A. D. Caviglia, S. Gariglio, C. Cancellieri, B. Sacépé, A. Fête, *et al.*, Physical Review Letters **105**, 236802 (2010).

[24] A. Dubroka, M. Rössle, K. W. Kim, V. K. Malik, L. Schultz, *et al.*, Physical Review Letters **104**, 156807 (2010).

[25] D. Li, S. Lemal, S. Gariglio, Z. Wu, A. Fête, *et al.*, Advanced Science **5**, 1800242 (2018).

[26] M. Salluzzo, J. C. Cezar, N. B. Brookes, V. Bisogni, G. M. De Luca, *et al.*, Physical Review Letters **102**, 166804 (2009).

[27] A. Joshua, S. Pecker, J. Ruhman, E. Altman, and S. Ilani, Nature Communications **3**, 1129 (2012).

[28] M. Stengel, Physical Review Letters **106**, 136803 (2011).

[29] J. Hemberger, P. Lunkenheimer, R. Viana, R. Böhmer, and A. Loidl, Physical Review B **52**(18), 13159 (1995).

[30] R. C. Neville, B. Hoeneisen, and C. A. Mead, Journal of Applied Physics **43**(5), 2124 (1972).

[31] C. Bell, S. Harashima, Y. Kozuka, M. Kim, B. G. Kim, *et al.*, Physical Review Letters **103**, 226802 (2009).

[32] W. Liu, S. Gariglio, A. Fête, D. Li, M. Boselli, *et al.*, APL Materials **3**, 062805 (2015).

[33] N. Reyren, S. Gariglio, A. D. Caviglia, D. Jaccard, T. Schneider, *et al.*, Applied Physics Letters **94**(11), 112506 (2009).

[34] J. M. Edge, Y. Kedem, U. Aschauer, N. A. Spaldin, and A. V. Balatsky, Physical Review Letters **115**(24), 247002 (2015).

[35] A. Stucky, G. W. Scheerer, Z. Ren, D. Jaccard, J.-M. Poumirol, *et al.*, Scientific Reports **6**(1), 37582 (2016).

[36] C. W. Rischau, X. Lin, C. P. Grams, D. Finck, S. Harms, *et al.*, Nature Physics **13**(7), 643 (2017).

[37] G. Scheerer, M. Boselli, D. Pulmannova, C. W. Rischau, A. Waelchli, *et al.*, Condensed Matter **5**(4), 60 (2020).

[38] S. Gariglio, M. Gabay, J. Mannhart, and J.-M. Triscone, Physica C: Superconductivity and its Applications **514**, 189 (2015).

[39] S. Gariglio, M. Gabay, and J.-M. Triscone, APL Materials **4**(6), 060701 (2016).

[40] Y.-Y. Pai, A. Tylan-Tyler, P. Irvin, and J. Levy, Reports on Progress in Physics **81**(3), 036503 (2018).

[41] S. Gariglio, A. D. Caviglia, J.-M. Triscone, and M. Gabay, Reports on Progress in Physics **82**(1), 012501 (2019).

[42] J. G. Bednorz and K. A. Müller, Zeitschrift für Physik B Condensed Matter **64**(2), 189 (1986).

[43] D. Di Castro, M. Salvato, A. Tebano, D. Innocenti, C. Aruta, *et al.*, Physical Review B **86**(13), 134524 (2012).

[44] D. Di Castro, C. Cantoni, F. Ridolfi, C. Aruta, A. Tebano, *et al.*, Physical Review Letters **115**(14), 147001 (2015).

[45] N. N. Greenwood and A. Earnshaw, "Copper, Silver and Gold", in *Chemistry of the Elements*, 2nd (Elsevier, 1997) Chap. 28, pp. 1173–1200.

[46] H. Onnes, Communications Leiden **124c**, 267 (1911).

[47] W. Meissner and R. Ochsenfeld, Die Naturwissenschaften **21**(44), 787 (1933).

[48] K. Kishio, K. Kitazawa, S. Kanbe, I. Yasuda, N. Sugii, *et al.*, Chemistry Letters **16**(2), 429 (1987).

[49] C. W. Chu, P. H. Hor, R. L. Meng, L. Gao, and Z. J. Huang, Science **235**(4788), 567 (1987).

[50] M. K. Wu, J. R. Ashburn, C. J. Torng, P. H. Hor, R. L. Meng, *et al.*, Physical Review Letters **58**(9), 908 (1987).

[51] H. Maeda, Y. Tanaka, M. Fukutomi, and T. Asano, Japanese Journal of Applied Physics **27**(Part 2, No. 2), L209 (1988).

[52] A. Schilling, M. Cantoni, J. D. Guo, and H. R. Ott, Nature **363**(6424), 56 (1993).

[53] L. Gao, Y. Y. Xue, F. Chen, Q. Xiong, R. L. Meng, *et al.*, Physical Review B **50**(6), 4260 (1994).

[54] A. V. Narlikar, "High-temperature cuprate superconductors", in *Superconductors*, 1st (Oxford University Press, 2014) Chap. 16, pp. 273–296.

[55] D. J. Rogers, P. Bove, and F. H. Teherani, Superconductor Science and Technology **12**(6), R75 (1999).

[56] S.-I. Uchida, *High Temperature Superconductivity*, Vol. 213, Springer Series in Materials Science (Springer Japan, Tokyo, 2015), p. 96.

[57] A. Iyo, Y. Tanaka, Y. Kodama, H. Kito, K. Tokiwa, *et al.*, Physica C: Superconductivity and its Applications **445-448**(1-2), 17 (2006).

[58] A. Mourachkine, *High-Temperature Superconductivity in Cuprates* (Springer, Dordrecht, 2002), p. 317.

[59] P. W. Anderson, Science **235**(4793), 1196 (1987).

[60] N. P. Armitage, P. Fournier, and R. L. Greene, Reviews of Modern Physics **82**(3), 2421 (2010).

[61] A. Damascelli, Z. Hussain, and Z.-X. Shen, Reviews of Modern Physics **75**(2), 473 (2003).

[62] Ø. Fischer, M. Kugler, I. Maggio-Aprile, C. Berthod, and C. Renner, Reviews of Modern Physics **79**(1), 353 (2007).

[63] R. Wesche, *Physical Properties of High-Temperature Superconductors*, Vol. 4, 1 (John Wiley & Sons, Ltd, Chichester, UK, 2015), p. 513.

[64] R. Wesche, "High-Temperature Superconductors", in *Springer Handbook of Electronic and Photonic Materials*, edited by S. Kasap and P. Capper (Springer International Publishing, Cham, 2017) Chap. 50, pp. 1225–1256.

[65] R. Hott and T. Wolf, "Cuprate High-Temperature Superconductors", in *digital Encyclopedia of Applied Physics*, Vol. 8 (Wiley-VCH Verlag GmbH & Co. KGaA, Weinheim, Germany, 2015), pp. 1–14.

[66] H. Kotegawa, Y. Tokunaga, K. Ishida, G.-q. Zheng, Y. Kitaoka, *et al.*, Journal of Physics and Chemistry of Solids **62**(1-2), 171 (2001).

[67] S. Ideta, K. Takashima, M. Hashimoto, T. Yoshida, A. Fujimori, *et al.*, Physical Review Letters **104**(22), 227001 (2010).

[68] J. M. Wheatley, T. C. Hsu, and P. W. Anderson, Nature **333**(6169), 121 (1988).

[69] P. W. Anderson, Science **268**(5214), 1154 (1995).

[70] S. Chakravarty, H.-Y. Kee, and K. Vølker, Nature **428**(6978), 53 (2004).

[71] Y. Hirata, K. M. Kojima, M. Ishikado, S. Uchida, A. Iyo, *et al.*, Physical Review B **85**(5), 054501 (2012).

[72] D. Di Castro and G. Balestrino, Superconductor Science and Technology **31**(7), 073001 (2018).

[73] H. Eisaki, N. Kaneko, D. L. Feng, A. Damascelli, P. K. Mang, *et al.*, Physical Review B **69**(6), 064512 (2004).

[74] H. Hobou, S. Ishida, K. Fujita, M. Ishikado, K. M. Kojima, *et al.*, Physical Review B **79**(6), 064507 (2009).

[75] Q. Q. Liu, H. Yang, X. M. Qin, Y. Yu, L. X. Yang, *et al.*, Physical Review B **74**(10), 100506 (2006).

[76] H. Matsukawa and H. Fukuyama, Journal of the Physical Society of Japan **59**(5), 1723 (1990).

[77] Y. M. Baikov and S. L. Shokhor, Physica C: Superconductivity and its applications **185-189**(PART 3), 1589 (1991).

[78] Y. Y. Peng, G. Dellea, M. Minola, M. Conni, A. Amorese, *et al.*, Nature Physics **13**(12), 1201 (2017).

[79] R. J. Cava, B. Batlogg, S. A. Sunshine, T. Siegrist, R. M. Fleming, *et al.*, Physica C: Superconductivity and its applications **153-155**(PART 1), 560 (1988).

[80] C. Murayama, N. Môri, S. Yomo, H. Takagi, S. Uchida, *et al.*, Nature **339**(6222), 293 (1989).

[81] E. Kaldis, P. Fischer, A. Hewat, E. Hewat, J. Karpinski, *et al.*, Physica C: Superconductivity **159**(5), 668 (1989).

[82] K. A. Müller, Zeitschrift für Physik B Condensed Matter **80**(2), 193 (1990).

[83] R. Griessen, Physical Review B **36**(10), 5284 (1987).

[84] B. A. Hunter, J. D. Jorgensen, J. L. Wagner, P. G. Radaelli, D. G. Hinks, *et al.*, Physica C: Superconductivity and its applications **221**(1-2), 1 (1994).

[85] N. Watanabe, K. Fukamachi, Y. Ueda, K. Tsushima, A. Balbashov, *et al.*, Physica C: Superconductivity **235-240**(PART 2), 1309 (1994).

[86] C. Meingast, A. Junod, and E. Walker, Physica C: Superconductivity **272**(1-2), 106 (1996).

[87] F. Hardy, N. J. Hillier, C. Meingast, D. Colson, Y. Li, *et al.*, Physical Review Letters **105**(16), 167002 (2010).

[88] J.-P. Locquet, J. Perret, J. Fompeyrine, E. Mächler, J. W. Seo, *et al.*, Nature **394**(6692), 453 (1998).

[89] R. J. Cava, A. Santoro, D. W. Johnson, and W. W. Rhodes, Physical Review B **35**(13), 6716 (1987).

[90] C. C. Torardi, M. A. Subramanian, J. C. Calabrese, J. Gopalakrishnan, E. M. McCarron, *et al.*, Physical Review B **38**(1), 225 (1988).

[91] Q. Huang, J. W. Lynn, Q. Xiong, and C. W. Chu, Physical Review B **52**(1), 462 (1995).

[92] C. Weber, C. Yee, K. Haule, and G. Kotliar, EPL (Europhysics Letters) **100**(3), 37001 (2012).

[93] Y. Ohta, T. Tohyama, and S. Maekawa, Physical Review B **43**(4), 2968 (1991).

[94] E. Pavarini, I. Dasgupta, T. Saha-Dasgupta, O. Jepsen, and O. K. Andersen, Physical Review Letters **87**(4), 047003 (2001).

[95] H. Sakakibara, H. Usui, K. Kuroki, R. Arita, and H. Aoki, Physical Review Letters **105**(5), 057003 (2010).

[96] H. Sakakibara, K. Suzuki, H. Usui, K. Kuroki, R. Arita, *et al.*, Physical Review B **86**(13), 134520 (2012).

[97] Z. Hiroi, M. Takano, M. Azuma, and Y. Takeda, Nature **364**(6435), 315 (1993).

[98] T. Siegrist, S. M. Zahurak, D. W. Murphy, and R. S. Roth, Nature **334**(6179), 231 (1988).

[99] R. D. Shannon, Acta Crystallographica Section A **32**(5), 751 (1976).

[100] R. Kipka and H. Müller-Buschbaum, Zeitschrift für Naturforschung B **32**(2), 121 (1977).

[101] L. Teske and H. Müller-Buschbaum, Zeitschrift für anorganische und allgemeine Chemie **379**(3), 234 (1971).

[102] M. Takano, Y. Takeda, H. Okada, M. Miyamoto, and T. Kusaka, Physica C: Superconductivity **159**(4), 375 (1989).

[103] N. Kobayashi, Z. Hiroi, and M. Takano, Journal of Solid State Chemistry **132**(2), 274 (1997).

[104] Z. Hiroi, M. Takano, M. Azuma, Y. Takeda, and Y. Bando, Physica C: Superconductivity and its applications **185-189**(PART 1), 523 (1991).

[105] G. Er, Y. Miyamoto, F. Kanamaru, and S. Kikkawa, Physica C: Superconductivity **181**(1-3), 206 (1991).

[106] M. Azuma, Z. Hiroi, M. Takano, Y. Bando, and Y. Takeda, Nature **356**(6372), 775 (1992).

[107] M. Takano, M. Azuma, Z. Hiroi, Y. Bando, and Y. Takeda, Physica C: Superconductivity **176**(4-6), 441 (1991).

[108] S. Adachi, H. Yamauchi, S. Tanaka, and N. Môri, Physica C: Superconductivity and its applications **208**(3-4), 226 (1993).

[109] P. Laffez, X. J. Wu, C. Q. Jin, S. Adachi, H. Yamauchi, *et al.*, Physica C: Superconductivity and its applications **233**(3-4), 373 (1994).

[110] X. Li, M. Kanai, T. Kawai, and S. Kawai, Japanese Journal of Applied Physics **31**(Part 2, No. 3A), L217 (1992).

[111] D. P. Norton, B. C. Chakoumakos, J. D. Budai, and D. H. Lowndes, Applied Physics Letters **62**(14), 1679 (1993).

[112] S. Takeno, S.-i. Nakamura, Y. Terashima, and T. Miura, Physica C: Superconductivity **206**(1-2), 75 (1993).

[113] E. Koller, L. Miéville, G. Triscone, J. Cors, J.-M. Triscone, *et al.*, Journal of Alloys and Compounds **195**(C), 303 (1993).

[114] Y. Terashima, R. Sato, S. Takeno, S.-i. Nakamura, and T. Miura, Japanese Journal of Applied Physics **32**(Part 2, No.1A/B), L48 (1993).

[115] A. Gupta, B. Hussey, T. Shaw, A. Guloy, M. Chern, *et al.*, Journal of Solid State Chemistry **112**(1), 113 (1994).

[116] M. G. Smith, A. Manthiram, J. Zhou, J. B. Goodenough, and J. T. Markert, Nature **351**(6327), 549 (1991).

[117] N. Ikeda, Z. Hiroi, M. Azuma, M. Takano, Y. Bando, *et al.*, Physica C: Superconductivity **210**(3-4), 367 (1993).

[118] S. Tao and H. U. Nissen, Physical Review B **51**(13), 8638 (1995).

[119] X. Li, T. Kawai, and S. Kawai, Japanese Journal of Applied Physics **33**(Part 2, No. 1A), L18 (1994).

[120] D. P. Norton, B. C. Chakoumakos, J. D. Budai, D. H. Lowndes, B. C. Sales, *et al.*, Science **265**(5181), 2074 (1994).

[121] S. Zhu, D. P. Norton, J. E. Chamberlain, F. Shahedipour, and H. W. White, Physical Review B **54**(1), 97 (1996).

[122] L. De Caro, C. Giannini, M. Nacucchi, L. Tapfer, G. Balestrino, *et al.*, Physical Review B **59**(21), 14074 (1999).

[123] G. Balestrino, S. Martellucci, P. Medaglia, A. Paoletti, and G. Petrocelli, Physica C: Superconductivity **302**(1), 78 (1998).

[124] G. Balestrino, S. Martellucci, P. G. Medaglia, A. Paoletti, G. Petrocelli, *et al.*, Physical Review B **58**(14), R8925 (1998).

[125] S. Colonna, F. Arciprete, A. Balzarotti, G. Balestrino, P. Medaglia, *et al.*, Physica C: Superconductivity **334**(1-2), 64 (2000).

[126] M. Salvato, I. Ottaviani, M. Lucci, M. Cirillo, D. Di Castro, *et al.*, Journal of Physics: Condensed Matter **25**(33), 335702 (2013).

[127] D. Di Castro, S. Caramazza, D. Innocenti, G. Balestrino, C. Marini, *et al.*, Applied Physics Letters **103**(19), 191903 (2013).

[128] C. Aruta, C. Schlueter, T.-L. Lee, D. Di Castro, D. Innocenti, *et al.*, Physical Review B **87**(15), 155145 (2013).

[129] M. Salvato, G. Tieri, G. Balestrino, and D. Di Castro, Superconductor Science and Technology **28**(9), 095012 (2015).

[130] F. Zarotti, D. Di Castro, R. Felici, and G. Balestrino, Physica B: Condensed Matter **539**(February), 123 (2018).

[131] D. Di Castro, C. Aruta, A. Tebano, D. Innocenti, M. Minola, *et al.*, Superconductor Science and Technology **27**(4), 044016 (2014).

[132] S. Amoruso, R. Bruzzese, N. Spinelli, and R. Velotta, Journal of Physics B: Atomic, Molecular and Optical Physics **32**(14), R131 (1999).

[133] R. Kelly and A. Miotello, "Mechanisms of Pulsed Laser Deposition", in *Pulsed Laser Deposition of Thin Films*, edited by B. Chrisey and G. K. Hubler (John Wiley & Sons, Inc., 1994) Chap. 3.

[134] D. B. Geohegan, "Diagnostics and Characteristics of Pulsed Laser Deposition Laser Plasma", in *Pulsed Laser Deposition of Thin Films*, edited by B. Chrisey and G. K. Hubler (John Wiley & Sons, Inc., 1994) Chap. 5.

[135] S. Amoruso, C. Aruta, R. Bruzzese, D. Maccariello, L. Maritato, *et al.*, Journal of Applied Physics **108**(4), 043302 (2010).

[136] S. Amoruso, B. Toftmann, J. Schou, R. Velotta, and X. Wang, Thin Solid Films **453-454**, 562 (2004).

[137] C. Aruta, S. Amoruso, R. Bruzzese, X. Wang, D. Maccariello, *et al.*, Applied Physics Letters **97**(25), 252105 (2010).

[138] S. Amoruso, C. Aruta, R. Bruzzese, X. Wang, and U. Scotti di Uccio, Applied Physics Letters **98**(10), 101501 (2011).

[139] R. Groenen, "Stoichiometry control in oxide thin films by pulsed laser deposition", (University of Twente, Enschede, The Netherlands, 2017).

[140] J. A. Venables, Surface Science **299-300**(11), 798 (1994).

[141] O. Kurtz, "Das Wachstum von Rhodium auf einer Graphit(0001)- und einer Rhenium(0001)-Oberfläche", (University of Berlin, Berlin, Germany, 1999).

[142] K. Oura, M. Katayama, A. V. Zotov, V. G. Lifshits, and A. A. Saranin, *Surface Science*, Advanced Texts in Physics (Springer Berlin Heidelberg, Berlin, Heidelberg, 2003).

[143] W. Kossel, Nachr. Ges. Wiss. Göttingen **1927**, 135 (1927).

[144] I. N. Stranski, Zeitschrift für Physikalische Chemie **136U**(1), 259 (1928).

[145] G. Ehrlich and F. G. Hudda, The Journal of Chemical Physics **44**(3), 1039 (1966).

[146] R. L. Schwoebel and E. J. Shipsey, Journal of Applied Physics **37**(10), 3682 (1966).

[147] R. L. Schwoebel, Journal of Applied Physics **40**(2), 614 (1969).

[148] H. Brune, "Growth Modes", in *Encyclopedia of Materials: Science and Technology*, Ml (Elsevier, 2001), pp. 3683–3692.

[149] G. S. Bales and D. C. Chrzan, Physical Review B **50**(9), 6057 (1994).

[150] G. Rosenfeld, B. Poelsema, and G. Comsa, "Epitaxial growth modes far from equilibrium", in *Growth and Properties of Ultrathin Epitaxial Layers*, Vol. 8, edited by D. A. King and D. P. Woodruff, C (Elsevier, 1997) Chap. 3, pp. 66–101.

[151] M. Horváth, L. Bilitzky, and J. Hüttner, *Ozone* (Elsevier, Budapest, 1985), p. 350.

[152] D. G. Schlom and J. S. Harris, "MBE Growth of High T_c Superconductors", in *Molecular Beam Epitaxy Application to Key Materials*, edited by R. F. Farrow (Noyes Publication, Mill Road, New Jersey, USA, 1995), pp. 505–622.

[153] D. Stornaiuolo, S. Gariglio, N. J. G. Couto, A. Fête, A. D. Caviglia, *et al.*, Applied Physics Letters **101**(22), 222601 (2012).

[154] V. E. Henrich, G. Dresselhaus, and H. J. Zeiger, Physical Review B **17**(12), 4908 (1978).

[155] N. Jalili and K. Laxminarayana, Mechatronics **14**(8), 907 (2004).

[156] B. Voigtländer, *Scanning Probe Microscopy*, NanoScience and Technology (Springer, Berlin, Heidelberg, 2015).

[157] C. Kittel, *Introduction to Solid State Physics*, 7th (John Wiley & Sons, Inc., 1996), p. 673.

[158] K. Momma and F. Izumi, Journal of Applied Crystallography **44**(6), 1272 (2011).

[159] C. Lichtensteiger, Journal of Applied Crystallography **51**(6), 1745 (2018).

[160] C. S. Schnohr and M. C. Ridgway, "Introduction to X-Ray Absorption Spectroscopy", in *X-Ray Absorption Spectroscopy of Semiconductors*, Vol. 190, edited by C. S. Schnohr and M. C. Ridgway, Springer Series in Optical Sciences (Springer Berlin Heidelberg, Berlin, Heidelberg, 2015), pp. 1–26.

[161] M. Blank, *Example XAS spectrum showing the three major data regions.* (Jan. 2010) https://en.wikipedia.org/w/index.php?title=File:XASFig.jpg.

[162] X. Sun and T.-K. Sham, "Group IV Nanowires", in *X-Ray Absorption Spectroscopy of Semiconductors*, Vol. 190, edited by C. S. Schnohr and M. C. Ridgway, Springer Series in Optical Sciences (Springer Berlin Heidelberg, Berlin, Heidelberg, 2015), pp. 223–246.

[163] E. E. Alp, S. M. Mini, and M. Ramanathan, *X-Ray Absorption Spectroscopy: EXAFS and XANES - A Versatile Tool to Study the Atomic and Electronic Structure of Materials*, tech. rep. (1990), pp. 25–36.

[164] J. F. Moulder, W. F. Stickle, P. E. Sobol, and K. D. Bomben, *Handbook of X-ray Photoelectron Spectroscopy*, edited by Jill Chastain (Perkin-Elmer Corporation, 1992), p. 261.

[165] C. Mariani and G. Stefani, "Photoemission Spectroscopy: Fundamental Aspects", in *Synchrotron Radiation*, Vol. 54, edited by S. Mobilio, F. Boscherini, and C. Meneghini, 5 (Springer Berlin Heidelberg, Berlin, Heidelberg, 2015), pp. 275–317.

[166] M. Schmal and C. A. C. Perez, "X-Ray Photoelectron Spectroscopy (ESCA: XPS/ISS)", in *Heterogeneous Catalysis and its Industrial Applications* (Springer International Publishing, Cham, 2016), pp. 251–266.

[167] S. Hüfner, *Photoelectron Spectroscopy*, Advanced Texts in Physics (Springer Berlin Heidelberg, Berlin, Heidelberg, 2003).

[168] D. J. Griffiths, *Introduction to Electrodynamics*, 3rd (Pearson Benjamin Cummings, 2008), p. 576.

[169] H. H. Barrett, Journal of Applied Physics **35**(5), 1420 (1964).

[170] H.-M. Christen, J. Mannhart, E. J. Williams, and C. Gerber, Physical Review B **49**(17), 12095 (1994).

[171] R. E. Glover and M. D. Sherrill, Physical Review Letters **5**(6), 248 (1960).

[172] A. Levy, J. P. Falck, M. A. Kastner, W. J. Gallagher, A. Gupta, *et al.*, Journal of Applied Physics **69**(8), 4439 (1991).

[173] J. Mannhart, D. Schlom, J. Bednorz, and K. Müller, Physical Review Letters **67**(15), 2099 (1991).

[174] T. Frey, J. Mannhart, J. G. Bednorz, and E. J. Williams, Physical Review B **51**(5), 3257 (1995).

[175] D. Matthey, N. Reyren, J.-M. Triscone, and T. Schneider, Physical Review Letters **98**(5), 057002 (2007).

[176] C. H. Ahn, J. .-. Triscone, N. Archibald, M. Decroux, R. H. Hammond, *et al.*, Science **269**(5222), 373 (1995).

[177] C. H. Ahn, L. Antognazza, T. Tybell, K. Char, M. Decroux, *et al.*, Journal of Low Temperature Physics **105**(5-6), 1517 (1996).

[178] C. H. Ahn, Science **284**(5417), 1152 (1999).

[179] J. Mannhart, Superconductor Science and Technology **9**(2), 49 (1996).

[180] N. Chandrasekhar, O. T. Valls, and A. M. Goldman, Physical Review Letters **71**(7), 1079 (1993).

[181] W. Kula and R. Sobolewski, Physical Review B **49**(9), 6428 (1994).

[182] W. Hu, S. Kaiser, D. Nicoletti, C. R. Hunt, I. Gierz, *et al.*, Nature Materials **13**(7), 705 (2014).

[183] G. Balestrino, R. Desfeux, S. Martellucci, A. Paoletti, G. Petrocelli, *et al.*, J. Mater. Chem. **5**(11), 1879 (1995).

[184] T. Ohnishi, K. Takahashi, M. Nakamura, M. Kawasaki, M. Yoshimoto, *et al.*, Applied Physics Letters **74**(17), 2531 (1999).

[185] D. Fuchs, P. Müller, A. Sleem, R. Schneider, D. Gerthsen, *et al.*, Journal of Applied Physics **112**(10), 103529 (2012).

[186] A. Cavallaro, G. F. Harrington, S. J. Skinner, and J. A. Kilner, Nanoscale **6**(13), 7263 (2014).

[187] J. Karpinski, K. Conder, H. Schwer, J. Löhle, L. Lesne, *et al.*, Journal of Superconductivity **8**(4), 515 (1995).

[188] B. Samia and S. Salima, Modelling, Measurement and Control B **87**(4), 230 (2018).

[189] P. F. Miceli and C. J. Palmstrom, Physical Review B **51**(8), 5506 (1995).

[190] V. M. Kaganer, R. Köhler, M. Schmidbauer, R. Opitz, and B. Jenichen, Physical Review B **55**(3), 1793 (1997).

[191] A. R. Wildes, R. A. Cowley, R. C. C. Ward, M. R. Wells, C. Jansen, *et al.*, Journal of Physics: Condensed Matter **10**(36), L631 (1998).

[192] S. Gariglio, N. Stucki, J.-M. Triscone, and G. Triscone, Applied Physics Letters **90**(20), 202905 (2007).

[193] D. D. Berkley, A. M. Goldman, B. R. Johnson, J. Morton, and T. Wang, Review of Scientific Instruments **60**(12), 3769 (1989).

[194] H. Appelboom, A. Fortuin, G. Rietveld, V. Matijasevic, P. Hadley, *et al.*, "In-situ growth of $YBa_2Cu_3O_y$ superconducting films by reactive coevaporation at low pressure using ozone", in *High T_c Superconductor Thin Films*, Vol. 89, 11 (Elsevier, 1992), pp. 383–388.

[195] N. Hayashi, T. Terashima, and M. Takano, Journal of Materials Chemistry **11**(9), 2235 (2001).

[196] H. P. Nair, Y. Liu, J. P. Ruf, N. J. Schreiber, S.-L. Shang, *et al.*, APL Materials **6**(4), 046101 (2018).

[197] H. Guo, D. Sun, W. Wang, Z. Gai, I. Kravchenko, *et al.*, Journal of Applied Physics **113**(23), 234301 (2013).

[198] J. V. Michael, The Journal of Chemical Physics **54**(10), 4455 (1971).

[199] T. Batakliev, V. Georgiev, M. Anachkov, S. Rakovsky, and S. Rakovsky, Interdisciplinary Toxicology **7**(2), 47 (2014).

[200] A. Sambri, C. Aruta, E. Di Gennaro, X. Wang, U. Scotti di Uccio, *et al.*, Journal of Applied Physics **119**(12), 125301 (2016).

[201] M. Döbeli, A. Wokaun, and T. Lippert, Journal of Applied Physics **124**(8), 085308 (2018).

[202] L. Vuitton, *Montre Tourbillon Volant "Poinçon de Genève"*, (July 2021) https://fr.louisvuitton.com/fra-fr/articles/tourbillon-volant.

[203] D. D. DiBitonto, P. T. Eubank, M. R. Patel, and M. A. Barrufet, Journal of Applied Physics **66**(9), 4095 (1989).

[204] TIMELAB - Fondation du laboratoire d'horlogerie et de microtechnique de Genève, *Poinçon de Genève*, (July 2021) https://www.poincondegeneve.ch.

[205] P. Rodrik, "Le Poinçon de Genève prend un coup de jeune et de modernité technologique", in *Tribune de Genève* (17 sept., Geneva, Switzerland, 2014), p. 12.

[206] Z. Liao, E. Skoropata, J. W. Freeland, E.-J. Guo, R. Desautels, *et al.*, Nature Communications **10**(1), 589 (2019).

[207] Z. Zhong, G. Koster, and P. J. Kelly, Physical Review B **85**(12), 121411 (2012).

[208] D. Samal, H. Tan, H. Molegraaf, B. Kuiper, W. Siemons, *et al.*, Physical Review Letters **111**(9), 096102 (2013).

[209] S. Li, Q. Zhang, S. Lin, X. Sang, R. F. Need, *et al.*, Advanced Materials **2001324**, 2001324 (2020).

[210] S. Lin, Q. Zhang, X. Sang, J. Zhao, S. Cheng, *et al.*, Nano Letters **21**(7), 3146 (2021).

[211] D. Samal and G. Koster, Journal of Materials Research **30**(4), 463 (2015).

[212] X. Zhou, C. Dong, F. Wu, H. Chen, G. Che, *et al.*, Journal of Solid State Chemistry **112**(1), 211 (1994).

[213] H. Yakabe, A. Kume, J. Wen, M. Kosuge, Y. Shiohara, *et al.*, Physica C: Superconductivity **232**(3-4), 371 (1994).

[214] J. Wen, H. Yakabe, A. Kume, Y. Shiohara, N. Koshizuka, *et al.*, Physica C: Superconductivity **228**(3-4), 279 (1994).

[215] A. Tsukamoto, J. Wen, K. Nakanishi, and K. Tanabe, Physica C: Superconductivity **292**(1-2), 17 (1997).

[216] D. Kan, A. Yamanaka, T. Terashima, and M. Takano, Physica C: Superconductivity **412-414**(SPEC. ISS.) 298 (2004).

[217] M. Crespin, P. Levitz, and L. Gatineau, J. Chem. Soc., Faraday Trans. 2 **79**(8), 1181 (1983).

[218] M. Kawai, S. Inoue, M. Mizumaki, N. Kawamura, N. Ichikawa, *et al.*, Applied Physics Letters **94**(8), 082102 (2009).

[219] Y. Tsujimoto, C. Tassel, N. Hayashi, T. Watanabe, H. Kageyama, *et al.*, Nature **450**(7172), 1062 (2007).

[220] S. Inoue, M. Kawai, Y. Shimakawa, M. Mizumaki, N. Kawamura, *et al.*, Applied Physics Letters **92**(16), 161911 (2008).

[221] H. Jeen, W. S. Choi, M. D. Biegalski, C. M. Folkman, I.-C. Tung, *et al.*, Nature Materials **12**(11), 1057 (2013).

[222] D. Kaneko, K. Yamagishi, A. Tsukada, T. Manabe, and M. Naito, Physica C: Superconductivity **469**(15-20), 936 (2009).

[223] M. Hayward and M. Rosseinsky, Solid State Sciences **5**(6), 839 (2003).

[224] I. D. Brown, Chem. Soc. Rev. **7**(3), 359 (1978).

[225] I. D. Brown and D. Altermatt, Acta Crystallographica Section B Structural Science **41**(4), 244 (1985).

[226] I. D. Brown, *Bond valence parameters*, (Dec. 2020) https://www.iucr.org/resources/data/data-sets/bond-valence-parameters.

[227] T. A. Yee, L. Suescun, and F. A. Rabuffetti, Journal of Solid State Chemistry **270**(August 2018), 242 (2019).

[228] W. Liu and H. H. Thorp, Inorganic Chemistry **32**(19), 4102 (1993).

[229] K. K. Wu and I. Brown, Materials Research Bulletin **8**(5), 593 (1973).

[230] S. Lemal, N. C. Bristowe, and P. Ghosez, Physical Review B **102**(11), 115309 (2020).

[231] M. Schmid, *Chemical Potential Calculator*, (Sept. 2020) https://www.iap.tuwien.ac.at/www/surface/chemical_potentials.

[232] K. Reuter and M. Scheffler, Physical Review B **65**(3), 035406 (2001).

[233] M. Takano, Journal of Superconductivity **7**(1), 49 (1994).

[234] H. Zhang, Y. Y. Wang, H. Zhang, V. P. Dravid, L. D. Marks, *et al.*, Nature **370**(6488), 352 (1994).

[235] H. Adachi, T. Satoh, Y. Ichikawa, K. Setsune, and K. Wasa, Physica C: Superconductivity **196**(1-2), 14 (1992).

[236] J.-Q. Fan, S.-Z. Wang, X.-Q. Yu, R.-F. Wang, Y.-L. Xiong, *et al.*, Physical Review B **101**(18), 180508 (2020).

[237] Y. Zhong, J.-Q. Fan, R.-F. Wang, S. Wang, X. Zhang, *et al.*, Physical Review Letters **125**(7), 077002 (2020).

[238] A. Barla, J. Nicolás, D. Cocco, S. M. Valvidares, J. Herrero-Martín, *et al.*, Journal of Synchrotron Radiation **23**(6), 1507 (2016).

[239] N. L. Saini, D. S. Law, P. Pudney, P. Srivastava, A. Menovsky, *et al.*, Physica C: Superconductivity and its applications **251**(1-2), 7 (1995).

[240] C. Aruta, G. Ghiringhelli, C. Dallera, F. Fracassi, P. G. Medaglia, *et al.*, Physical Review B **78**(20), 205120 (2008).

[241] D. D. Sarma, O. Strebel, C. T. Simmons, U. Neukirch, G. Kaindl, *et al.*, Physical Review B **37**(16), 9784 (1988).

[242] E. Pellegrin, N. Nücker, J. Fink, S. L. Molodtsov, A. Gutiérrez, *et al.*, Physical Review B **47**(6), 3354 (1993).

[243] J. M. Chen, R. S. Liu, and W. Y. Liang, Physical Review B **54**(17), 12587 (1996).

[244] P. Ghigna, G. Spinolo, G. Flor, and N. Morgante, Physical Review B **57**(21), 13426 (1998).

[245] M. Merz, N. Nücker, P. Schweiss, S. Schuppler, C. T. Chen, *et al.*, Physical Review Letters **80**(23), 5192 (1998).

[246] Z. Hu, S.-L. Drechsler, J. Málek, H. Rosner, R. Neudert, *et al.*, Europhysics Letters (EPL) **59**(1), 135 (2002).

[247] W. M. Li, J. F. Zhao, L. P. Cao, Z. Hu, Q. Z. Huang, *et al.*, Proceedings of the National Academy of Sciences **116**(25), 12156 (2019).

[248] D. Meyers, S. Mukherjee, J.-G. Cheng, S. Middey, J.-S. Zhou, *et al.*, Scientific Reports **3**(1), 1834 (2013).

[249] D. Choudhury, P. Rivero, D. Meyers, X. Liu, Y. Cao, *et al.*, Physical Review B **92**(20), 201108 (2015).

[250] H. Romberg, M. Alexander, N. Nücker, P. Adelmann, and J. Fink, Physical Review B **42**(13), 8768 (1990).

[251] M. S. Golden, C. Dürr, A. Koitzsch, S. Legner, Z. Hu, *et al.*, Journal of Electron Spectroscopy and Related Phenomena **117-118**, 203 (2001).

[252] C. T. Chen, L. H. Tjeng, J. Kwo, H. L. Kao, P. Rudolf, *et al.*, Physical Review Letters **68**(16), 2543 (1992).

[253] M. Karppinen, M. Kotiranta, T. Nakane, H. Yamauchi, S. C. Chang, *et al.*, Physical Review B **67**(13), 134522 (2003).

[254] N. Merrien, F. Studer, G. Poullain, C. Michel, A. M. Flank, *et al.*, Journal of Solid State Chemistry **105**(1), 112 (1993).

[255] Y. Tanaka, M. Karppinen, T. Kobayashi, T. S. Chan, R. S. Liu, *et al.*, Chemistry of Materials **20**(16), 5414 (2008).

[256] A. K. Ariffin, C. Janowitz, B. Müller, L. Dudy, P. Sippel, *et al.*, Journal of Physics: Conference Series **150**(5), 1 (2009).

[257] W. R. Flavell, J. A. Hampson, C. Neeson, and R. J. D. Tilley, Superconductor Science and Technology **1**(5), 221 (1989).

[258] D. A. Geeson, M. S. Golden, S. J. Golden, and W. R. Flavell, Superconductor Science and Technology **2**(5), 279 (1989).

[259] M. S. Golden, R. G. Egdell, and W. R. Flavell, Journal of Materials Chemistry **1**(4), 489 (1991).

[260] F. Parmigiani, Z. X. Shen, D. B. Mitzi, I. Lindau, W. E. Spicer, *et al.*, Physical Review B **43**(4), 3085 (1991).

[261] M. Taguchi, A. Chainani, K. Horiba, Y. Takata, M. Yabashi, *et al.*, Physical Review Letters **95**(17), 8 (2005).

[262] K. Maiti, J. Fink, S. de Jong, M. Gorgoi, C. Lin, *et al.*, Physical Review B **80**(16), 165132 (2009).

[263] F. Burgüzy, C. Politis, P. Lamparter, and S. Steeb, Zeitschrift für Naturforschung A **44a**, 780 (1989).

[264] M. H. Frommer, Superconductor Science and Technology **3**(11), 523 (1990).

[265] M. van Veenendaal, Physical Review B **74**(8), 085118 (2006).

[266] P. Steiner, S. Hüfner, V. Kinsinger, I. Sander, B. Siegwart, *et al.*, Surface and Interface Analysis **12**(5), 326 (1988).

[267] A. F. Carley, M. W. Roberts, J. S. Lees, and R. J. D. Tilley, J. Chem. Soc., Faraday Trans. **86**(18), 3129 (1990).

[268] T. Böske, K. Maiti, O. Knauff, K. Ruck, M. S. Golden, *et al.*, Physical Review B **57**(1), 138 (1998).

[269] C.-Q. Jin, S. Adachi, X.-J. Wu, H. Yamauchi, and S. Tanaka, Physica C: Superconductivity **223**(3-4), 238 (1994).

[270] G. Balestrino, S. Martellucci, P. Medaglia, A. Paoletti, and G. Petrocelli, Physica C: Superconductivity **302**(1), 78 (1998).

[271] Y. Krockenberger, A. Ikeda, K. Kumakura, and H. Yamamoto, Journal of Applied Physics **124**(7), 073905 (2018).

[272] H. Takagi, T. Ido, S. Ishibashi, M. Uota, S. Uchida, *et al.*, Physical Review B **40**(4), 2254 (1989).

[273] K.-i. Kubo and H. Yamauchi, Physical Review B **49**(2), 1289 (1994).

[274] K.-i. Kubo, M. Ichikawa, N. Sugii, K. Yamamoto, and H. Yamauchi, Physical Review B **49**(10), 6919 (1994).

[275] M. Karppinen and H. Yamauchi, Philosophical Magazine B **79**(2), 343 (1999).

[276] J. T. Herron and H. I. Schiff, The Journal of Chemical Physics **24**(6), 1266 (1956).

[277] D. Nečas and P. Klapetek, Central European Journal of Physics **10**, 181 (2012).

[278] L. J. van der Pauw, Philips Technical Review **20**, 220 (1958).

[279] L. J. van der Pauw, Philips Research Reports **13**, 1 (1958).

[280] K. Okada and A. Kotani, Physical Review B **52**(7), 4794 (1995).